ASRITE

Annual Symposium on Research and Industrial Training
of Department of Electronics

Proceedings of
13th Annual Symposium on Research and Industrial Training
of
Department of Electronics

11th September 2026

Department of Electronics
Faculty of Applied Sciences
Wayamba University of Sri Lanka
Kuliyapitiya,60200
Sri Lanka.

Proceedings of
13th Annual Symposium on Research and Industrial Training
of
Department of Electronics

11th September, 2026

ASRITE
Annual Symposium on Research and Industrial Training
of Department of Electronics

Department of Electronics
Faculty of Applied Sciences
Wayamba University of Sri Lanka
Kuliyapitiya, 60200
Sri Lanka

Editorial Board

Editor-in- chief
Snr. Prof. K. P. Vidanapathirana

Review Editor
Snr. Prof. (Mrs.) G.A.K.S. Perera

Board Members
Snr. Prof. K.P. Vidanapathirana
Snr. Prof. (Mrs.) G.A.K.S. Perera
Prof. L.D.R.D. Perera
Prof. (Mrs.) J.M.J.W. Jayasinghe
Prof. M.A.A. Karunarathna
Dr. Y.A.A. Kumarayapa
Dr. W.A.S. Wijesinghe
Eng. S.R.L. Gunawardhana
Mr. P.G.T.R. Payagala

Review Panel
Snr. Prof. K.P. Vidanapathirana
Snr. Prof. L.B.D.R.P. Wijesundara
Prof. (Mrs.) J.M.J.W. Jayasinghe
Prof. M.A.A. Karunarathna
Dr. W.A.S. Wijesinghe
Mr. P.G.T.R. Payagala

©Department of Electronics, Faculty of Applied Sciences,
Wayamba University of Sri Lanka, 2026

ISSN 2362 0560
Designing and Printing at the Department of Electronics,
Faculty of Applied Sciences, Wayamba University of Sri Lanka, Kuliyapitiya

Message from the Dean

It is with great pleasure and pride that I extend my warmest greetings to the Annual Symposium on Research and Industrial Training of the Department of Electronics 2026 (ASTITE), hosted by the Department of Electronics of the Faculty of Applied Sciences, Wayamba University of Sri Lanka. Since its inception in 2014, ASRITE has established itself as a premier platform for young researchers to showcase their creativity, innovations, and research findings and to receive wider attention from the scientific and industrial communities.

Research and innovation are the lifeblood of technological advancement and academic excellence. In this era of rapid technological development, the ability to think critically, challenge existing paradigms, and build practical solutions is more vital than ever. The Department of Electronics has consistently nurtured these qualities among its products. The diverse range of research areas covered in the symposium reflects the modern, forward-thinking nature of the presenters.

I strongly encourage all our young researchers to view today not just as the culmination of their projects, but as the true beginning of their journey as lifelong innovators and researchers. I believe that the year-long research experience provides a unique learning experience to bridge the gap between academic theory and real-world practice. Engaging in scientific inquiry helps develop the advanced problem-solving capabilities, resilience, and adaptability required to excel in a competitive global landscape. This strong foundation is instrumental in maintaining an exceptional employability rate and a commendable position in the top-tier organizations.

I would like to express my sincere appreciation to the academic staff of the Department of Electronics for their unyielding commitment, mentorship, and guidance in research. My gratitude also goes out to the industry experts whose collaboration ensures that our research remains relevant to contemporary industrial demands. Finally, I commend the Coordinator and the organizing committee of ASRITE 2026 for their dedication and hard work in making a stage for young researchers.

I congratulate the young researchers on your achievements and urge you to keep pushing the boundaries of technology to serve society. I wish ASRITE 2026 all the success.

Prof. MMDR Deegahawature
Dean, Faculty of Applied Sciences
Wayamba University of Sri Lanka

Foreword

It is with great pleasure and satisfaction that I write this foreword to the proceedings of the 13th Annual Symposium on Research and Industrial Training of the Department of Electronics (ASRITE 2026), Faculty of Applied Sciences, Wayamba University of Sri Lanka.

ASRITE provides a valuable platform for undergraduates of the Department of Electronics to present the findings of their final-year research. Through the research projects, students apply the knowledge and skills they have acquired in various fields of electronics, power and energy, and communication to develop innovative and practical solutions to real-world research problems. The symposium therefore provides an important opportunity for students to demonstrate their technical competencies, research capabilities, and creativity while gaining valuable experience in communicating their research findings.

The successful organization of this symposium is the result of the dedicated efforts and contributions of many individuals. I would like to express my sincere gratitude to Prof. E. M. P. Ekanayake, Vice Chancellor of Wayamba University of Sri Lanka, and Prof. M. M. D. R. Deegahawathura, Dean of the Faculty of Applied Sciences, for their guidance and continued support. I also extend my sincere appreciation to Prof. L. D. R. D. Perera, Coordinator of ASRITE 2026, and the organizing committee, comprising staff and students of the Department of Electronics, for their commitment and hard work in organizing this event. My special appreciation goes to all academic staff members of the Department for their dedicated supervision of the students' research projects throughout the year and for their valuable contribution to the rigorous double-blind review process. I also gratefully acknowledge Mr. Anuradha Udunuwara, Senior Engineer – Enterprise Business Solutions at Sri Lanka Telecom PLC and Tech Lead at Xyntac Singapore Pte. Ltd., for accepting our invitation to deliver the keynote address, and all the evaluators for their valuable service in evaluating the project demonstrations and presentations.

The symposium would not be possible without the research contributions of our students. I sincerely congratulate all the students for their commitment, perseverance, and enthusiasm throughout their research journey. I hope that participating in ASRITE 2026 has been a rewarding and enriching learning experience for them, providing valuable insights into the research process and professional communication.

Finally, I hope that ASRITE 2026 will inspire our graduates to pursue further research and innovation in diverse fields of Electronics and related disciplines, and encourage them to contribute meaningfully to technological advancement and the sustainable development of our country.

J.M. Jeevani W. Jayasinghe

Professor in Electrical and Electronic Engineering
Head/ Department of Electronics

CONTENTS

1	**EDGE-AI FRUIT-FLY DETECTION AND ADAPTIVE ULTRASONIC DETERRENCE SYSTEM FOR SMART AGRICULTURE** S.D.N. Fernando*, M.A.A. Karunarathna	1
2	**EXPANDABLE CELL POWER STORAGE SYSTEM INTEGRATED WITH A SMART BATTERY MANAGEMENT SYSTEM** Y.A. Rajapaksha*, G.A.K.S. Perera	9
3	**SMART MOTION-ACTIVATED CCTV ENHANCEMENT MODULE WITH BACKUP RECORDING** K.S.C. Fernando*, K.P. Vidanapathirana	15
4	**DESIGN OF A COMPACT HIGH-GAIN PRINTED ANTENNA FOR LONG RANGE (LoRa) COMMUNICATION** E.V.N. Thathsarani*, J.M.J.W. Jayasinghe	23
5	**LOW-COST FPGA-BASED REAL-TIME NEAR-FIELD ELECTROMAGNETIC NOISE SPECTRUM ANALYZER USING A SPARTAN-3E** P.M.I. Nimanthini*, W.A.S. Wijesinghe	31
6	**REAL-TIME BRAKE PAD OVERHEAT DETECTION AND WARNING SYSTEM FOR VEHICLES HAVING DISC BRAKES** H.C.F.Aththachchi*, K.P.Vidanapathirana	39
7	**DESIGN AND IMPLEMENTATION OF A SMART SHOP PROMOTION SYSTEM USING RADIO FREQUENCY IDENTIFICATION AND GEOFENCING TECHNOLOGY** A.A.B.C. Jayawardhana*, J.M.J.W. Jayasinghe, T.M. Premathilake	47
8.	**DEVELOPMENT OF A LOW-COST FABRIC DYE POWDER MIXING PROTOTYPE WITH GRAVIMETRIC DISPENSING AND COLOUR SENSING** H.P.D.P.C. Madhusanka*, P.G.T.R. Payagala	55
9	**DEVELOPMENT OF A MACHINE LEARNING-BASED NON-INVASIVE BLOOD GLUCOSE ESTIMATION SYSTEM** I. D. S. T. Madhushankha*, P. G. T. R. Payagala	63

10	**IOT-BASED REAL-TIME MONITORING AND ALERT SYSTEM FOR SAFETY IN MINING TUNNELS** S.S.P.P. De Silva*, S.R.L. Gunawardhana	71
11	**TRUE RANDOM NUMBER GENERATOR USING TRANSISTOR NOISE FOR SECURE OTP GENERATION** L.K. Abeyrathna*, W.A.S.Wijesinghe	79
12	**SMART ACADEMIC DOCUMENT SUBMISSION LOCKER USING IMAGE PROCESSING AND IOT** U.S. Weeragoda*, M.A.A. Karunarathna	87
13	**DESIGN AND IMPLEMENTATION OF A MULTI-SENSOR ALCOHOL VAPOUR DETECTION SYSTEM USING EMBEDDED MACHINE LEARNING** K.S.M.J. Fernando*, P.G.T.R. Payagala	95
14	**A LOW-COST IOT-BASED LANDSLIDE EARLY-WARNING PROTOTYPE USING HYDROLOGICAL AND INERTIAL DATA FUSION** K.K.N. Alwis*, W.A.S. Wijesinghe	103
15	**SOLAR-POWERED IOT SYSTEM FOR OUTDOOR AIR-QUALITY AND ENERGY MONITORING WITH AI-BASED PREDICTION AND AUTOMATIC LIGHTING** K.P.I. Ashani*, S.R.L. Gunawardhana	111
16	**DESIGN AND IMPLEMENTATION OF A MULTI-SPECTRUM LI-FI COMMUNICATION SYSTEM WITH ADAPTIVE TRANSMISSION** H.M.M.U. Menike*, S.R.L. Gunawardhana	119

Proc. Annual Symposium on Research & Industrial Training, 13 (2026) 1 - 8
Department of Electronics – Wayamba University of Sri Lanka

EDGE-AI FRUIT-FLY DETECTION AND ADAPTIVE ULTRASONIC DETERRENCE SYSTEM FOR SMART AGRICULTURE

S.D.N. Fernando*, M.A.A. Karunarathna

Department of Electronics, Wayamba University of Sri Lanka, Kuliyapitiya, Sri Lanka

**dhanushkafdo2001@gmail.com*

ABSTRACT

Insect pest infestation is a major cause of crop and post-harvest loss for smallholder farmers, who typically rely on broad-spectrum pesticide spraying that is costly, non-selective, and harmful to the environment and human health. This paper presents the design and progressive development of a low-cost, AI-based pest detection and protection system intended for smart agriculture applications. The system pairs a Raspberry Pi 3B+ running a real-time YOLO-based object detection model with an ESP32 microcontroller driving a bank of waterproof ultrasonic transducers, allowing the platform to automatically detect a target pest from a live camera feed and trigger a targeted ultrasonic deterrent signal rather than a chemical one. A DHT22 sensor logs local temperature and humidity, and a web-based dashboard provides real-time monitoring of the live camera feed, pest counts, actuation status, and environmental readings. Beyond simple detection-triggered activation, the system incorporates an adaptive search procedure that evaluates candidate ultrasonic frequencies and duty cycles over fixed observation windows, first sweeping a wide frequency range and then narrowing in on the most promising region, in order to identify the signal parameters most effective at deterring the detected pest. During this reporting period, the detection model was retrained on an expanded dataset of 2000 images (65%/15%/10% train/validation/test split) that included low-quality, blurred, and variable-lighting images, using data augmentation to improve robustness under realistic field conditions; the retrained model achieved a precision of approximately 97%, recall of approximately 97%, and a mean average precision (mAP@0.5) of approximately 99% on the validation set. The ultrasonic actuation hardware was also upgraded to a 5140 waterproof ultrasonic speaker unit for improved outdoor durability. In a preliminary open-field test with 15 repeated trials per candidate, a coarse frequency sweep identified a 35 kHz signal at 60% duty cycle as producing the largest and only statistically significant reduction in observed pest count among the thirteen candidates tested; this is an initial, controlled-test indication rather than confirmed field-level pest protection, and further trials are needed before practical efficacy can be established. Fruit flies were the primary target species, given their impact on fruit and vegetable crops in Sri Lanka. These preliminary results indicate that a low-cost edge-AI platform can feasibly combine real-time pest recognition with an adaptive, non-chemical deterrent response, offering smallholder farmers a potentially more targeted and sustainable alternative to routine pesticide application, pending further validation.

Keywords: Pest detection, **Y**OLO, **U**ltrasonic deterrent

1.0 INTRODUCTION

Insect pests are responsible for substantial pre- and post-harvest losses in tropical and subtropical agriculture, including in Sri Lanka, where smallholder farmers form the backbone of fruit and vegetable production [1]. The conventional response to such infestations is the routine application of broad-spectrum chemical pesticides. While effective in the short term, this approach is costly for smallholders, non-selective toward beneficial insects, and associated with long-term risks to soil health, water quality, and human health, as well as the gradual development of pesticide resistance in target pest populations.

Existing low-cost monitoring alternatives, such as sticky traps and pheromone traps, require frequent manual inspection and provide only a delayed, indirect estimate of pest activity rather

than an automated, real-time response [2]. Meanwhile, recent advances in low-power embedded hardware, such as the ESP32 microcontroller and single-board computers like the Raspberry Pi, together with lightweight on-device object detection models such as the YOLO family, have made it practical to run real-time computer vision directly at the point of deployment rather than depending on constant cloud connectivity [3]. Ultrasonic emissions have also been explored as a non-chemical means of disrupting insect behavior. Reported effective ranges for arthropod pests fall broadly within 20-65 kHz, offering a potential deterrent pathway that does not involve any chemical residue [4, 5].

Building on these developments, this project proposes an integrated, low-cost AI-based pest detection and protection system that continuously monitors a crop area using a camera and an on-device detection model, and automatically activates a targeted ultrasonic deterrent signal upon detecting a target pest, while also logging local environmental conditions and adaptively searching for the most effective deterrent frequency. Fruit flies were used as the target pest species for training and field validation in this study, given their significant economic impact on fruit and vegetable crops, although the underlying detection-and-deterrent framework is not inherently specific to a single species. This paper reports on the current stage of development of this system, focusing on the detection model refinement, the ultrasonic actuation hardware, the adaptive frequency optimization method, the monitoring dashboard, and the results of laboratory and field testing conducted during this reporting period.

The specific objectives are developing a real-time, on-device YOLO detection model for the target pest, implement a low-cost ESP32-driven ultrasonic actuation unit triggered on detection; implement an adaptive search identifying the frequency/duty-cycle combination with the greatest statistically supported pest-count reduction and provide real-time monitoring via a web dashboard.

2.0 EXPERIMENTAL

2.1 System overview and block diagram

The system has two units (Fig. 2.1). A Raspberry Pi 3B+ with a camera runs a YOLO detection model (TFLite) for on-device inference. An ESP32 drives ultrasonic transducers via TIP31C stages and reads a DHT22 sensor. The units communicate over Wi-Fi: on detecting a pest above threshold, the Pi triggers the ESP32 to emit an ultrasonic deterrent. A Wi-Fi dashboard shows the live feed, pest count, actuation status, and sensor readings.

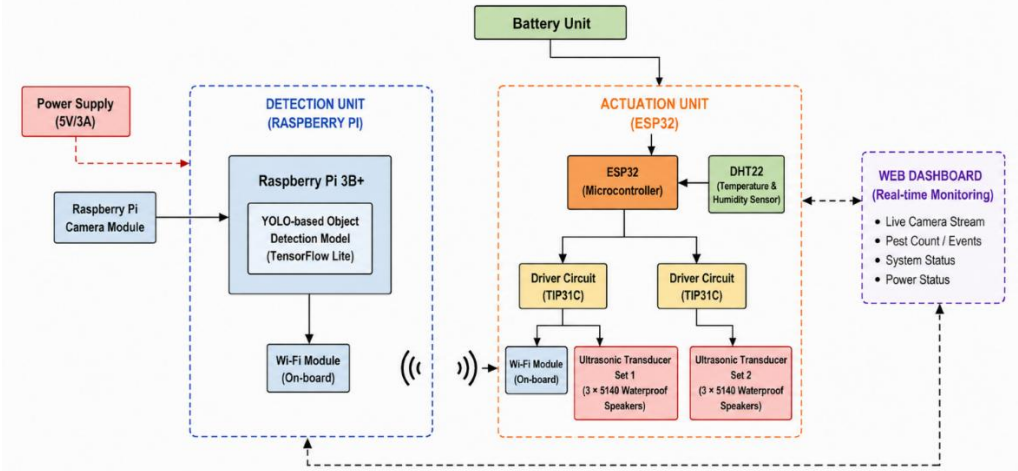


Figure 2.1: Block diagram of the AI-based pest detection and protection system, showing the Raspberry Pi detection unit, the ESP32 actuation unit with its ultrasonic transducer sets and DHT22 sensor, and the web-based monitoring dashboard.

2.2 Ultrasonic actuation circuit and hardware realization

The ultrasonic deterrent stage is built around the ESP32 microcontroller, which generates the drive signal on a general-purpose I/O pin configured as a PWM output. This output is connected through a 1 kΩ base resistor to the base of a TIP31C NPN power transistor, which is used as a low-side switch to drive the ultrasonic transducer load from a common 5 V supply rail. Three 5140 waterproof ultrasonic speakers are connected as one set on each switched output, and two such sets are implemented, giving a total of six ultrasonic transducers arranged as two independently switchable channels. The resulting hardware interconnections are shown in Figure 2.2. This arrangement was chosen to provide wider acoustic coverage of the monitored area while keeping the driver circuit simple and inexpensive to reproduce. The 5140 waterproof speaker was selected to replace an earlier, non-waterproof speaker used in an initial prototype, improving the durability and reliability of the deterrent unit for continuous outdoor deployment.

Environmental sensing is provided by a DHT22 digital temperature and humidity sensor, interfaced to a dedicated GPIO pin on the ESP32. A 10 kΩ resistor is connected in parallel between the sensor's supply and data lines, acting as a pull-up resistor, as required for reliable single-wire communication with the sensor [6].

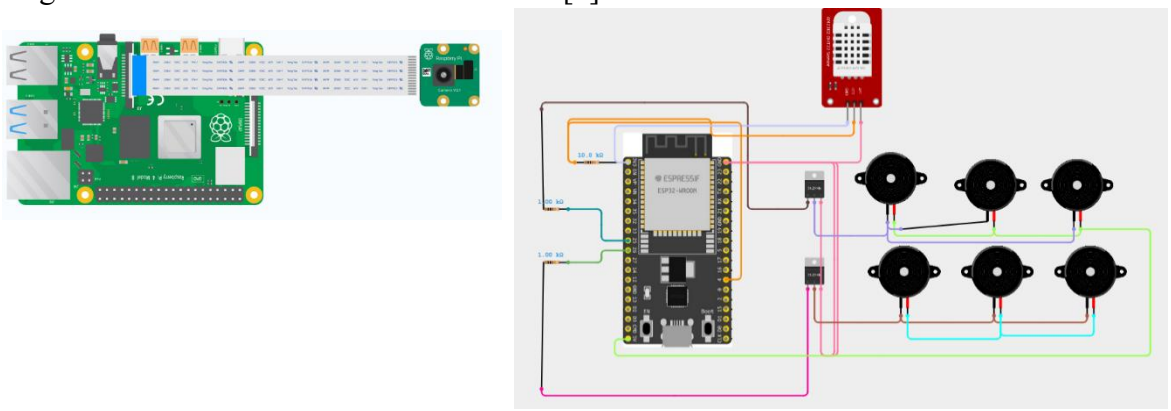


Figure 2.2: Hardware interconnections of the actuation and detection units the ESP32 GPIO output, 1 kΩ base resistor, TIP31C transistor, ultrasonic speaker sets, and DHT22 sensor with its 10 kΩ pull-up resistor, together with the Raspberry Pi 3B+ connected to the Raspberry Pi Camera Module V2 via the CSI ribbon cable for the detection unit.

2.3 Dataset and model training

The detection model was a YOLOv8 model [7] trained at an input resolution of 320x320 pixels, on a 2000-image dataset of fruit flies (single detection class), manually annotated using Roboflow's tool and hosted on Roboflow, with a 65%/15%/10% train/validation/test split. During this reporting period, the dataset was expanded with additional images deliberately chosen to represent challenging field conditions, including low-quality, blurred, and variable-lighting images, to better reflect real outdoor deployment conditions rather than only clean laboratory captures. Data augmentation (brightness, contrast, blur, rotation, noise) was applied to improve robustness [3, 8]. The model was retrained on this expanded, augmented dataset and exported to TensorFlow Lite (845 kB) for deployment on the Raspberry Pi 3B+.

2.4 Detection-triggered deterrent logic

During operation, the perception unit continuously captures frames from the camera and runs the detection model on each frame. When a target pest is detected with a confidence above the configured threshold, the perception unit sends a signal over Wi-Fi to the ESP32 actuation unit, which activates the ultrasonic output before returning to an idle state. This event-driven

approach ensures that the ultrasonic deterrent is applied specifically when a pest is present, rather than continuously, reducing unnecessary acoustic emission and power consumption.

2.5 Testing methodology

The retrained detection model was evaluated against the previous model version using real-time camera testing under different lighting conditions, to assess whether the dataset expansion and augmentation improved detection reliability under realistic field variation. The complete system, comprising the camera and detection unit, the ESP32 actuation unit with the upgraded 5140 waterproof speakers, and the DHT22 sensor, was tested under both controlled laboratory conditions and open-field outdoor conditions to confirm correct end-to-end operation, including successful ultrasonic activation immediately following a positive detection event. The 5140 transducers are rated for 40 kHz ± 1.5 kHz. Drive frequency and acoustic output were verified with an ESP32 sampling a matched 40 kHz ± 1.5 kHz waterproof ultrasonic receiver at fixed distances/angles, giving an effective coverage area of approximately 22.6 m^2 (5.36 m diameter, 30° beam angle) over a tested range of up to 10 m. Frequency-sweep trials ran under open-field conditions, each candidate repeated over 15 trials. Inference settings on the Raspberry Pi 3B+ were also tuned during this process to sustain real-time operation on this resource-constrained edge device.

2.6 Adaptive ultrasonic frequency optimization

Rather than emitting a single, fixed ultrasonic frequency, the actuation logic incorporates an adaptive search procedure that evaluates a set of candidate frequencies and duty cycles to identify the combination most effective at reducing the observed pest count. Each candidate signal is applied for a fixed observation window, chosen to be long enough to allow any change in pest presence to be observed, and the pest count recorded by the detection unit immediately before and after the signal is applied is compared to estimate the effectiveness of that candidate. For a candidate signal producing a baseline pest count C_{base} and a post-actuation count C_{after} over matched observation windows, the deterrent effect is computed using following equation 01.

$$\text{Effect (\%)} = [(C_{base} - C_{after}) / C_{base}] \times 100 \quad [1]$$

Here, Effect (%) denotes the percentage reduction in pest count attributed to the candidate signal, C_{base} is the pest count recorded during the baseline observation window, and C_{after} is the pest count recorded during the matched post-actuation observation window.

A candidate is only accepted as a genuine deterrent, rather than incidental variation in fly activity, if a two-sample statistical significance test comparing the before- and after-actuation counts across repeated trials returns [9].

$$t = (\bar{x}_{base} - \bar{x}_{after}) / \sqrt{(s^2_{base}/n_{base} + s^2_{after}/n_{after})} \quad [2]$$

Here, t is the calculated t-statistic used to test the significance of the change in pest count; $\bar{x}_{base}$ and $\bar{x}_{after}$ are the mean pest counts observed across repeated baseline and post-actuation trials, respectively; s^2_{base} and s^2_{after} are the corresponding sample variances; and n_{base} and n_{after} are the number of baseline and post-actuation trials conducted for that candidate.

The search proceeds in two stages. a coarse sweep first evaluates a small number of widely spaced candidate frequencies across the ultrasonic range, and once each candidate has been evaluated a sufficient number of times, a finer sweep narrows in on the region around the best-performing coarse candidate, testing more closely spaced frequencies within that window to more precisely locate the most effective signal. Candidate selection at each stage is guided by

an upper-confidence-bound (UCB1) strategy [10] that balances exploring candidates with limited prior data against re-testing candidates that have performed well so far. At trial n, the candidate i with the highest score is selected next.

$$UCB_i\,(n) = \bar{x}_i + c \times \sqrt{(2 \ln n / n_i)} \qquad [3]$$

Here, $UCB_i\,(n)$ denotes the upper-confidence-bound score assigned to candidate i at trial n, used to rank candidates for selection, where and $\bar{x}_i$ is the mean observed effect of candidate i, n_i is the number of times candidate i has been tested, n is the total number of trials completed so far, and c is an exploration constant that controls how strongly under-tested candidates are favored. Only measurements that pass the significance check in Equation (2) are used to update the ranking used in Equation (3), so that the candidate identified as most effective reflects a genuine and repeatable reduction in pest presence rather than incidental variation in pest activity.

2.7 Web-based monitoring dashboard

A browser-based dashboard, served locally over Wi-Fi by the perception unit, provides real-time visibility into system operation without requiring direct access to either the Raspberry Pi or the ESP32. The dashboard displays the live annotated camera feed with detected pests highlighted, the current pest count and its recent trend, the actuation status and currently selected ultrasonic frequency and duty cycle, the stage of the frequency optimization search, and the DHT22 temperature and humidity readings. For deployments with multiple actuation units, the dashboard also displays the physical location of each unit on a map, allowing a user to monitor coverage across a wider growing area from a single interface and the result data sent to the user as sms. The dashboard layout is shown in Figure 2.3.

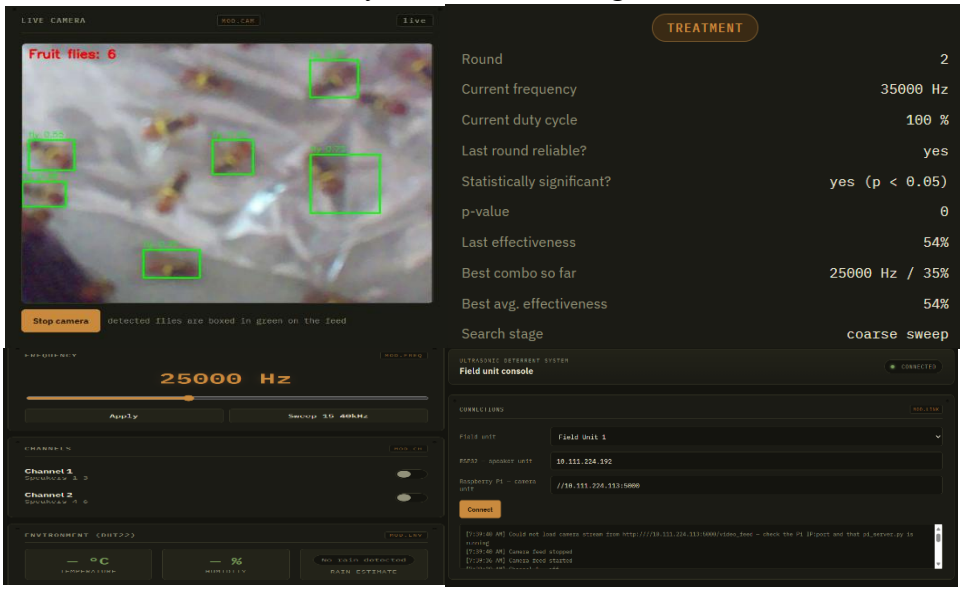


Figure 2.3: Web-based monitoring dashboard showing the live camera feed, pest count, actuation status, and environmental sensor readings.

3.0 RESULTS AND DISCUSSION

3.1 Detection model training performance

The retrained model trained for approximately 120 epochs; loss curves in Figure 3.1 decreased steadily and converged without divergence, which is consistent with, though not sufficient on its own to establish, the absence of overfitting. On the validation set, the model reached a

precision of approximately 97%, recall of approximately 97%, mAP@0.5 of approximately 99%, and mAP@0.5:0.95 of approximately 90%, consistent with levels reported for other YOLO-based fruit-fly detectors [3, 11] and with fewer false detections versus the previous model under varied lighting.

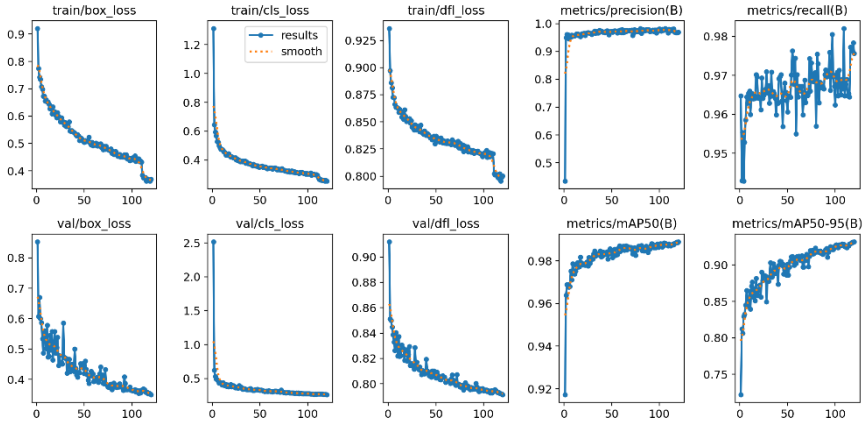
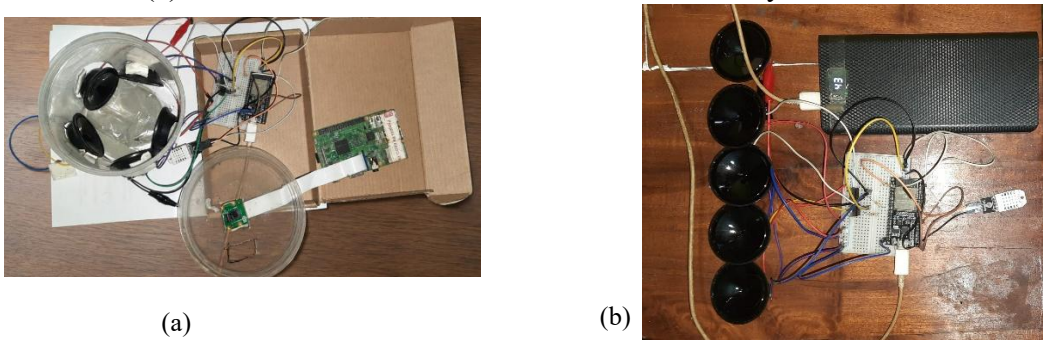


Figure 3.1: Training and validation loss curves and detection performance metrics (precision, recall, mAP@0.5, and mAP@0.5:0.95) for the retrained YOLO detection model.

3.2 Hardware integration and deterrent activation

Integration of the 5140 waterproof ultrasonic speaker with the Raspberry Pi and ESP32 actuation unit was verified, with the output activating successfully after each detection. The 5140 unit, replacing a non-waterproof speaker in the initial prototype, is expected to offer improved outdoor durability. Figure 3.2 shows the assembled prototype: Raspberry Pi with camera module (a) and ESP32 driver circuit with transducer array and DHT22 sensor (b).



(a) (b)

Figure 3.2: Assembled prototype hardware. (a) Raspberry Pi 3B+ with camera module used as the detection unit; (b) ESP32 driver circuit with ultrasonic transducer array, DHT22 sensor, and portable power supply used as the actuation unit.

3.3 Real-time performance on edge hardware

Inference settings were optimized to maintain real-time detection on the Raspberry Pi 3B+, a resource-constrained single-board computer, without offloading computation to an external server or cloud [12], confirming the feasibility of running the full detection-to-actuation pipeline on low-cost, locally available edge hardware important for a system intended to be affordable and deployable without reliable internet.

3.4 Adaptive frequency optimization and dashboard status

The adaptive frequency optimization procedure and web-based dashboard described in Sections 2.6 and 2.7 have been implemented and verified, with the actuation unit correctly cycling through candidate frequencies and duty cycles and the dashboard correctly reflecting live camera feed, pest counts, and actuation status.

During this reporting period, a coarse sweep of thirteen candidate frequency and duty-cycle combinations spanning 20-40 kHz was completed; results are summarized in Table 3.2. Baseline and after-actuation pest counts gave the percentage effect via Equation (1), with the significance check of Equation (2) determining whether the change reflected a genuine deterrent response.

Table 3.2 Coarse-sweep candidate results for the adaptive ultrasonic frequency search

Time	Freq (Hz)	Duty (%)	Baseline	After	Effect	p-value (sig.)	Reliable
11:26:28 AM	20000	60	0.7	0.2	–	–	no
11:05:24 AM	40000	100	0.6	0.1	–	–	no
11:00:45 AM	25000	15	0.4	0.8	–	–	no
10:56:06 AM	20000	15	0.1	0.4	–	–	no
10:51:27 AM	35000	60	2.9	0.4	84%	0 (yes)	yes
10:46:52 AM	40000	15	0.6	0.0	–	–	no
10:42:10 AM	30000	60	1.8	0.2	–	–	no
10:37:31 AM	30000	100	0.0	2.0	–	–	no
6:17:02 PM	30000	15	0.7	0.6	–	–	no
6:12:31 PM	40000	35	0.0	0.1	–	–	no

Of the thirteen coarse candidates tested, twelve showed no significant change and were not retained as reliable. One yielded a computable, statistically significant result: a 35 kHz signal at 60% duty cycle reduced the pest count from a baseline of 2.9 to 0.4, an effect of approximately 84%, with $p \approx 0$, well below $\alpha = 0.05$, indicating a statistically significant, repeatable reduction in observed pest count in these open-field trials. This is a preliminary, controlled-test indication rather than confirmed field-level protection: no direct evidence yet establishes ultrasound as an effective fruit-fly control strategy [5], and sustained reductions in infestation or crop damage would need further field trials to confirm. Applying the UCB1 rule of Equation (3), this candidate carries by far the highest mean effect among candidates with a confirmed significant response and receives top priority for the fine sweep, expected to narrow in on the 35 kHz region at moderate-to-high duty cycles, consistent with reported effective ranges of 25-45 kHz for ultrasonic arthropod deterrence [4, 5]. Fine-sweep and field-validation results will follow in a future update.

4.0 CONCLUSION

This study developed and evaluated a low-cost, AI-based pest detection and deterrence platform for smart agriculture, combining a Raspberry Pi-based detection unit, an ESP32-

driven ultrasonic actuation unit, DHT22 environmental sensing, an adaptive frequency optimization procedure, and a web-based dashboard. The detection model was retrained on an expanded, augmented dataset, achieving approximately 97% precision, 97% recall, and mAP@0.5 of approximately 99%, with fewer false detections under challenging conditions; the actuation hardware was upgraded to a waterproof speaker unit for outdoor durability. A coarse frequency sweep identified 35 kHz at 60% duty cycle as the only statistically significant reduction in pest count in these preliminary open-field trials, prioritized via the UCB1 rule for the subsequent fine sweep. Laboratory and field testing confirmed reliable real-time detection and correct end-to-end operation, demonstrating technical feasibility as a preliminary, non-chemical alternative to routine pesticide spraying. Future work includes the fine frequency sweep, multi-season field trials, durability/power evaluation, and quantifying actual reductions in pest population and crop damage. Overall, these preliminary results support the technical feasibility of low-cost edge-AI platforms as a potentially more targeted, sustainable approach to pest management, pending further field confirmation.

ACKNOWLEDGEMENTS

The author expresses sincere gratitude to the academic and technical staff of the Department of Electronics, Faculty of Applied Sciences, Wayamba University of Sri Lanka, for their invaluable support throughout this project.

REFERENCES

1. Mutamiswa, R., Nyamukondiwa, C., Chikowore, G., Chidawanyika, F., Overview of Oriental Fruit Fly, Bactrocera dorsalis (Hendel) (Diptera: Tephritidae) in Africa: From Invasion, Bio-Ecology to Sustainable Management, *Crop Protection*, 141, (2021), art. 105492.
2. Dias, N.P., Zotti, M.J., Montoya, P., Carvalho, I.R., Nava, D.E., Fruit Fly Management Research: A Systematic Review of Monitoring and Control Tactics in the World, *Crop Protection*, 112, (2018), 187-200.
3. Mamdouh, N., Khattab, A.K.F., YOLO-Based Deep Learning Framework for Olive Fruit Fly Detection and Counting, *IEEE Access*, 9, (2021), 84252-84262.
4. Panthawong, A., Doggett, S.L., Chareonviriyaphap, T., The Efficacy of Ultrasonic Pest Repellent Devices against the Australian Paralysis Tick, Ixodes holocyclus (Acari: Ixodidae), *Insects*, 12(5), (2021), 400.
5. Aflitto, N., DeGomez, T., Sonic Pest Repellents, *University of Arizona Cooperative Extension*, Bulletin AZ1639, (2015).
6. Sutono, S., Mohamed, Y.H., IoT-Based Smart Agriculture System Using ESP32, DHT22, and Soil Moisture Sensors with Relay Control for Water-Scarce Environments, *Proc. Int. Conf. Informatics, Engineering, Science & Technology (INCITEST)*, 1, (2025), 1-8.
7. Ultralytics, YOLOv8, *Ultralytics Docs*. [Online]. Available: https://docs.ultralytics.com/models/yolov8/ (Accessed: 21 July 2026).
8. Pang, H., Zhang, Y., Cai, W., Li, B., Song, R., A Real-Time Object Detection Model for Orchard Pests Based on Improved YOLOv4 Algorithm, *Scientific Reports*, 12, (2022), art. 13418.
9. Montgomery, D.C., *Design and Analysis of Experiments*, 9th Ed., Hoboken, NJ, USA, John Wiley & Sons, 2017.
10. Auer, P., Cesa-Bianchi, N., Fischer, P., Finite-Time Analysis of the Multiarmed Bandit Problem, *Machine Learning*, 47(2-3), (2002), 235-256.
11. Hakim, A., Srivastava, A.K., Hamza, A., Owais, M., Habib-ur-Rahman, M., Qadri, S., Qayyum, M.A., Khan, F.Z.A., Mahmood, M.T., Gaiser, T., Yolo-pest: An Optimized YoloV8x for Detection of Small Insect Pests Using Smart Traps, *Scientific Reports*, 15, (2025), art. 14029.
12. Boddu, S., Mukherjee, A., Efficient Edge Deployment of Quantized YOLOv4-Tiny for Aerial Emergency Object Detection on Raspberry Pi 5, *arXiv:2506.09300*, (2025).

Proc. Annual Symposium on Research & Industrial Training, 13 (2026) 9 -14
Department of Electronics – Wayamba University of Sri Lanka

EXPANDABLE CELL POWER STORAGE SYSTEM INTEGRATED WITH A SMART BATTERY MANAGEMENT SYSTEM

Y.A. Rajapaksha*, G.A.K.S. Perera

Department of Electronics, Wayamba University of Sri Lanka, Kuliyapitiya, Sri Lanka

**yasasrajapaksha21@gmail.com*

ABSTRACT

The increasing demand for scalable and intelligent battery energy storage systems has highlighted the limitations of conventional lithium-ion battery packs with fixed cell configurations. These systems are difficult to expand, require replacement of the entire battery pack when individual cells fail, and often lack individual cell monitoring capabilities. This research presents the design and implementation of an expandable cell power storage system integrated with a smart battery management system that enables modular battery expansion, individual cell monitoring, and remote system supervision. The proposed prototype consists of three battery modules, each containing two series-connected lithium-ion cells, together with passive cell balancing, voltage and temperature monitoring, state-of-charge estimation, a microcontroller-based control unit, and a metal oxide semiconductor field effect transistor switching circuit for connecting and disconnecting battery modules. Battery parameters are displayed locally using a thin-film transistor liquid crystal display and transmitted through wireless communication to a web-based monitoring dashboard for real-time remote observation. Experimental evaluations under different load conditions confirmed the successful operations of the monitoring system, passive balancing circuit, and module switching mechanism. The developed system demonstrated reliable battery operation while allowing individual modules to be isolated or reconnected without interrupting the remaining battery pack. The proposed architecture provides an effective solution for improving the scalability, maintainability, and operational flexibility of lithium-ion battery energy storage systems.

Keywords: Battery management system, **L**ithium-ion battery, **S**tate of charge

1.0 INTRODUCTION

The increasing demand for renewable energy systems for different applications including electric vehicles, portable electronic devices, and backup power solutions has led to the widespread adoption of lithium-ion (Li-ion) battery technology due to its high energy density, long cycle life, and low self-discharge rate. As battery-powered applications continue to expand, the need for battery systems that are scalable, reliable, and easy to maintain has become increasingly important. Battery Management Systems (BMSs) play a vital role in ensuring the safe and efficient operation of Li-ion battery packs by monitoring battery parameters, protecting cells from abnormal operating conditions, and improving battery lifespan [1-3].

Conventional Li-ion battery packs are typically designed with a fixed cell configuration, making it difficult to increase or decrease the energy storage capacity according to varying application requirements. In addition, when a single cell becomes defective, replacing that individual cell is often impractical, leading to increased maintenance costs and unnecessary battery waste. Furthermore, many existing battery management systems primarily monitor the overall battery pack rather than individual cell performance, limiting the ability to detect cell imbalance, degradation, or faults at an early stage [1- 4]. Recent studies on expandable battery energy storage systems have demonstrated the potential of modular battery architectures to improve system scalability, simplify maintenance, and enhance overall reliability [2,4].

Similarly, the integration of Internet of Things (IoT) technologies into battery management systems has enabled real-time remote monitoring of battery parameters such as cell voltage, temperature, and state of charge (SOC), allowing users to access battery information through web-based applications and improving predictive maintenance capabilities [3].

Although modular battery architectures and IoT-based monitoring techniques have been investigated separately, there remains a need for an integrated solution that combines expandable battery storage with intelligent battery management. Such a system should allow battery capacity to be easily expanded according to user requirements, enable defective cells to be replaced without replacing the entire battery pack, continuously monitor the condition of individual cells, and provide remote access to battery information while maintaining historical data logs for analysis [3,4].

Therefore, this research investigates the design and implementation of an expandable cell power storage system integrated with a smart BMS that provides flexible battery capacity expansion, individual cell replacement capability, real-time individual cell monitoring, remote web-based monitoring, and automatic battery data logging to improve the scalability, maintainability, and operational efficiency of Li-ion battery energy storage systems.

2.0 EXPERIMENTAL

2.1 Block diagram of the system

The proposed battery management circuit mainly consists of a battery module with multiple cells, battery balancing circuit, cell monitoring circuit, ESP32 microcontroller unit (MCU), cell disconnecting and connecting circuit, output controller and display to monitor the system as shown in Figure 2.1.

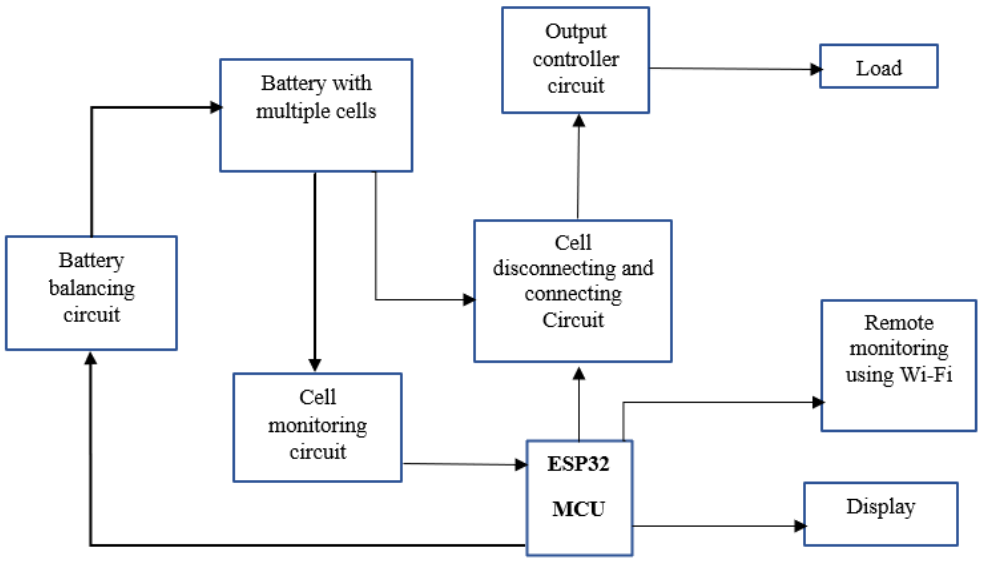


Figure 2.1: Block diagram of the BMS system

The experimental battery pack is consisting of 3 battery modules each containing series connected two 3.7 V lithium-ion cells. Hence, each module outputs near 7.4 V of voltage. The battery balancing circuit is balancing each cell in the system using passive cell balancing

method. The monitoring circuit monitors the voltage, temperature and SOC of each cell. The cell disconnecting and connecting circuit (Figure 2.2) uses IRFZ44N MOSFET transistors to connect and disconnect cells from the battery pack according to the microcontroller signals if need. The output controller circuit controls the output voltage of the battery pack. The parameters of each cells are displayed using the OLED display and the system can monitor in remotely using Wi-Fi communication through a web dashboard.

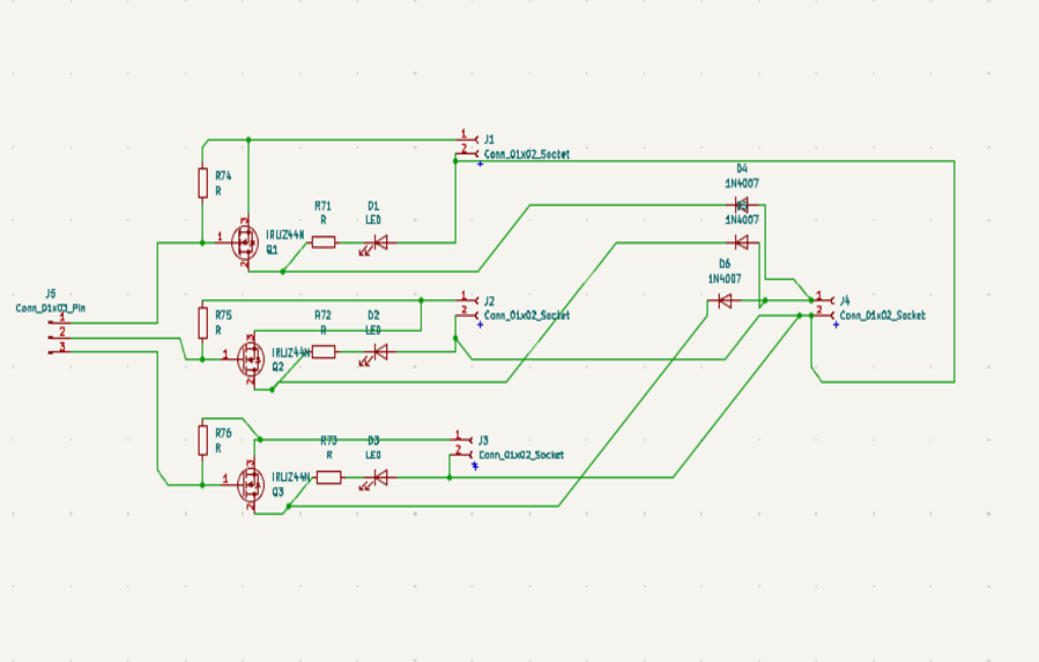


Figure 2.2: Circuit diagram of the cell connecting and disconnecting circuit

When microcontroller inputs a high voltage of 3.3 V, the corresponding cell is connected to the load and when microcontroller inputs 0 V to the MOSFET, the corresponding cell is disconnected from the load.

Hardware implementation of the system is shown in Figure 2.3.

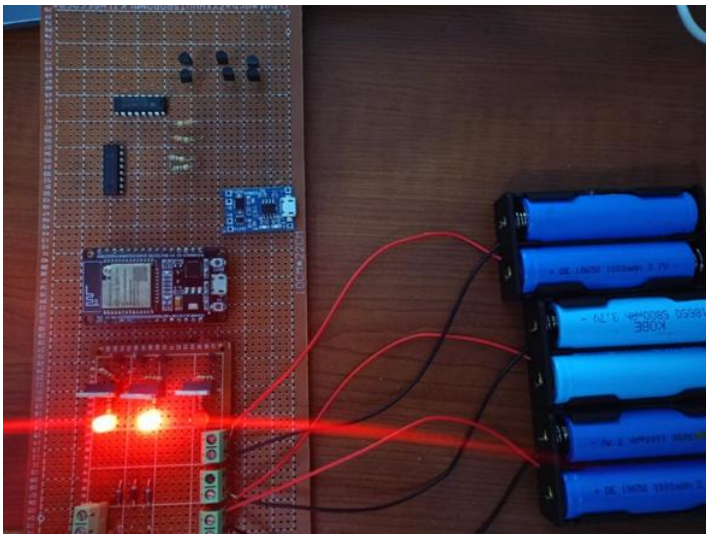


Figure 2.3: Hardware implementation of the system

The system was tested with different loads by connecting them to the output of the battery system and test the output voltage was tested by disconnecting cell modules from the system. Voltage, temperature and SOC values were monitored using display and the web dashboard.

3.0 RESULTS AND DISCUSSION

The cell connecting and disconnecting mechanism functioned correctly according to the control signals generated by the ESP32. The MOSFET based switching circuit enabled individual battery modules to be isolated or reconnected without interrupting the operation of the remaining battery pack.

This functionality demonstrated the modular nature of the proposed battery system, allowing faulty modules to be disconnected or additional modules to be integrated with minimal system interruption. The electronic switching method also provided faster operation and greater reliability than conventional mechanical switching methods [3].

The individual cell monitoring circuit successfully measured and displayed the voltage, temperature, and estimated SOC of each battery cell as shown in Figure 3.1.

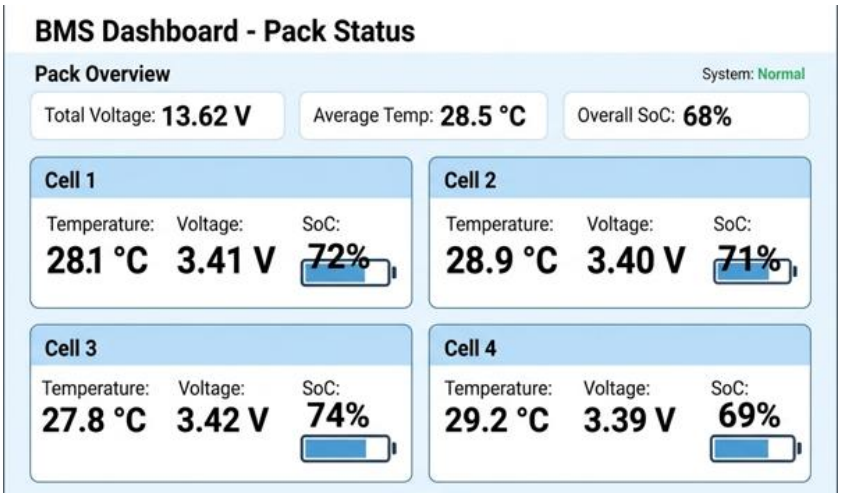


Figure 3.1: Battery status shown on the web dashboard

The measured values were updated continuously on the OLED display and transmitted to the web dashboard through the ESP32's Wi-Fi interface. The remote monitoring feature enabled users to observe battery conditions in real time without requiring direct access to the battery pack, improving system usability and maintenance [5,6].

4.0 CONCLUSION

The proposed expandable cell power storage system successfully demonstrated the feasibility of integrating modular battery reconfiguration with a smart BMS. The experimental results support the main objective of the study by showing that battery modules can be independently connected or disconnected while maintaining the operation of the remaining system which provides greater flexibility for capacity expansion and maintenance. In addition, individual cell voltage, temperature, and SOC information could be monitored locally and remotely through the ESP32 based web dashboard, supporting improved battery supervision and maintenance.

These findings are consistent with previous studies that have identified reconfigurable battery architectures and IoT based monitoring as effective approaches for improving battery-system scalability and monitoring capabilities. Although the prototype was successfully demonstrated under experimental load conditions, further research is required to evaluate long-term reliability, higher-power operation, larger battery configurations, switching durability, and more accurate SOC estimation. Overall, this study demonstrates that combining expandable battery modules with intelligent monitoring provides a practical foundation for developing more scalable, maintainable, and flexible Li-ion energy storage systems.

ACKNOWLEDGEMENTS

The authors would like to express their appreciation to the Department of Electronics, Faculty of Applied Sciences, Wayamba University of Sri Lanka, Kuliyapitiya, Sri Lanka.

REFERENCES

1. Farakhor, A., Wu, D., Wang, Y. and Fang, H., *IEEE Transactions on Transportation Electrification,* 2023, 9/2, 2878-2890. https://doi.org/10.1109/TTE.2022.3223993 (Accessed 2026-08-01).
2.Samaddar, N., Kumar, S. and Jayapragash, R., *Journal of Physics*, 2020, 1716/1, 012005. https://doi.org/10.1088/1742-6596/1716/1/012005 (Accessed 2026-08-01).
3. Karthikeyen, S., Kousi Priya, C., Varshini, M., Swathi, P. and Sudharsan, S., *Journal of Electronics and Informatics,* 2024, 6/2, 117-130. https://doi.org/10.36548/jei.2024.2.004 (Accessed 2026-08- 02).
4.Balasingam, B., Ahmed, M. and Pattipati, K., *Energies*, 2020, 13/11, 2825. https://www.mdpi.com/1996-1073/13/11/2825 (Accessed 2026-08-03).
5. Xiong, R., Li, L. and Tian, J., *Journal of Power Sources*, 2018, 405, 18-30. https://doi.org/10.1016/j.jpowsour.2018.10.019 (Accessed 2026-08-14).
6. Ng, K. S., Moo, C. S., Chen, Y. P. and Hsieh, Y. C., *Applied Energy*, 2009, 86/9, 1506-1511. https://doi.org/10.1016/j.apenergy.2008.11.021 (Accessed 2026-08-4).

Proc. Annual Symposium on Research & Industrial Training, 13 (2026) 15 - 22
Department of Electronics – Wayamba University of Sri Lanka

SMART MOTION-ACTIVATED CCTV ENHANCEMENT MODULE WITH BACKUP RECORDING

K.S.C. Fernando*, K.P. Vidanapathirana

Department of Electronics, Wayamba University of Sri Lanka, Kuliyapitiya, Sri Lanka

**fernandoshirantha06@gmail.com*

ABSTRACT

Closed-Circuit Television (CCTV) systems are widely used for security monitoring; however, conventional systems often operate continuously during periods without detected activity. This research presents the design and development of a smart CCTV enhancement system based on an STM32F103C8T6 microcontroller for motion-based CCTV power management. The proposed system integrates an RCWL-0513 microwave motion sensor with a MOSFET-based switching circuit to automatically activate a 12 V CCTV camera when motion is detected and deactivate it after approximately 30 s without further motion. A mini FPV DVR with MicroSD storage is incorporated to record and store CCTV video during activated surveillance periods, while LED and buzzer indicators provide visual and audio alerts. The hardware consists of a 12 V power input, LM2596 12 V-to-5 V buck converter, AMS1117-3.3 regulator, STM32F103C8T6 minimum system, ST-LINK interface, motion-sensing circuit, and CCTV switching and alert circuits. The schematic and PCB were developed using KiCad, while the protective enclosure was designed using SolidWorks. Experimental results demonstrated a motion detection range of approximately 5–6 m, a detection rate of approximately 90%, an average CCTV activation response of approximately 0.19 s, and an average deactivation time of approximately 30.3 s. The LED and buzzer operated successfully during motion detection, while the mini FPV DVR successfully recorded and stored CCTV video on a MicroSD card. The developed system demonstrates the feasibility of integrating microwave motion detection, automatic CCTV power control, local alerts, and event-based video recording into a compact CCTV enhancement module.

Keywords: STM32F103C8T6, **S**mart CCTV, **M**otion Detection

1.0 INTRODUCTION

Security and surveillance systems are widely used in residential, commercial, industrial, and public environments. Conventional Closed-Circuit Television (CCTV) systems generally operate continuously to provide uninterrupted monitoring, which can result in unnecessary camera operation during periods without detected activity. This creates a need for intelligent control methods that can manage CCTV operation according to actual surveillance requirements [1].

Recent developments in embedded systems and microcontroller technology enable CCTV systems to be controlled automatically using real-time motion information. This research presents the development of a smart CCTV enhancement module based on an STM32F103C8T6 microcontroller, RCWL-0513 microwave motion sensor, and MOSFET-based power switching circuit. The system incorporates LED and buzzer indicators for local alerts and a mini FPV DVR with MicroSD storage for local video recording. The electronic circuit was designed using KiCad, while the protective enclosure was developed using SolidWorks [1].

The developed prototype was experimentally evaluated for motion detection, CCTV activation and deactivation, alert operation, and local video recording. The experimental results demonstrated an approximately 5-6 m motion detection range, 90% detection rate, 0.19 s average CCTV activation response, and 30.3 s average deactivation time. The mini FPV DVR also successfully recorded and stored CCTV video on a MicroSD card. These results demonstrate the feasibility of integrating motion detection, automatic CCTV power control, local alerts, and event-based video recording into a compact CCTV enhancement system [2].

2.0 EXPERIMENTAL

2.1 Methodology and system architecture

The proposed smart CCTV security system consists of several integrated hardware and software modules designed to achieve automatic surveillance control based on human motion detection. The overall system architecture consists of a power management unit, STM32F103C8T6 microcontroller-based control unit, RCWL-0513 motion detection module, CCTV power switching circuit, user alert system, and mechanical enclosure. The complete system architecture is illustrated in Figure 2.1[2].

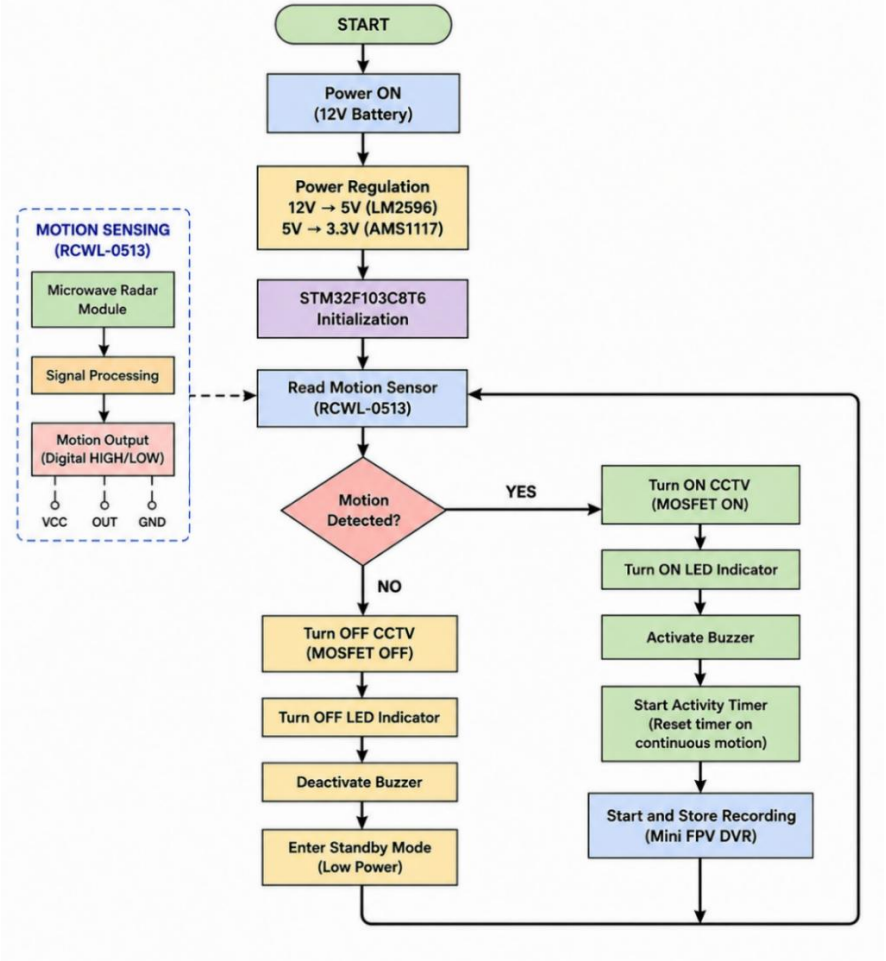


Figure 2.1: Block diagram of the proposed STM32-based smart CCTV security system. The system integrates a 12V power source, voltage regulation stage, STM32 controller, motion detection sensor, alert modules, and automatic CCTV power control unit.

The system receives power from a 12V DC battery source, which acts as the primary energy supply for the complete surveillance system. Since the individual components require different

operating voltages, a power conversion stage is implemented. The LM2596 buck converter is used to reduce the input voltage from 12V to 5V, while an AMS1117-3.3 voltage regulator provides a stable 3.3V supply for the STM32F103C8T6 microcontroller. The regulated power system ensures reliable operation of the controller, sensors, and external modules [3].

The STM32F103C8T6 functions as the main processing unit of the proposed system. It receives the digital output signal generated by the RCWL-0513 microwave motion sensor and determines the required control actions. When movement is detected, the microcontroller activates the CCTV power switching circuit and generates alert signals through the LED indicator and buzzer system. The overall control logic is designed to reduce unnecessary CCTV operation by activating the camera only when human activity is detected [4].

The CCTV camera power management system is implemented using an IRFZ44N MOSFET-based electronic switching circuit. The MOSFET operates as a low-side power switch controlled by the STM32 through a BC547 transistor driver stage. This arrangement provides reliable switching of the 12V CCTV supply while reducing the limitations associated with mechanical relays, such as slower switching response and reduced operating lifetime [5].

2.2 Hardware realization

The prototype implementation was developed by integrating the electronic circuits, embedded controller, and mechanical enclosure into a single compact security system. The complete hardware realization is shown in Figure 2.2 [3].

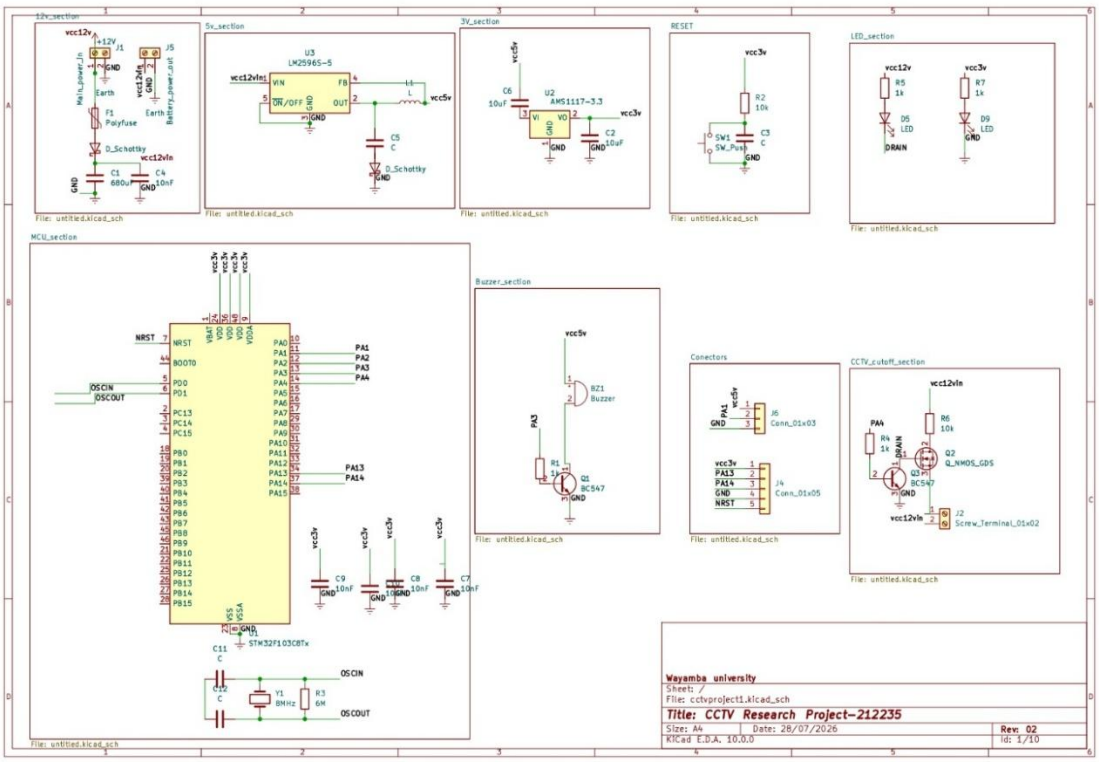


Figure 2.2: Complete hardware architecture of the proposed smart CCTV controller consisting of STM32F103C8T6, RCWL-0513 motion sensor, power regulation circuits, MOSFET switching stage, and alert modules.

The STM32F103C8T6 minimum system circuit was developed with all essential components required for stable microcontroller operation. The circuit includes an external 8MHz crystal oscillator connected to the OSC_IN and OSC_OUT pins, decoupling capacitors for power stability, a reset circuit using the NRST pin, BOOT0 configuration for normal operation, and an SWD programming interface for firmware development and debugging using the ST-LINK V2 programmer [6].

The motion detection subsystem is implemented using the RCWL-0513 microwave radar sensor. The sensor was selected because of its ability to detect human movement using microwave technology without requiring image processing. The sensor provides a digital output signal that is directly connected to a GPIO input of the STM32 microcontroller. The controller continuously monitors this input signal and performs predefined actions according to the detected motion condition is shown in Figure 2.3 [4].

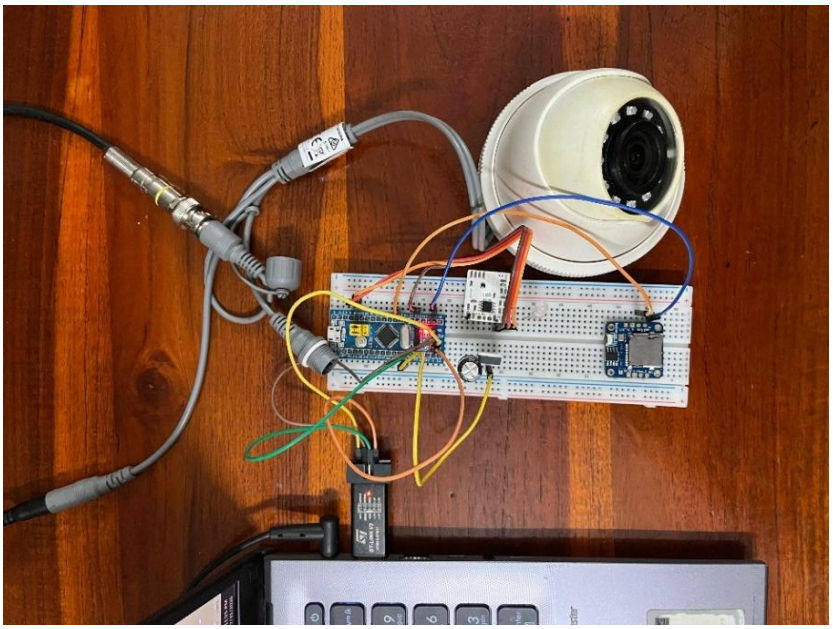


Figure 2.3: Experimental setup of the STM32-based smart CCTV security system prototype

The alert mechanism consists of a blue LED indicator and an audio buzzer circuit. The LED provides visual indication of detected movement, while the buzzer generates an audible warning signal. Since the STM32 GPIO pins cannot directly drive higher current loads, a BC547 transistor driver circuit is used to control the buzzer operation[3].

The electronic circuit design and PCB layout were developed using KiCad software. The schematic design was divided into separate functional sections, including the power supply circuit, microcontroller circuit, sensor interface, alert system, and CCTV switching circuit. Proper component placement, grounding, and power track considerations were followed during PCB development to improve system reliability[4].

In addition to the electronic development, a protective enclosure was designed using SolidWorks 3D CAD software. The enclosure was developed to provide mechanical protection for the PCB and internal components while allowing proper access to external connections such as the power input, CCTV output, sensor interface, and programming connector. The enclosure

design considered component dimensions, mounting locations, cable routing, and ventilation requirements [4].

2.3 Power management and energy optimization method

The power management approach of the proposed system is designed to improve energy efficiency by controlling CCTV operation according to real-time activity. Unlike conventional CCTV systems that remain continuously powered, the proposed system supplies power to the camera only when motion is detected [3-4].

The 12V battery supply is distributed through the power regulation section. The LM2596 converter provides a stable 5V output for peripheral devices, while the AMS1117 regulator supplies the 3.3V operating voltage required by the STM32 controller. Filtering capacitors are included in both regulator stages to minimize voltage fluctuations and improve system stability [3].

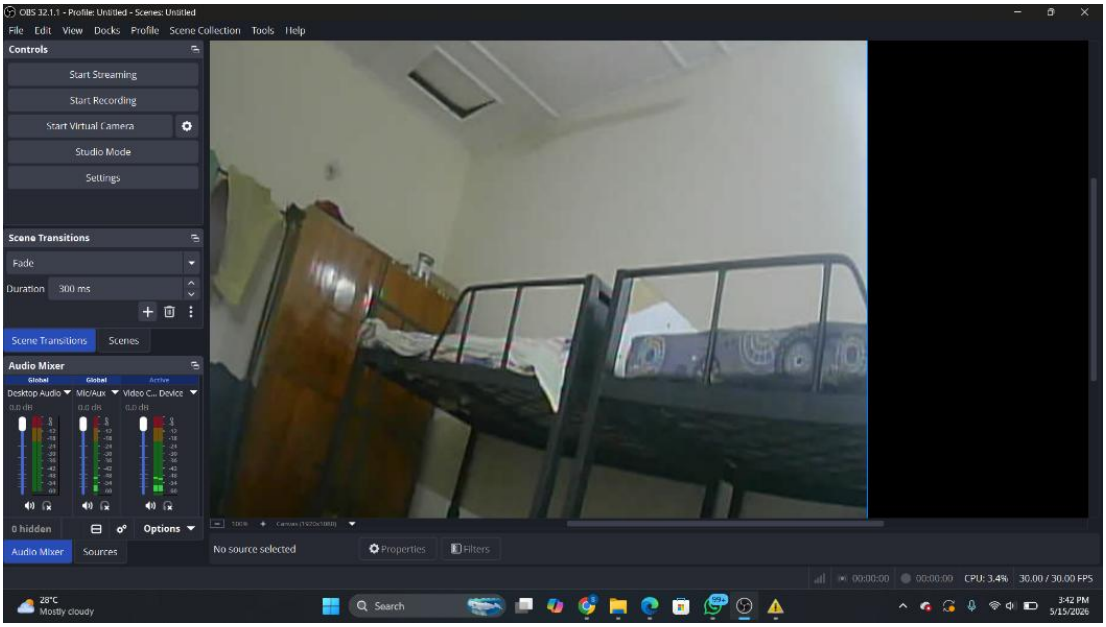


Figure 2.4: Real-time monitoring interface of the CCTV camera system using OBS Studio

The figure 2.4 is shown automatic power control method allows the CCTV camera to remain inactive during periods without detected movement, reducing unnecessary power consumption and improving suitability for battery-powered surveillance applications [3].

2.4 Experimental testing methodology

The developed prototype was evaluated through a series of functional tests to verify the operation of individual hardware sections and the complete integrated system. The testing procedure included verification of power supply outputs, STM32 programming communication, motion sensor response, alert activation, and CCTV power switching operation [4].

The power regulation section was examined to confirm the availability of required voltage levels for different components. The STM32 controller was tested through the ST-LINK interface to ensure successful firmware programming and debugging. The motion detection

system was evaluated by observing the response of the controller when movement was introduced within the sensor detection area [5].

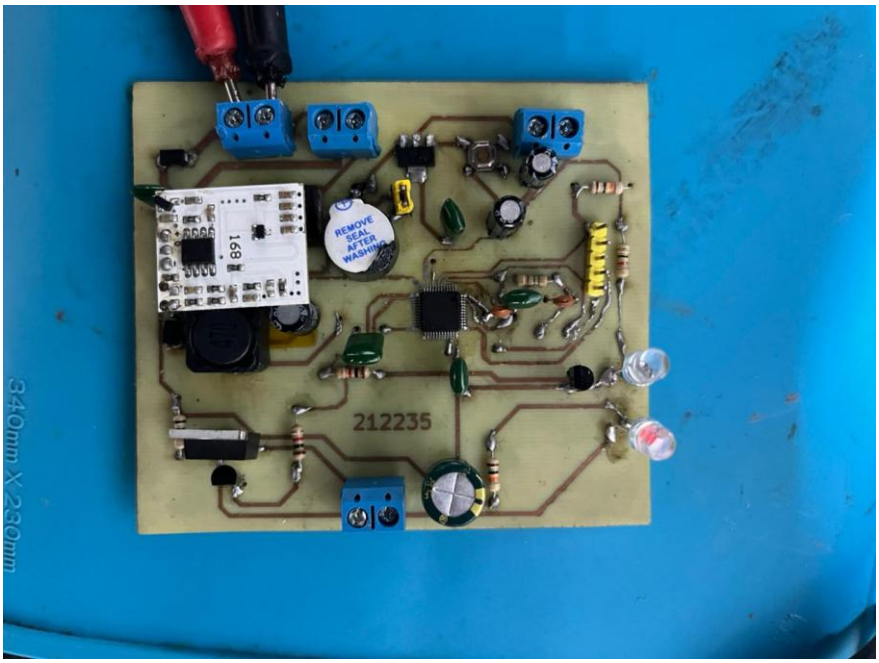


Figure 2.4: Fabricated PCB prototype of the STM32-based smart CCTV enhancement module
The complete system of figure 2.4 testing procedure was conducted by integrating all modules together and verifying the automatic activation and deactivation of the CCTV power supply according to motion detection conditions [5].

No human subjects, animals, or personal data were involved in the experimental process. The motion detection tests were performed only to evaluate the functionality of the developed hardware system. The proposed system was designed for ethical security applications while considering privacy and responsible usage [6].

2.5 Mini FPV DVR and Local Video Storage

A mini FPV DVR module is integrated into the proposed CCTV system to record and store surveillance video during motion-activated operation. The DVR receives the CCTV video signal and stores the recorded footage on a MicroSD card, allowing detected events to be reviewed later. In the experimental setup, the DVR was tested to verify successful video recording and local storage during CCTV activation [1].

3.0 RESULTS AND DISCUSSION

3.1 Electrical and Motion-Control Performance

The developed STM32F103C8T6-based CCTV enhancement module was successfully assembled and tested. The 12 V input supply was regulated to approximately 5 V using the LM2596 converter and 3.3 V using the AMS1117 regulator. The RCWL-0513 successfully provided a digital motion signal to the STM32, which controlled the MOSFET-based CCTV power switching circuit. During motion detection, the CCTV camera, LED indicator and buzzer were activated. When motion was no longer detected, the system maintained CCTV

operation for the programmed approximately 30 s period before switching the camera OFF. The observed switching response was approximately 0.19 s, while the measured timer period was approximately 30.3 s.

Table 3.1: Electrical and Motion-Control Test Results

Parameter	Expected Value	Observed Value	Result
Input voltage	12 V	12.7V	Successful
LM2596 output	5.0V	5.02V	Successful
AMS1117 output	3.3 V	3.27V	Successful
Detection distance	10m	2.5-9m	Successful
CCTV activation response	Fast	0.19s	Fast
Deactivation timer	30s	28.7s	30s continuous

The results confirm that the designed power regulation system is suitable for supplying the required voltage levels for the smart CCTV controller.

3.2 STM32 controller and programming verification

The mini FPV DVR was integrated with the CCTV video path to record surveillance footage when the camera was activated. The recorded video was successfully stored on a MicroSD card and subsequently reviewed, confirming the operation of the local recording function. The STM32 was used for control and did not directly process the CCTV video signal. The integrated system therefore demonstrated motion detection, automatic CCTV power control, visual and audio alerts, and local video recording. Switching the camera OFF during inactive periods provides the intended power-management function; however, a quantitative energy-saving percentage was not calculated because complete system power consumption was not measured. Therefore, the results support the functional achievement of motion-based CCTV power management rather than a quantified energy-saving claim. This interpretation is consistent with the existing research material, which emphasizes that energy savings depend on camera duty cycle and measured system power.

Table 3.2: Overall System Functional Performance

Test Condition / Function	Approx. Observed Result	Assessment
No motion	CCTV OFF, LED OFF, buzzer OFF	Successful
Motion detected	CCTV ON, LED ON, buzzer ON	Successful
Continuous motion	CCTV remains ON	Successful
30 s without motion	CCTV switches OFF	Successful
CCTV video recording	Video recorded by mini FPV DVR	Successful
MicroSD storage	Recorded footage stored	Successful

Overall, the experimental findings demonstrate that the proposed architecture successfully achieves its primary functional objectives. The RCWL-0513 provides the motion input, the STM32 performs the control decision, and the MOSFET controls the CCTV power supply, while the mini FPV DVR provides local event recording and MicroSD storage. The results therefore demonstrate the feasibility of the proposed smart CCTV enhancement module. The same source material recommends using measured detection, switching, timer, power, thermal and reliability results for a stronger quantitative evaluation.

4.0 CONCLUSION

This study successfully developed a smart CCTV enhancement system using an STM32F103C8T6 microcontroller for automatic motion-based CCTV power control. The system integrates the RCWL-0513 microwave motion sensor, MOSFET-based CCTV switching circuit, LED and buzzer alert circuits, regulated power supply, and mini FPV DVR with MicroSD storage.

The experimental results demonstrated an approximate 5-6 m motion detection range, 90% detection rate under the conducted trials, 0.19 s average CCTV activation response, and 30.3 s average deactivation time. The CCTV camera was successfully activated when motion was detected and deactivated after the programmed inactivity period. The LED and buzzer also operated successfully, while the mini FPV DVR successfully recorded and stored CCTV video on the MicroSD card. These results demonstrate that the proposed system achieved its main functional objectives and provides a practical approach for automatic CCTV control and local event recording.

The developed prototype combines KiCad-based electronic design with a SolidWorks-designed enclosure, providing an integrated and compact CCTV enhancement module. The system demonstrates the feasibility of using embedded control and microwave motion detection to automate CCTV operation according to detected activity.

Future development can focus on wireless communication, mobile notifications, AI-based human/object detection, cloud-based monitoring, and further optimization of the power-management system to enhance the functionality and practical applicability of the proposed CCTV system.

ACKNOWLEDGEMENTS

The authors would like to express their appreciation to the Department of Electronics, Faculty of Applied Sciences, Wayamba University of Sri Lanka, Kuliyapitiya, Sri Lanka.

REFERENCES

1. M. H. Jusoh, M. F. Bin Jamali, A. F. Z. Abidin, A. A. Sulaiman, and M. F. Hussin, “Wi-Fi and GSM Based Motion Sensor for Home Security System Apllication,” *IOP Conference Series: Materials Science and Engineering*, vol. 99, p. 012010, Nov. 2015, doi: 10.1088/1757-899x/99/1/012010.
2. Noor, Muhamad, and Norliana Yusof, “Development of a Motion Activated Security Cam for Monitoring Applications,” *SpringerBriefs in applied sciences and technology*, pp. 1–8, Jan. 2024, doi: 10.1007/978-3-031-47727-0_1.
3. Manuals, “RCWL-0513 Microwave Radar Human Body Induction Switch Module - Technical Specifications,”Manuals.plus,Mar.24,2026. https://manuals.plus/m/230c5489379d85846a61f3a69e14c9852dbba06e41f694cfbfcd254635b96cb3.
4. “RM0008 Reference manual STM32F101xx, STM32F102xx, STM32F103xx, STM32F105xx and STM32F107xx advanced Arm ® -based 32-bit MCUs • STM32F10xxx Cortex ® -M3 programming manual (PM0056) • STM32F10xxx Flash memory programming manual (PM0075)
5. “This Is Information on a Product in Full production. STM32F103x8 STM32F103xB,” 2015. Accessed:Aug.10,2026.[Online]. Available:https://www.st.com/resource/en/datasheet/stm32f103c8.pdf
6. “LM2596,” *Ti.com*, 2023. https://www.ti.com/product/LM2596?utm (Accessed Aug. 09, 2026).manual in italics, publisher, year of publication)

Proc. Annual Symposium on Research & Industrial Training, 13 (2026) 23 - 30
Department of Electronics – Wayamba University of Sri Lanka

DESIGN OF A COMPACT HIGH-GAIN PRINTED ANTENNA FOR LONG RANGE (LoRa) COMMUNICATION

E.V.N. Thathsarani*, J.M.J.W. Jayasinghe

Department of Electronics, Wayamba University of Sri Lanka, Kuliyapitiya, Sri Lanka

*thathsaraninavodya160@gmail.com

ABSTRACT

Long Range (LoRa) communication systems operating in the 863-870 MHz ISM band require antennas with suitable radiation characteristics for reliable long-distance communication. High antenna gain is desirable for extending the communication range, while an omnidirectional radiation pattern is preferred for communicating with multiple devices distributed around the transmitter. In compact LoRa devices, the antenna is also required to have a small physical footprint. However, printed antennas operating at sub-GHz frequencies are inherently relatively large, resulting in a trade-off between antenna size and radiation performance. Therefore, this study aims to develop optimized printed dipole antennas that address these requirements. A conventional center-fed printed dipole antenna was initially designed and used as the reference antenna. Subsequently, two modified printed dipole configurations were designed, optimized, and analyzed using Ansys High Frequency Structure Simulator (HFSS), and the prototypes were fabricated. The impedance bandwidths were experimentally evaluated using a vector network analyzer (VNA). The first proposed antenna is a modified Koch fractal dipole with dimensions of 125.7 × 20 mm², developed primarily for antenna miniaturization. It achieved a simulated gain of 2.3 dBi and a measured bandwidth of 100 MHz. Since its gain was relatively limited, a reflector-assisted modified bow-tie dipole antenna with dimensions of 150 × 85 mm² was subsequently developed to enhance the gain. The proposed antenna achieved a simulated gain of 5.1 dBi and a measured bandwidth of 140 MHz.

Keywords: **D**ipole antenna, **K**och Fractal, **R**eflector

1.0 INTRODUCTION

Long Range (LoRa) communication technology is widely used in Internet of Things (IoT) applications because of its long range of communication and low power consumption [1,2]. Antenna plays an essential role in determining the communication range and the reliability of LoRa communication system [2,3]. However, antennas that work at 868MHz are typically bulky in size due to lower frequencies and make it hard to integrate into small devices [4]. It becomes necessary to obtain miniaturized printed antennas while maintaining their performance in terms of gain and bandwidth [2].

There are many ways that have been investigated to minimize the size of the antennas, such as folding, meandering, fractal structures, and modification of the radiating elements of antennas. All these methods are useful to miniaturize the antennas [2,5,6]. Due to this reduction of the antenna sizes, the antenna gain and efficiency decrease. The fractal Koch structures provide increased electrical current paths in less physical length [5,6]. Likewise, the bow tie antennas offer great flexibility in adjusting the geometry and impedance of the antenna, while reflectors are useful in improving the directivity and gain. Hence, it is an important requirement for 868 MHz LoRa applications to achieve an appropriate trade off among antenna parameters such as size, bandwidth, and gain.

In this study, two optimized printed dipole antennas for 868 MHz LoRa applications are introduced. These structures have been fabricated and then tested using Vector Network Analyzer (VNA).

2. EXPERIMENTAL

2.1 Antenna design methodology

The reference antenna was chosen as a center fed conventional printed dipole because of its simple and balanced nature, and ability to be manufactured using printed circuit board (PCB). Free space wavelength in the target region was determined as [7];

$$\lambda_0 = \frac{c}{f_0} \quad [2.1]$$

Where;
c = The velocity of electromagnetic waves in free space, f_0 = The operating frequency

At 868 MHz, $\lambda_0$is approximately 345.6 mm, The initial half wave dipole length was calculated as [7];

$$L_{\text{dipole}} = \frac{\lambda_0}{2} \quad [2.2]$$

Where;
L_{dipole} = The initial half wave dipole length

Hence the length of linear dipole antenna is 172.8 mm for free space.

For an FR4 dielectric substrate with a dielectric constant of $\epsilon_r = 4.4$, the effective dielectric constant can be approximated as [5];

$$\epsilon_{\text{eff}} = \frac{1+\epsilon_r}{2} \quad [2.3]$$
$$\epsilon_{\text{eff}} = 2.7$$

Therefore, the approximate dipole length (L) for the FR4 material is calculated as [5];

$$L = \frac{L_{\text{dipole}}}{\sqrt{\epsilon_{\text{eff}}}} \quad [2.4]$$
$$L \approx 108\,\text{mm}$$

The half wave dipole length for the FR-4 material was considered as the theoretical starting point. The corresponding printed dipole was then designed on the 1.6 mm thick FR-4 substrate and optimized using High Frequency Structure Simulator (HFSS) software to obtain the required operating characteristics. As this conventional antenna exhibits a narrow bandwidth and a low gain, while its length is incompatible to be installed in a small device, performance enhancement techniques were applied.

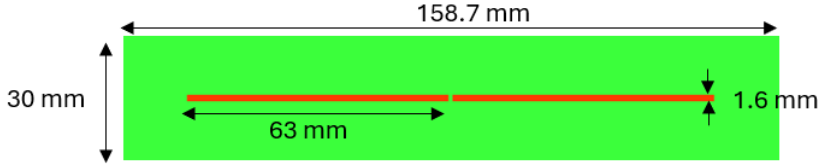


Figure 2.1: Geometry and dimensional parameters of the conventional printed dipole antenna simulated on a 1.6 mm thick FR-4 substrate for 868 MHz operation.

The first modification involved a modified Koch dipole with the aim of reducing its size while increasing the gain, and the second modification involved a modified bow tie dipole with a printed reflector for increasing gain. The geometrical parameters of these designs were parametrically optimized considering resonance, S_{11}, impedance bandwidth, and realized gain.

2.2 Modified Koch printed dipole design

The modified Koch dipole was developed to reduce the end-to-end length of the dipole arm and the size of the substrate without using parasitic elements. The parameters for the angle and the number of iterations were varied in order to maximize the effective path of current with a reduced physical size. The optimum geometry used a 50°first angular section close to the feed followed by 45°sections. The final antenna dimensions and geometrical parameters are shown in figure 2.2. As the gain of this compact antenna was limited, a modified bow tie dipole with printed reflector was designed.

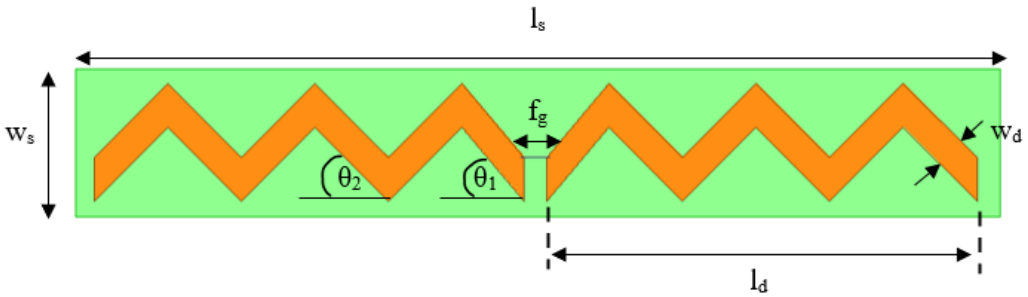


Figure 2.2: Geometry and dimensional parameters of the proposed modified Koch printed dipole antenna.

Table 2.1: Dimensions of the proposed modified Koch printed dipole antenna.

Parameter	Dimension
l_s	125.7 mm
w_s	20 mm
l_d	58.5 mm
w_d	4 mm
f_g	3 mm
θ_1	50°
θ_2	45°

2.3 Modified bow tie dipole with printed reflector

The geometry was designed for gain improvement by gradually converting the conventional dipole to a bow tie radiator. Straight feed to flare length, gradual widening of the arms, flaring dimensions, and rounded outer terminations of the antenna were optimized parametrically using HFSS. The best bandwidth and radiation properties were obtained for the selected combination.

A Copper reflector was added to the PCB on the opposite side [8]. Length, width, and positioning of the reflector relative to the driven element were optimized, and the length of the reflector was selected to be approximately 97% of the dipole length. The optimized geometries of the radiator and reflector are shown in figure 2.3.

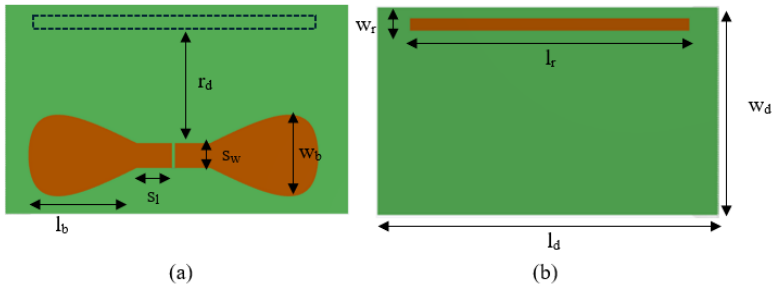


Figure 2.3: Geometry and optimized dimensional parameters of the proposed modified bow tie dipole antenna (a) Radiator (b) Backside

Table 2.2: Dimensions of the proposed modified bow tie dipole antenna with a reflector

Parameter	Dimension (mm)
r_d	47
l_b	47
w_b	22
s_w	10
s_l	15
w_r	5
l_r	120
w_d	85
l_d	150

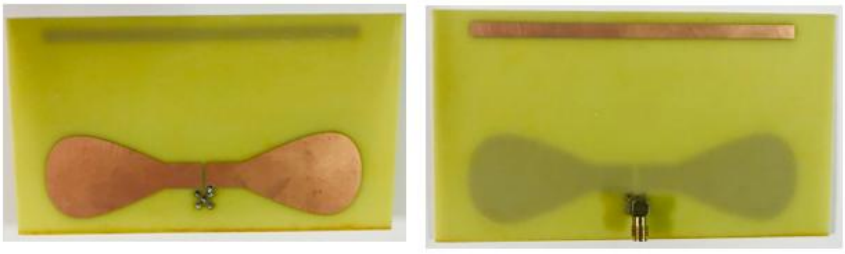
2.4 Simulation, fabrication and measurement

Both proposed antennas were optimized and modeled using Ansys HFSS. The simulations evaluated S_{11}, impedance bandwidth realized gain and radiation characteristics. After improving the design, the Koch antenna and the reflector assisted bow tie antenna were fabricated on 1.6 mm-thick FR-4 substrates with a relative dielectric constant (ε_r) of 4.4 and 35 µm-thick copper layers and 50 Ω SMA connectors were attached at the feeding points. The fabricated prototype antennas are shown in figure 2.4 and figure 2.5.



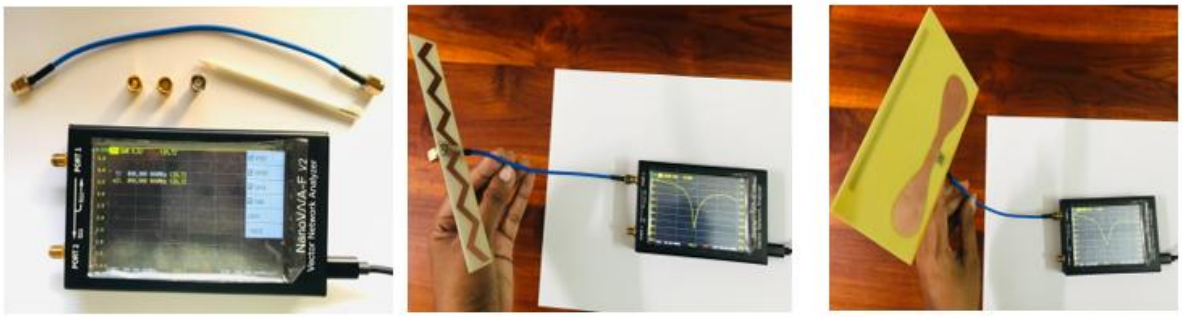
Figure 2.4: Fabricated modified Koch printed dipole antenna

The experimental S_{11}characteristics were obtained using Vector Network Analyzer (Model: NanoVNA-F V2). Calibration of VNA was performed for the selected frequency range before connecting any of the antennas via the 50 Ω SMA port. Arrangement of VNA calibration and measurements is shown in figure 2.6.



(a) (b)

Figure 2.5: Fabricated bow tie dipole antenna (a) Radiator, and (b) Reflector.



(a) (b) (c)

Figure 2.6: S_{11} measurement (a) Calibration setup of the NanoVNA-F V2 (b) Experimental S_{11} measurement setup of fabricated modified Koch printed dipole and (c) Experimental S_{11} measurement setup of reflector assisted modified bow tie dipole.

3. RESULTS AND DISCUSSION

3.1 Bandwidth

The comparison of the simulated and measured S_{11}responses for the proposed antennas is shown in figure 3.1. The modified Koch antenna achieved simulated and measured −10 dB bandwidths of 864 MHz-966 MHz and 820 MHz-920 MHz, respectively. Similarly, the reflector-assisted bow-tie antenna exhibited simulated and measured bandwidths of 819 MHz-878 MHz and 740 MHz-880 MHz, respectively.

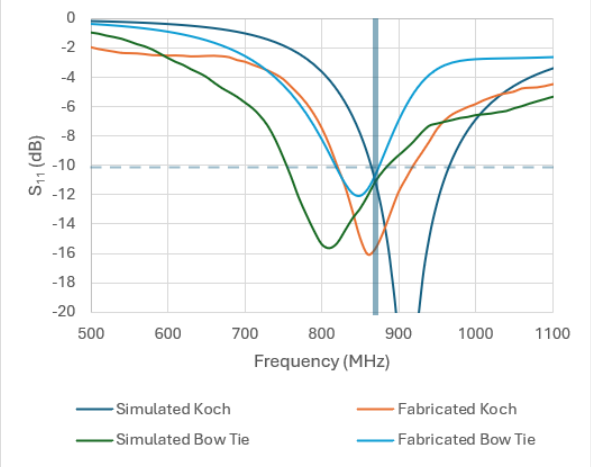


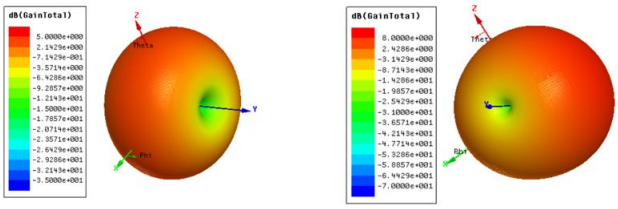
Figure 3.1: simulated and measured S_{11}characteristics of the modified Koch and reflector assisted bow tie antennas with highlighted 863-870 MHz target LoRa operating band.

All simulated and fabricated antennas exhibited S_{11} below −10 dB throughout the required 863–870 MHz LoRa operating band, confirming satisfactory impedance matching across the target frequency range.

3.2 Gain

The simulated 3D gain patterns at 868 MHz are given in figure 3.2. The modified Koch fractal antenna demonstrated a maximum gain value of 2.3 dBi, in comparison with 2.1 dBi for the

conventional dipole reference antenna, even though the size was reduced. The reflector assisted bow tie dipole achieved a gain of 5.1 dBi, which represents an approximately 3.0 dB gain improvement in comparison with the conventional dipole antenna. This improvement is mainly due to the optimized flared shape of the radiator and the directional influence of the printed reflector.

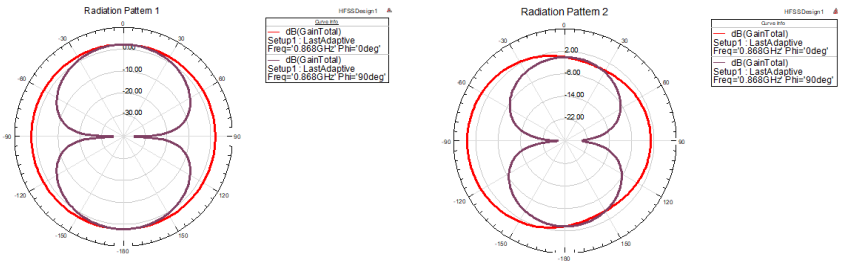


(a) (b)

Figure 3.2: Simulated 3D gain distributions at 868 MHz: (a) modified Koch dipole and (b) reflector assisted bow tie dipole.

3.3 Radiation pattern

Figure 3.3 shows the modeled radiation patterns at 868 MHz. Both the modified Koch dipole and the reflector assisted bow tie dipole exhibit omnidirectional radiation patterns in the investigated planes.



(a) (b)

Figure 3.3: Simulated total gain radiation patterns at 868 MHz in the $\phi = 0°$and $\phi = 90°$planes: (a) modified Koch dipole and (b) reflector assisted bow tie dipole.

3.4 Theoretical communication range estimation

The theoretical communication range was estimated using the Friis transmission equation under ideal free space line of sight (LOS) conditions [9].

$$P_r = P_t G_t G_r \left(\frac{\lambda}{4\pi d}\right)^2 \quad [3.1]$$

Where;
P_t= Transmit power , P_r= Receiver sensitivity, G_t= Gain of the transmitting antenna
G_r= Gain of the receiving antenna, λ= Wavelength, d= Communication distance

The free space path loss ($FSPL$) is obtained as;

$$FSPL = P_t + G_t + G_r - P_r - L_m \quad [3.2]$$

Where;
L_m= Additional practical loss/margin

Hence, the distance can be obtained from;

$$d = \left(\lambda/(4\pi)\right)10^{(FSPL/20)} \quad [3.3]$$

For the theoretical communication range estimation, the RAK11720 LoRa module, which is based on the Semtech SX1262 transceiver, was considered as the communication module. The communication range was estimated for the two proposed antennas considering the theoretical and practical operating scenarios using the Friis transmission equation under the assumptions given in Table 3.1 [9,10,11]. The resulting communication ranges are summarized in Table 3.2.

Table 3.1: Assumptions used for theoretical communication range estimation

Parameter	Theoretical operation	Practical operation
Frequency	868 MHz	868 MHz
Transmit power	+22 dBm	+14 dBm
Receiver sensitivity	-137 dBm	-130 dBm
Receiving antenna	0 dBi	0 dBi
Propagation	Free space LOS	Free space LOS
Additional practical loss/margin	40 dB	40 dB

Table 3.2: Estimated theoretical communication range

Antenna	Theoretical operation	Practical operation
Modified Koch	32 km	5.7 km
Modified Bow tie	44 km	7.8 km

3.5 Performance comparison

Table 3.3 below shows the performance of the conventional and proposed antennas. The modified Koch antenna results in the decrease of the substrate area from 5061mm² to 2514mm², which is equivalent to 49.7% of area reduction. At the same time, the modified gain is improved by 0.2dBi, resulting in gain of 2.3 dBi. In contrast, the reflector assisted bow tie antenna focuses more on the gain aspect and manages to achieve 5.1 dBi, which is 3.0 dB higher compared to the conventional antenna.

Table 3.3: Performance comparison of the conventional and proposed printed dipole antennas.

	Bandwidth (MHz)	Gain (dBi)	Gain enhancement (%)	Substrate size (mm x mm)	End to end length of each arm (mm)
Conventional dipole	66	2.1	Reference	158.7 × 30	63
Simulated koch antenna	102	2.3	+9.5%	125.7 × 20	58.5
Fabricated koch	100	-	-	125.7 × 20	58.5
Simulated bow tie	59	5.1	+142.9%	150 × 85	62
Fabricated bow tie	140	-	-	150 × 85	62

4. CONCLUSION

In this paper, two printed dipole antennas were optimized for LoRa applications around 868 MHz, aiming at compactness and gain enhancement. The modified Koch dipole showed a

47.2% reduction in substrate area when compared to the conventional dipole, having a simulated gain of 2.3 dBi, and measured bandwidth 100 MHz. The reflector assisted modified bow tie antenna showed a simulated gain of 5.1 dBi, which is approximately 3 dB increase in gain in comparison with the conventional reference dipole antenna, with measured bandwidth 140 MHz. All the fabricated antennas could effectively cover the targeted 868 MHz operating frequency. It can be concluded that the Koch dipole antenna leads to an efficient way for miniaturizing antennas without reduction in radiation properties. On the other hand, the bow tie antenna design assisted with a printed reflector shows considerable gain increase. Therefore, the proposed designs offer practical alternatives for compact and enhanced gain 868 MHz LoRa applications.

ACKNOWLEDGEMENTS

The authors would like to express their sincere gratitude to the academic and supporting staff of the Department of Electronics, for their support, and laboratory facilities. The authors also sincerely thank Senior Lecturer Mrs. Shyama Wickramasinghe for her support in providing the measurement facilities and for her guidance in carrying out the antenna measurements.

REFERENCES

1. Al-Shareeda, M. A., Alsadhan, A. A., Qasim, H. H. and Manickam, S., Long range technology for internet of things: review, challenges, and future directions. *Bulletin of Electrical Engineering and Informatics* 12/6, (2023), 3758–3767, doi: 10.11591/eei.v12i6.5214.
2. Bhardwaj, S., Malik, P. K., Gupta, A. and Singh, R., Real-time implementation of a novel design approach for sub-GHz long-range antenna for smart Internet of Things communication. *International Journal of Antennas and Propagation* 2023/1, (2023), Article 8602885, doi: 10.1155/2023/8602885.
3. Yahya, M. S., Soeung, S., Abdul Rahim, S. K., Geok, T. K. and Musa, U., Machine learning-optimized wearable antenna for LoRa localization. *IEEE Access* 12, (2024), 139237–139252, doi: 10.1109/ACCESS.2024.3457808.
4. Yang, Y., Vermeeren, G. and Joseph, W., Design of a compact 868 MHz on-body matched antenna for relaying biomedical implants. *Proc. 19th European Conference on Antennas and Propagation (EuCAP)*, Stockholm, Sweden, (2025), doi: 10.23919/EuCAP63536.2025.10999965.
5. Gadgil, C., Development and simulation of Koch dipole antenna for 868 MHz. *International Journal of Creative Research Thoughts* 12/4, (2024), g394–g396.
6. Halouani, M., Oueslati, D., Laadhar, L. and Rmili, H., Design approach of fractal antenna for passive dual UHF band RFID tag. *Proc. 13th Mediterranean Microwave Symposium (MMS)*, Saida, Lebanon, (2013).
7. Zingg, R., *Printed Dipole Antenna*. Boulder, CO, USA: University of Colorado at Boulder, (2000).
8. Abu Hussin, F., Ahmad, B. H., Abd. Aziz, M. Z. A. and Suaidi, M. K., Modified printed dipole with reflector and director. *Jurnal Teknologi* 78/6-4, (2016), 137–140, doi: 10.11113/jt.v78.8989.
9. Shaw, J. A., Radiometry and the Friis transmission equation. *American Journal of Physics* 81/1, (2013), 33–37, doi: 10.1119/1.4755780.
10. RAKwireless, *RAK11720 WisDuo LPWAN+BLE Module Datasheet*. Online. https://docs.rakwireless.com/product-categories/wisduo/rak11720-module/datasheet/ (Accessed 2026-08-05).
11. Ahmad, Z., Hashim, S. J., Ferré, G., Rokhani, F. Z., Al-Haddad, S. A. R. and Sali, A., LoRa and rotating polarization wave: physical layer principles and performance evaluation. *IEEE Access* 11, (2023), 14892–14905, doi: 10.1109/ACCESS.2023.3242552.

Proc. Annual Symposium on Research & Industrial Training, 13 (2026) 31 - 38
Department of Electronics – Wayamba University of Sri Lanka

LOW-COST FPGA-BASED REAL-TIME NEAR-FIELD ELECTROMAGNETIC NOISE SPECTRUM ANALYZER USING A SPARTAN-3E

P.M.I. Nimanthini* and W.A.S. Wijesinghe

Department of Electronics, Wayamba University of Sri Lanka, Kuliyapitiya, Sri Lanka

**nimanthini2001@gmail.com*

ABSTRACT

There are numerous sources of electromagnetic noise in electronic systems, and observing these signals may be helpful to understand the behavior of these systems. In this paper, a low-cost FPGA-based system for detection and visualization of near-field electromagnetic noise and its spectral activity is presented. The system includes the custom-made coaxial loop probe, two-stage amplifier, input protection circuit, the on-board ADC of a Xilinx Spartan-3E Starter Kit, FPGA-based signal processing, and the VGA display. With this system, the near-field electromagnetic noise can be detected from the device under test without electrical contact with the device. The detected weak signal is amplified and processed before feeding it into FPGA ADC for further acquisition and visualization of the signal behavior on the display screen. The gain of the implemented analogue amplifier was experimentally measured with a function generator and digital oscilloscope and was found to be equal to approximately 98, while theoretically the expected gain was 100. Moreover, the experimental impedance of the fabricated probe was examined over the considered frequency range. As the experimental results show, the developed prototype was able to detect, amplify and visualize near-field signals and their behavior on the display screen. Because the designed probe and analogue front end were not calibrated, this system was meant to be used for qualitative observation of near-field electromagnetic noise.

Keywords: **E**lectromagnetic noise, **F**PGA, **R**eal-Time Signal Analysis

1.0 INTRODUCTION

With an increase in the number of electronic systems, there is also an increase in the likelihood of electromagnetic interference (EMI) occurrence in modern electronic environments. Computers, switching power supplies, communication devices, electric motors, and many other electronic circuits produce electromagnetic emissions in the process of their functioning. Information obtained by the means of observation of such emissions can be useful in studying the electromagnetic characteristics of electronic systems [1,2]. Thus, the observation of near field electromagnetic activity can be useful both for educational purposes and for troubleshooting and preliminary research of electromagnetic behavior of electronic systems.

Frequency domain measuring equipment such as spectrum analyzers and specialized EMC measuring equipment provides precise and wideband measurements. However, this type of measuring equipment is rather expensive and is usually used only in laboratories. Thus, the need arises for inexpensive experimental equipment to measure and compare the electromagnetic activity.

Since Field-Programmable Gate Arrays (FPGAs) are characterized by the availability of low-latency and parallel-processing, they serve as a perfect medium for acquiring and processing digital samples of data in real time [3,4]. Thus, FPGAs can be used to capture analogue signals, process digital samples, and visualize acquired data. However, developing a low-cost system which includes a fabricated near-field probe, analogue signal conditioning, ADC acquisition,

FPGA processing, and real-time visualization is a good solution for qualitative observation of electromagnetic activity.

The major contribution of this project lies in the development of a low-cost prototype system consisting of a fabricated coaxial loop probe, a two-stage analogue amplifier, an input protection circuit, an ADC of the Spartan-3E Starter Kit, FPGA processing, and VGA display. This project is focused on qualitative and comparative observation of near-field electromagnetic signals. Since neither the probe nor analogue part of the measurement system are calibrated, the project is not aimed at replacing calibrated spectrum analyzers and EMC measuring devices.

Thus, the purpose of this research is to design and construct a low-cost coaxial loop detector that can detect electromagnetic waves from the electronic devices around, to design an analogue signal conditioning and protection circuit for the weak detected signals to be able to interface with the Spartan-3E Starter Kit ADC, to obtain and process the detected signal using the Spartan-3E FPGA, and to have real-time visualization of the detected signal and its spectrum activity using the VGA display. In addition, the evaluation of the designed prototype will be carried out as a low-cost qualitative system for near-field EM activity observation.

2.0 METHODOLOGY

2.1 System overview

The proposed system was designed for detection, processing, and visualization of electromagnetic interference produced by nearby electronic equipment in real-time. The system comprises four major components: EM probe, analog frontend, FPGA processor, and VGA display. The block diagram of the entire system is shown in Figure 1 below.

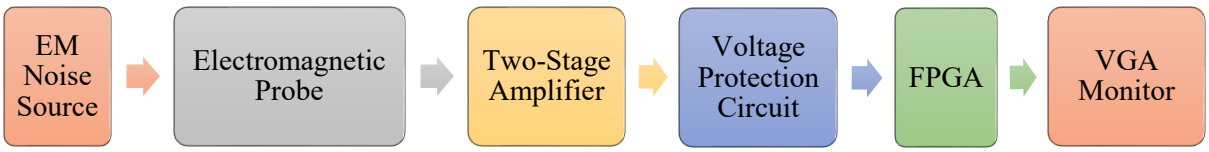


Figure 1: Block diagram of the system

The first component of the system under consideration is the electromagnetic probe that detects the EM interference from the nearby electronic equipment. A loop probe was fabricated from the coaxial cable. Placing the probe near the electronic equipment will help to capture the EM interference from the equipment without any electrical connection. The output signal from the probe is quite weak and cannot be fed directly into the FPGA. Therefore, the received signal is then transmitted to the signal conditioning circuit. This circuit uses a two-stage amplifier, which comprises LM 741 operational amplifiers. One of the major objectives of the amplifier is to amplify the low-amplitude electromagnetic wave while retaining its waveform. Additionally, a voltage protection circuit is employed to ensure that the signal level does not exceed the safe voltage input limit of the FPGA. In preparation for connection to the FPGA, the performance of the amplifier was tested using a function generator and a digital oscilloscope.

The amplified analog signal is then sent to the Analog to Digital Converter (ADC) of the Spartan-3E Starter Kit. The analog voltage is then converted into digital values, which are

subsequently processed by the FPGA. The FPGA keeps reading the digital samples and storing them temporarily for waveform generation. Verilog HDL was used to program the FPGA on Xilinx ISE 14.7. The FPGA also includes a VGA controller that produces the HSYNC and VSYNC signals needed for the VGA display. With the help of sampled values of ADC, the VGA controller plots the waveform based on the pixel values for plotting the waveform. With the arrival of new ADC sampled values, the waveform plot is updated in real time and thus, the changes in the electromagnetic noise are visible to the user instantly.

The whole system functions continuously from the moment of the acquisition of the signal until its plotting on the screen. Firstly, the EM probe receives the electromagnetic signal. Secondly, the amplifier boosts the signal level and passes it to the ADC. Then the FPGA analyzes the digital samples and produces the signals for the VGA monitor. In the end, the plot of electromagnetic noise is displayed on the monitor screen.

2.2 Near-field probe and analogue front end

The hardware setup includes three major parts: the EM probe, two-stage amplifier, and voltage protector circuit. These parts are applied to sense weak near-field signals, amplify them, and generate appropriate input signal for the FPGA.

Loop-type near-field probe was implemented through the use of coaxial cable. Unbalanced loop probe design with a gap in the neck was used, see Figure 2. The loop part of the coaxial cable was used as the detector of magnetic-field-based near-field electromagnetic activities of the nearby electronic devices. Such a design allowed for simple and cheap implementation of electromagnetic signals comparison without electrical connection to the tested device. During experimental observation, the probe was placed near electronic devices to capture their electromagnetic emissions. The output signal was measured depending on the observation conditions, especially the position of the probe relative to the source. Hence, the signal amplitude should be considered as a relative measure of the electromagnetic field. Present prototype is not calibrated for the absolute measurement of the electromagnetic field.

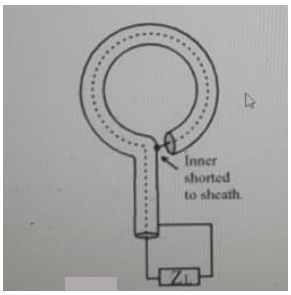


Figure 2: Reference loop configurations and the selected unbalanced loop design with a gap at the neck used to fabricate the proposed EM probe [5].

The weak signal obtained from the EM probe was amplified through a two-stage amplifier circuit using the LM741 operational amplifier. This is because the LM741 operational amplifier is one of the commonly used op-amps capable of providing voltage gain to low-level analog signals for effective amplification. The first stage ensures an amplification of the weak signal, while the second stage ensures an additional amplification of the already amplified signal for better output signals. The resistor and capacitor values were set for the provision of stable amplification at the required frequency range without signal distortion. The amplifier was

tested using a function generator and a digital oscilloscope before integration with the FPGA. Performance tests on the amplifier before sending the output signal to the FPGA were carried out using the function generator and the digital oscilloscope. Various frequencies were applied to the amplifier to examine the output waveforms. The output signals were observed to be amplified to produce high output levels without losing the waveform characteristics. The amplified output represents the waveform of the electromagnetic noise better. The simulated circuit diagram of the amplifier is shown in figure 3.

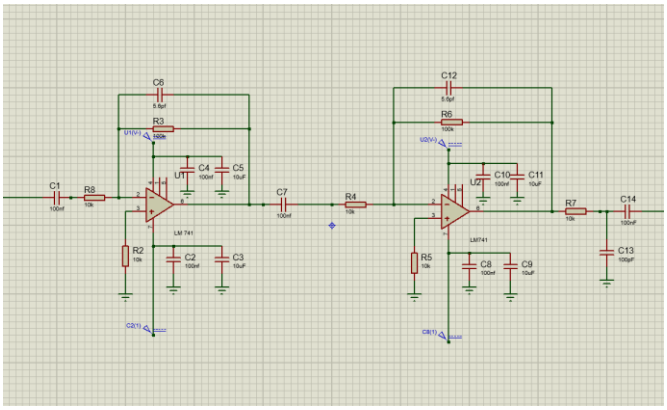


Figure 3: Simulated circuit diagram of the amplifier

There was inclusion of protection circuitry between the two-stage amplifier's output and the analog input header (J7) on the FPGA board. As the operational amplifier works using 12 V dual supply, the output voltage of the operational amplifier could go beyond the limits of the input voltages of the board in the presence of strong electromagnetic pulses. In the Spartan-3E Starter Kit board, the input analog voltage is applied to an integrated LTC6912-1 Programmable Pre-amplifier and an integrated LTC1407A-1 14-bit Analog-to-Digital Converter (ADC). The ADC has an input voltage range of 1.25 V based on the internal 1.65 V DC reference voltage (with an active input voltage window of 0.4 V to 2.9 V at unity gain). The absolute maximum input voltages for the on-board ICs are limited to a range of -0.3 V to +3.3 V [6]. Figure 4 illustrates the schematic diagram of the protection circuit used in the proposed system.

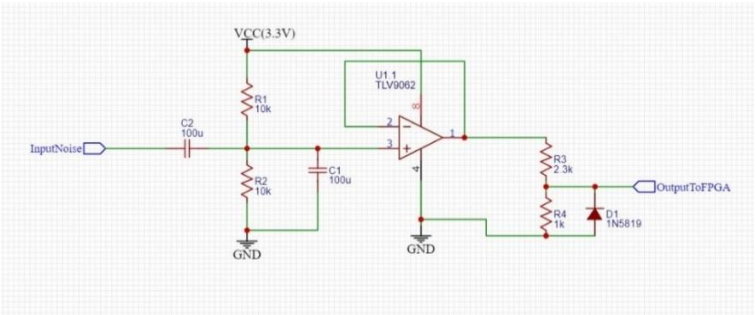


Figure 4: Simulated circuit diagram of the voltage protection circuit

2.3 FPGA acquisition and FFT processing

The increased EM noise signal is processed on a Spartan-3E FPGA board. An ADC of the FPGA is employed to digitize the received analog signal that can be further processed. The FPGA is programmed by means of Verilog HDL to implement the ADC data acquisition procedure and necessary signal processing operations. The main goal of FPGA realization is the analysis of the detected EM noise signal and processing of the received data for its

visualization. In order to visualize the processed signal, a VGA controller is implemented in the FPGA to display the processed signal on a VGA monitor. VGA controller creates the necessary horizontal and vertical synchronization signals to control the display. The signal data from the ADC is transformed into pixel information and the EM noise waveform is displayed on the monitor screen. It allows observing the properties of the detected noise signal like signal variations and its frequency behavior without additional measurement equipment.

3.0 RESULTS AND DISCUSSION

3.1 EM Probe Observation

The fabricated EM coaxial loop probe could measure EM noise that emits from different electronic devices surrounding it without the use of any electrical connection between the EM probe and the electronic devices. Figure 5 shows the constructed EM probe used in the proposed system to detect near-field electromagnetic noise signals.



Figure 5: Constructed custom EM probe

The impedance of the EM probe was then calculated for the frequency range under consideration and the graph is shown in Figure 6. The graph represents the impedance of the probe as a function of frequency.

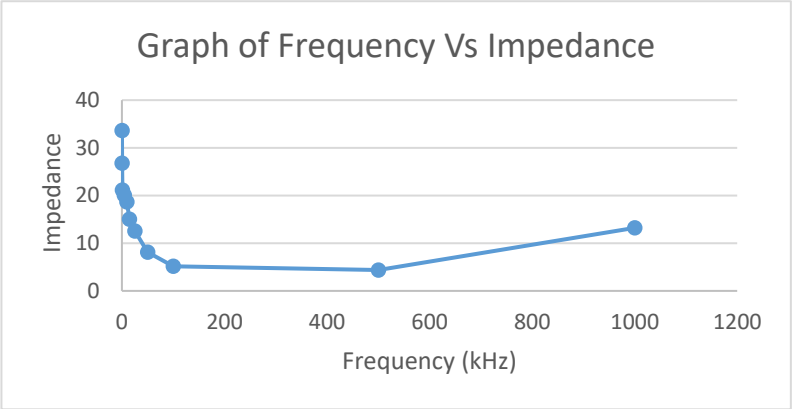
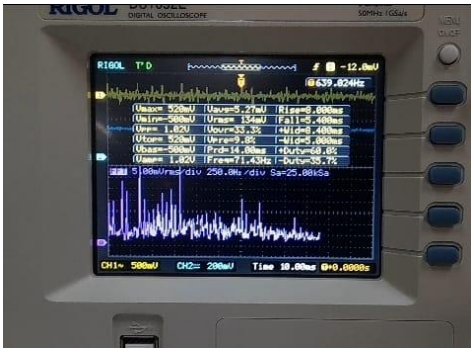


Figure 6: Graphical representation of impedance of the EM probe

In the probe tests, variations in the measured signal were noted depending on the probe's location relative to electronic devices. Specifically, the amplitude of the detected signal depends on the proximity of the probe to the source of electromagnetic activity. With increased distance of the probe from the source of activity, there would be reduced coupling between the probe and the electromagnetic activity in its vicinity. As a result, the detected signal would be relatively weak. Conversely, with decreased distance, there would be strong coupling leading to increased detection signal amplitude. The positioning and distance of the probe affect the

detected signal. In view of this, comparative measurements must be made using the same probe positioning and arrangement. The current results show that the developed probe is capable of qualitatively detecting electromagnetic activity, but not quantitative field strength measurements. During the testing of the EM probe, the probe was placed near different electronic equipment, which produced some output signals in the EM probe. The amplitude of the signal measured depended on the distance between the measurement point and the source of EM activity. Figure 7 illustrate the FFT spectrum of the electromagnetic noise observed



using the fabricated custom EM probe

Figure 7: FFT spectrum of the electromagnetic noise observed using the fabricated custom EM probe

3.2 Amplifier Circuit Performance

The two-stage amplifier based on LM741 successfully amplified the weak EM signal while preserving its waveform. Figure 8 shows the Hardware implementation of Amplifier.

Figure 8: Hardware implementation of Amplifier

The amplifier was tested using the function generator and the digital oscilloscope prior to the connection with the FPGA. The amplifier was designed with a theoretical voltage gain of 100. The actual gain measured experimentally was around 98, which is very close to the theoretical gain. Therefore, it has been proved that the amplifier behaves according to its design and is appropriate for signal conditioning in the suggested system. The figure 9 shows the relationship between frequency and gain of the amplifier

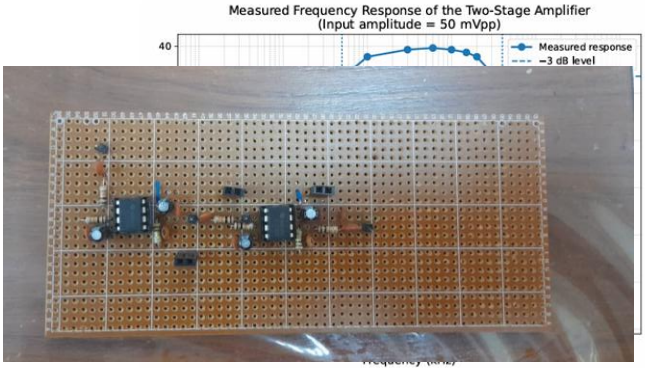


Figure 9: Measured frequency response of Amplifier

3.3 FPGA and VGA Display Results

The conditioned electromagnetic signal was successfully captured by the Spartan-3E FPGA and displayed on the VGA screen. The FPGA took the digitized data from the ADC, processed it and produced the necessary VGA synchronization signals.

The spectrum displayed on the VGA screen was additionally verified through the use of a digital oscilloscope to determine the detected signal behavior. The obtained results prove that the deviations and frequency-dependent features of the signal displayed by the FPGA correspond to those of the signal measured through the oscilloscope. The real-time spectrum of the detected electromagnetic signal displayed on the VGA screen is presented in Figure 10 below.

Thus, the results provide confirmation that all components were integrated properly and successfully worked together. Consequently, the created system can be used for the comparative real-time observation of near-field electromagnetic spectrum activity. Nevertheless, since the EM probe and analogue front end are not calibrated, the obtained spectrum cannot be regarded as an accurate electromagnetic field measurement.



Figure 10: Real-time FFT spectrum of the detected electromagnetic noise displayed on the VGA monitor using the Spartan-3E FPGA.

3.4 Complete System Prototype

The entire hardware system was accomplished by incorporating the EM probe, signal conditioning circuit, protection circuit, FPGA development board, and VGA monitor. The entire system shows how the real-time acquisition, processing, and display of electromagnetic noise signals. Figure 11 shows the overall hardware implementation of the system.



Figure 11: Overall hardware implementation of the system

3.5 Capabilities and limitations

This developed system is capable of detecting weak near-field EM radiation and analyzing its frequency-domain behavior in real time. The homemade coaxial-loop probe offers an easy and cost-effective approach to detecting EM radiation without any physical contact. This is due to the fact that the FPGA unit is responsible for performing the ADC acquisition and FFT computation, while the VGA monitor allows visualization of the detected spectrum.
Nevertheless, there are certain drawbacks of the system. But the developed probe and analogue front-end were not calibrated yet, and hence the measured signal is affected by factors such as the distance between the source and the probe, the position of the probe, orientation, and frequency. Further development can improve its measurement capability by compensating for the frequency response of the analogue front end and by introducing frequency calibration for the FFT display. Calibration of the EM probe and refinement of the analogue signal-conditioning stage would also enable more consistent comparison of measured spectra. These improvements could extend the system toward more quantitative electromagnetic measurement applications.

4 CONCLUSION

This study developed a low-cost FPGA-based system for real-time qualitative observation of near-field electromagnetic activity. This system consists of a customized coaxial loop probe, two-stage amplifier, protection stage, Spartan-3E FPGA with ADC, and a VGA monitor. The experimental gain of the amplifier was found to be about 98, while the signal and spectrum being measured and visualized were verified with an oscilloscope. The obtained results show that the designed system allows for detecting and visualization of the relative near-field spectrum in real-time mode. However, as the probe and analogue front-end are not calibrated, the described system may be used for qualitative observations only.

ACKNOWLEDGEMENTS

The authors are grateful to all the academic and non-academic staff of the Department of Electronics, Faculty of Applied Sciences, Wayamba University of Sri Lanka for their help and support in this study.

REFERENCES

1. Paul, C. R., *Introduction to Electromagnetic Compatibility*, 2nd Ed., New York, John Wiley & Sons, (2005), doi: https://doi.org/10.1002/0471758159.
2. Ott, H. W., *Electromagnetic Compatibility Engineering*, Hoboken, NJ, John Wiley & Sons, (2009), doi: https://doi.org/10.1002/9780470508510.
3. Brown, S., Vranesic, Z., *Fundamentals of Digital Logic with Verilog Design*, 3rd Ed., New York, McGraw-Hill, (2009).
4. Meyer-Baese, U., Meyer-Baese, A., *Digital Signal Processing with Field Programmable Gate Arrays*, Berlin, Springer, 2001, doi: https://doi.org/10.1007/978-3-662-04613-5.
5. Ediss, R. *Probing the Magnetic Field Probe*, Philips Semiconductors, UK. Online. https://www.uniteng.com/neildocs/references/Probing_the_Magnetic_Field_Probe.htm (Accessed 2026-07-31).
6. Xilinx, *Spartan-3E FPGA Starter Kit Board User Guide*, UG230, Version 1.2, 2011. Online. https://docs.amd.com/v/u/en-US/ug230 (Accessed 2026-07-31).

Proc. Annual Symposium on Research & Industrial Training, 13 (2026) 39 - 46
Department of Electronics – Wayamba University of Sri Lanka

REAL-TIME BRAKE PAD OVERHEAT DETECTION AND WARNING SYSTEM FOR VEHICLES HAVING DISC BRAKES

H.C.F.Aththachchi*, K.P.Vidanapathirana

Department of Electronics, Wayamba University of Sri Lanka, Kuliyapitiya, Sri Lanka

*hasidu.chamoditha234@gmail.com

ABSTRACT

Disc brakes convert vehicle kinetic energy into heat, and prolonged or severe braking can increase brake temperature sufficiently to contribute to brake fade. This study presents a low-cost, two-module prototype for real-time brake-pad temperature monitoring and driver warning. The system consists of a rechargeable wheel-side sensor module using a K-type thermocouple, MAX31855 converter, and ESP32-S3, and an ESP32-S3-based mini-dashboard that receives temperature and system-status data wirelessly through ESP-NOW. The system classifies the measured temperature as NORMAL below 250 °C, WARNING from 250 °C to below 350 °C, and DANGER at or above 350 °C, while the mini-dashboard provides real-time temperature information together with visual and audible warning indications. A controlled heating experiment was conducted by heating a metal test surface using a hot-air gun, with seven measurement points covering approximately 52-381 °C and therefore spanning all three programmed temperature regions. The developed system recorded values from 52.4 °C to 380.7 °C, while corresponding infrared thermometer measurements ranged from 53.1 °C to 381.8 °C, with a mean absolute difference of approximately 0.89 °C. The infrared thermometer was used only as an independent secondary comparison rather than as a calibrated reference standard. The complete prototype was also evaluated during an approximately 10 km road test under normal driving conditions, during which real-time sensing, wireless transmission, and dashboard operation were successfully demonstrated, with a maximum recorded temperature of approximately 37.5 °C. The results demonstrate the functional feasibility of the developed monitoring and warning prototype; however, further calibration and testing under severe braking, longer driving periods, and wider automotive operating conditions are required before safety-critical implementation.

Keywords: Brake pad overheating, **D**isc brakes, **R**eal-time warning system

1.0 INTRODUCTION

The braking system is a primary safety subsystem in a road vehicle. In a disc brake, friction between the rotating disc and stationary pads converts kinetic energy into thermal energy. During prolonged downhill braking, repeated stop-start operation, emergency braking, or high-load operation, heat can accumulate faster than it is removed by conduction, convection, and radiation. Elevated temperature can change the frictional behaviour of the pad, promote glazing and wear, heat the calliper and brake fluid, and ultimately reduce available braking torque. The loss and subsequent recovery of frictional effectiveness at high and lower temperatures is commonly described as brake fade and recovery [1,2].

Systems such as the anti-lock braking system (ABS) and electronic brake-force distribution (EBD) improve vehicle control by monitoring wheel dynamics and regulating hydraulic pressure. However, they do not normally provide the driver with direct information on brake-pad temperature. Therefore, increasing brake temperature may remain unnoticed until a reduction in braking performance becomes apparent. Real-time temperature monitoring can provide the driver with an earlier indication of increasing thermal conditions, allowing excessive brake heating to be recognized before prolonged braking or driving is continued [3].

Brake-interface temperature is difficult to measure because the contact region is rotating, spatially non-uniform, exposed to debris, and subject to rapid transient heating. Qi and Day showed that sensor location and thermocouple arrangement strongly affect the measured peak temperature and response at the disc-pad interface [2]. Numerical and experimental studies have also shown that factors such

as material properties, operating conditions, vehicle speed, and heat-transfer characteristics influence brake-temperature behavior [4-6]. These findings indicate that a practical monitoring system requires robust high-temperature sensing, real-time processing, and warning thresholds that can later be calibrated for the selected brake-pad material and vehicle.

The objective of this work was to design, construct, and evaluate a compact, low-cost, real-time brake-pad overheat detection and warning prototype. The system was designed as a portable two-module arrangement consisting of a rechargeable wheel-side sensor unit and a separately powered in-vehicle mini-dashboard, with wireless communication eliminating the need for a direct signal cable between the two units. This arrangement was intended to simplify installation on vehicles equipped with disc brakes while providing the driver with continuous temperature information and clear warning indications. The specific objectives were to (i) measure temperature using a K-type thermocouple and MAX31855 converter, (ii) process the measurements using an ESP32-S3, (iii) classify the thermal condition into three warning levels, (iv) wirelessly transfer temperature and system-status data to a dedicated mini-dashboard using ESP-NOW [7], (v) provide real-time visual and audible warning information, and (vi) evaluate the sensing response through controlled heating and an initial vehicle road test.

2.0 METHODOLOGY

2.1 System architecture

The proposed design is divided into a wheel-side sensor module and a separate mini dashboard module. In the sensor module, a K-type thermocouple measures temperature near the brake-pad backing region, while the MAX31855 performs cold-junction compensation and converts the thermocouple signal into digital temperature data [8]. An ESP32-S3 retrieves temperature data through the SPI-compatible interface, checks the sensor condition, applies warning thresholds, and monitors the rechargeable battery level. The processed temperature, warning state, sensor condition, and battery information are transmitted wirelessly to the mini-dashboard using ESP-NOW [7]. The ESP32-S3-based mini-dashboard receives wireless data and updates a 3.5-inch TFT display while controlling the external red danger LED and buzzer. The functional architecture of the developed system is shown in Figure 2.1.

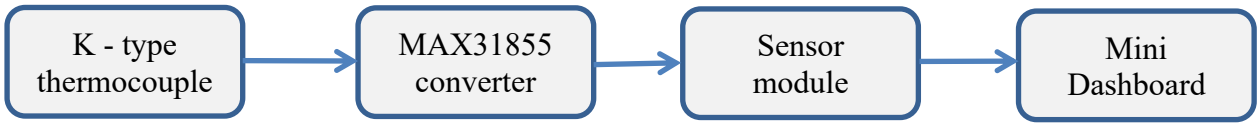


Figure 2.1. Functional block diagram of the developed system

2.2 Hardware implementation

The main hardware components used in the proposed prototype along with their functions are summarized in Table 2.1.

Table 2.1. Main hardware used in the prototype.

Component	Function
K-type thermocouple	Measures temperature near the brake-pad backing region and generates a thermoelectric voltage corresponding to the measured temperature.

Component	Function
MAX31855 module	Provides cold-junction compensation, digitization, and SPI-compatible data transfer in the sensor module ESP32 - S3 [8].
Sensor module-ESP32 - S3	Reads and validates the temperature, monitors the sensor-unit battery level, classifies the temperature condition, and transmits temperature, status, and battery data wirelessly to the mini-dashboard through ESP-NOW [7,9].
Mini-dashboard ESP32 - S3	Receives the wireless data packet through ESP-NOW and controls the TFT display and external status-indicator LEDs.
3.5-inch TFT display (RM68140, 320 × 480)	Displays the real-time brake temperature, NORMAL/WARNING/ DANGER status, wireless connection condition, sensor condition, maximum temperature, and sensor-unit battery percentage.
Power/status LED	Blinks while the mini-dashboard is powered and operating, providing a visual indication that the dashboard controller is active.
Red danger LED	Illuminates when the measured brake temperature reaches or exceeds 350 °C, providing an immediate visual overheat warning.
3.7 V rechargeable Li-ion battery	Provides portable electrical power to the wheel-side sensor module.
USB-C Li-ion charging/protection module	Enables recharging of the sensor-unit Li-ion battery through USB-C and provides battery charging/protection functions.
XL6009 DC-DC boost converter	Boosts the Li-ion battery voltage to a regulated 5 V supply for powering the sensor-module ESP32-S3 and associated electronics.
ON/OFF power switch	Allows the rechargeable sensor unit to be switched on or off without disconnecting the battery and charging circuit.
Protective enclosures and heat-resistant wiring	Protect the modules and the wheel-side sensor connection from heat, vibration, dust, and handling.

2.3 Temperature classification and alert algorithm

The sensor-module program initializes the MAX31855 interface and ESP-NOW communication before entering a continuous sampling loop. Each temperature measurement is checked for sensor faults and compared with the programmed warning thresholds. The temperature, selected warning state, sensor condition, and battery information are then transmitted to the mini-dashboard using ESP-NOW [7]. The mini-dashboard ESP32-S3 updates the 3.5-inch TFT display and controls the external warning outputs.

The implemented decision rule is:

$$State(T) = NORMAL,\ T < 250\ °C;\quad WARNING,\ 250\ °C \leq T < 350\ °C;\quad DANGER,\ T \geq 350\ °C$$

The implemented warning states, corresponding temperature ranges, and mini-dashboard outputs are summarized in Table 2.2.

Table 2.2. Implemented temperature warning logic

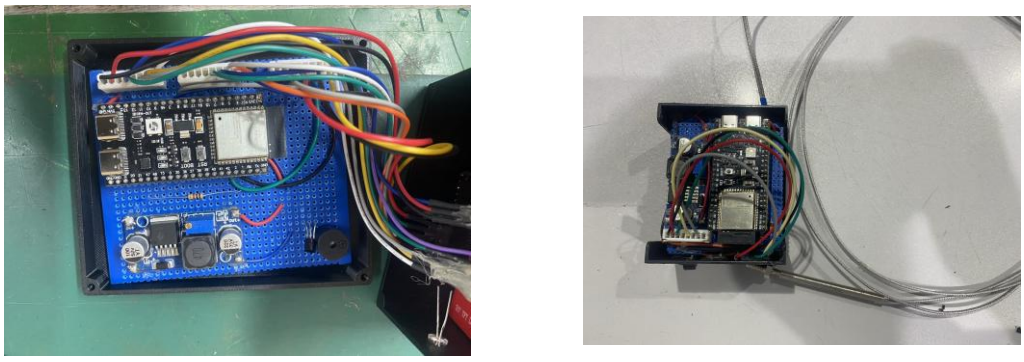
State	**Temperature range**	**TFT mini-dashboard output**	**Warning outputs**
NORMAL	$T < 250$ °C	Live temperature and NORMAL status displayed in green.	Red warning LED OFF; buzzer OFF
WARNING	250 °C $\leq T < 350$ °C	Live temperature and WARNING status displayed in yellow	Red warning LED OFF; buzzer OFF
DANGER	$T \geq 350$ °C	Live temperature and DANGER status displayed in red	Red warning LED ON; buzzer ON

Minor variations were observed during early trials because of airflow and electrical/environmental noise. Consequently, stable wiring, correct thermocouple polarity, secure junction placement, and software averaging are important for repeatable operation. When the converter reports a disconnected or incorrectly wired sensor, the display should present a sensor-fault message rather than classifying an invalid value as a safe temperature.

2.4 Prototype development and test procedure

Prototype development began by installing and verifying the ESP32 development environment, USB-to-UART driver, and MAX31855 software library. The K-type thermocouple was then connected to the MAX31855 module, which was interfaced with the ESP32-S3 in the sensor module. Initial tests using the Arduino Serial Monitor confirmed successful temperature data acquisition. The thermocouple readings at room temperature and under heated conditions were checked using an infrared thermometer as an independent secondary comparison. During this process, incorrect readings caused by reversed thermocouple polarity were identified and corrected.

Following the initial verification of the individual components, the hardware was assembled into two separate prototype units. The wheel-side sensor module integrates the ESP32-S3, MAX31855 thermocouple interface, K-type thermocouple, rechargeable power system, and battery-monitoring circuitry. The mini-dashboard module integrates the ESP32-S3, a 3.5-inch TFT display, warning indicators, a buzzer, and the required power circuitry. The components were mounted on prototype boards and arranged within protective enclosures for subsequent system integration and vehicle testing. The internal hardware arrangements of the two developed modules are shown in Figure 2.2.



(a) (b)

Figure 2.2 Internal hardware assembly of the developed prototype: (a) mini-dashboard module and (b) wheel-side sensor module with K-type thermocouple.

The three-stage temperature classification logic, consisting of NORMAL, WARNING, and DANGER states, was evaluated under controlled conditions by gradually heating a metal surface

using a hot-air gun. The K-type thermocouple was placed in contact with the heated surface, and the corresponding temperature changes and transitions between the three warning states were observed in real time on the mini-dashboard. Measurements were recorded at approximately 50 °C intervals over a temperature range of approximately 52 °C to 381 °C, covering all three programmed temperature regions. An infrared thermometer was used at each measurement point only as an independent secondary comparison. The mini-dashboard, based on an ESP32-S3 and a 3.5-inch TFT display, displays the measured temperature, warning status, wireless communication status, sensor condition, and sensor-unit battery level. ESP-NOW was used to wirelessly transmit the measured temperature and associated system data from the wheel-side sensor module to the mini-dashboard [7]. A red LED and buzzer were also incorporated to provide additional visual and audible indications when the temperature reaches the DANGER level.

In addition to the controlled heating test, the complete system was installed on a vehicle and evaluated over a distance of approximately 10 km under normal driving conditions. The test did not involve prolonged downhill braking, repeated hard braking, or other severe braking conditions intended to produce brake overheating. During the road test, the wheel-side sensor module continuously measured the brake temperature and transmitted the readings to the mini-dashboard inside the vehicle. The highest temperature recorded by the system during the test was approximately 37.5 °C. Following completion of the road test and after the vehicle had stopped, an independent brake-region temperature measurement was obtained using the infrared thermometer as a secondary comparison. Figure 2.3(a) shows the infrared thermometer measurement, while Figure 2.3(b) shows the corresponding temperature received and displayed by the mini-dashboard. The road test was used primarily to evaluate real-time temperature monitoring, wireless data transmission, and overall prototype operation under normal vehicle operating conditions rather than to reproduce a brake-overheating event.

Finally, the two-module arrangement was developed to eliminate the need for a long direct cable between the wheel-side sensor and the dashboard, thereby supporting practical installation in a vehicle.



(a) (b)

Figure 2.3. Temperature comparison following the vehicle road test: (a) brake-region temperature measured using the infrared thermometer and (b) corresponding temperature displayed on the developed mini-dashboard.

3.0 RESULTS AND DISCUSSION

3.1 Functional results

The sensing, communication, display, and warning stages operated successfully during functional testing. The K-type thermocouple and MAX31855 provided real-time temperature measurements to

the wheel-side ESP32-S3 sensor module. During controlled heating, the measured temperature increased in real time, and the programmed three-stage classification logic changed the system status according to the defined thresholds: NORMAL below 250 °C, WARNING from 250 °C to below 350 °C, and DANGER at or above 350 °C. The controlled test reached approximately 381 °C and therefore covered all three programmed temperature regions. The sensor module transmitted the measured temperature, sensor condition, and battery information wirelessly to the ESP32-S3-based mini-dashboard using ESP-NOW. The mini-dashboard displayed the received information on a 3.5-inch TFT display and provided additional warning indications using a red danger LED and buzzer. The rechargeable sensor-unit power system and battery-monitoring function were also integrated into the completed prototype. The overall results of the functional tests are summarized in Table 3.1.

Table 3.1. Summary of prototype test outcomes

Test item	Outcome
Temperature acquisition	Passed
Temperature measurement response	Verified
Three-stage decision logic	Passed
TFT mini-dashboard	Passed
Warning indicators	Passed
Wireless communication	Passed
Rechargeable power & battery monitoring	Passed
Vehicle road test	Verified

3.2 Completed Prototype

Following the integration and functional testing of the individual stages, the complete brake-pad overheat detection and warning prototype was assembled as two separate units: a wheel-side sensor module and an in-vehicle mini-dashboard module. The sensor module incorporates the K-type thermocouple, MAX31855, ESP32-S3, rechargeable Li-ion battery-based power supply, charging circuitry, and battery-monitoring circuit within a protective enclosure. The mini-dashboard incorporates an ESP32-S3, a 3.5-inch TFT display, a red danger LED and a buzzer for additional visual and audible warnings. The two units communicate wirelessly through ESP-NOW, eliminating the need for a long signal cable between the wheel-side temperature sensor and the vehicle cabin. The completed prototype used for functional and vehicle testing is shown in Figure 3.1.



(a) (b) (c)

Figure 3.1 Installation of the completed prototype on the test vehicle: (a) in-vehicle mini-dashboard, (b) wheel-side sensor module, and (c) K-type thermocouple positioned near the brake-pad backing region.

3.3 Measurement interpretation

The performance of the developed temperature-monitoring system was evaluated using both a vehicle road test and a controlled heating experiment. During the road test, the complete prototype was installed on the vehicle and operated over a driving distance of approximately 10 km under normal driving and braking conditions. The test did not involve prolonged downhill braking, repeated hard braking, or other severe braking conditions intended to generate brake overheating. The system continuously monitored the brake temperature during vehicle operation, and the maximum temperature observed on the mini-dashboard was approximately 37.5 °C.

After completion of the road test and once the vehicle had stopped, the mini-dashboard indicated 36.25 °C, while an independent secondary measurement obtained using the infrared thermometer indicated approximately 36.1 °C, giving an absolute difference of approximately 0.15 °C. The corresponding readings are shown in Figure 2.3(a) and Figure 2.3(b). The relatively low maximum temperature observed during the road test can be attributed to the short test distance and normal driving conditions, which did not include prolonged or severe braking. Therefore, the road test primarily demonstrated practical installation, real-time temperature monitoring, wireless data transmission, and dashboard operation under actual vehicle movement rather than brake-overheating performance.

To evaluate the system over a wider temperature range, a controlled heating experiment was conducted by progressively heating a metal surface using a hot-air gun. Seven measurement points were recorded between approximately 52 °C and 381 °C. This range covered all three programmed temperature regions and included measurements above both the 250 °C WARNING threshold and the 350 °C DANGER threshold. At each test point, an infrared thermometer was used only as an independent secondary measurement to provide an indicative consistency check. The recorded values are presented in Table 3.2.

Table 3.2. Comparison of developed system and IR thermometer measurements during controlled heating

Test point	Developed system (°C)	IR thermometer (°C)	Absolute difference (°C)	System state
1	52.4	53.1	0.7	NORMAL
2	101.7	102.4	0.7	NORMAL
3	152.3	153.6	1.3	NORMAL
4	201.6	202.8	1.2	NORMAL
5	250.7	251.2	0.5	WARNING
6	302.4	303.1	0.7	WARNING
7	380.7	381.8	1.1	DANGER

The developed system followed the increasing temperature trend throughout the controlled heating experiment. The absolute differences between the developed system and the infrared thermometer ranged from 0.5 °C to 1.3 °C, with a mean absolute difference of approximately 0.89 °C. The infrared thermometer measurements were used only as an indicative comparison and not as a calibrated reference standard.

The expanded test covered all three programmed warning regions, with measurements below 250 °C classified as NORMAL, measurements of 250.7 °C and 302.4 °C classified as WARNING, and 380.7 °C classified as DANGER. These results demonstrate the operation of the programmed temperature-classification logic; however, further testing under severe vehicle braking conditions is required to evaluate actual brake-overheating performance.

4.0 CONCLUSION

A functional real-time brake-pad overheat detection and warning prototype was developed using a K-type thermocouple, MAX31855, ESP32-S3 controllers, ESP-NOW wireless communication, and a dedicated TFT mini-dashboard. The system provided real-time temperature monitoring and classified the measured temperature into NORMAL, WARNING, and DANGER states. Controlled heating tests conducted over approximately 52-381 °C demonstrated the operation of all three programmed temperature regions, with a mean absolute difference of approximately 0.89 °C between the developed system and the infrared thermometer used as an indicative secondary comparison.

An approximately 10 km road test under normal driving conditions also demonstrated practical temperature monitoring, wireless data transmission, and dashboard operation, with a maximum recorded temperature of approximately 37.5 °C. However, the road test did not reproduce an actual brake-overheating condition. Therefore, further calibration and testing under prolonged and severe braking conditions are required before the system can be considered for safety-critical automotive applications. As a future development, the system can be extended by installing individual temperature-sensing modules at all four wheels, allowing the driver to monitor the thermal condition of each disc brake independently through a single in-vehicle dashboard.

ACKNOWLEDGEMENTS

The authors would like to express their appreciation to the academic and technical staff of the Department of Electronics, Faculty of Applied Sciences, Wayamba University of Sri Lanka, for the facilities and assistance provided during this project.

REFERENCES

1. Blau, P.J., Compositions, Functions, and Testing of Friction Brake Materials and Their Additives. Technical Report ORNL/TM-2001/64, Oak Ridge National Laboratory, Oak Ridge, Tennessee, 2001, doi: 10.2172/788356
2. Qi, H.S. and Day, A.J., Investigation of disc/pad interface temperatures in friction braking. Wear 262, (2007), 505–513, doi: 10.1016/j.wear.2006.08.027
3. Mladenov, G.D., Saliev, D.N. and Abdurahman, H., Integrated brake disc temperature measurement system. *AIP Conference Proceedings* 2449, (2022), 050008, doi: 10.1063/5.0091883.
4. Abebe, L., Nallamothu, R.B., Subrahmanyam, K.H.S., Nallamothu, S.K. and Nallamothu, A.K., Thermal analysis of disc brake made of different materials. *International Journal of Mechanical Engineering* 3, (2016), 5–9, doi: 10.14445/23488360/IJME-V3I6P102.
5. Grkić, A., Mikluc, D., Muždeka, S., Arsenić, Ž. and Duboka, Č., A model for the estimation of brake interface temperature. Strojniški vestnik – Journal of Mechanical Engineering 61, (2015), 392–398, doi: 10.5545/sv-jme.2014.2364.
6. Bellini, C., Di Cocco, V., Iacoviello, D. and Iacoviello, F., Temperature influence on brake pad friction coefficient modelisation. *Materials* 17, (2024), 189, doi: 10.3390/ma17010189.
7. Espressif Systems, *ESP-NOW – ESP32-S3, ESP-IDF Programming Guide*. https://docs.espressif.com/projects/esp-idf/en/stable/esp32s3/api-reference/network/esp_now.html (Accessed 09-08-2026).
8. Analog Devices, *MAX31855 Cold-Junction Compensated Thermocouple-to-Digital Converter Data Sheet*, Rev. 5, 2015. https://www.analog.com/MAX31855/datasheet (Accessed 09-08-2026).
9. Espressif Systems, *ESP32-S3 Series Datasheet*. https://documentation.espressif.com/esp32-s3_datasheet_en.pdf (Accessed 09-08-2026).

Proc. Annual Symposium on Research & Industrial Training, 13 (2026) 47 - 54
Department of Electronics – Wayamba University of Sri Lanka

DESIGN AND IMPLEMENTATION OF A SMART SHOP PROMOTION SYSTEM USING RADIO FREQUENCY IDENTIFICATION AND GEOFENCING TECHNOLOGY

A.A.B.C. Jayawardhana[*1], J.M.J.W. Jayasinghe[1], T.M. Premathilake[2]

[1] *Department of Electronics, Wayamba University of Sri Lanka, Kuliyapitiya, Sri Lanka*
[2]*Techlabs Global private limited, 9B Horton place, Colombo 7, Sri Lanka*

chathushkajayawardhana@gmail.com

ABSTRACT

An intelligent retail environment requires real-time interaction and personalized engagement to attract customers. Traditional promotional methods such as posters and flyers lack real-time responsiveness and context awareness. This paper presents a novel smart shop promotion system that integrates a custom-designed Radio Frequency Identification (RFID) tag antenna with an ESP32 edge controller and Internet of Things (IoT) cloud infrastructure for proximity detection near the shop. The passive Ultra-High Frequency (UHF) RFID tag antenna was designed and simulated, optimizing its geometry for an operating resonance frequency of 867 MHz within the UHF RFID band. A prototype hardware platform comprising a UHF RFID reader and ESP32 edge gateway was realized to capture and relay tag IDs. A React-based mobile application was developed and successfully deployed and tested on an Android device, incorporating user authentication, shop-category preferences, and notification interfaces. The proposed system provides a foundation bridging customized RFID hardware design, embedded edge processing with ESP32, and proximity-based automated marketing.

Keywords: **R**adio Frequency Identification, **E**SP32 Gateway, **G**eofencing,

1.0 INTRODUCTION

In modern retail environments, attracting and engaging nearby potential customers requires real-time interaction and intelligent location-aware systems. Traditional advertising methods such as printed posters, static banners, and paper flyers offer limited reach, lack context awareness, and cannot personalize promotional offers to individual shoppers in real time. To overcome these limitations, technologies such as Radio Frequency Identification (RFID) and Geofencing have emerged as key components of intelligent retail marketing.

RFID enables wireless identification of objects or individuals via electromagnetic fields, while geofencing uses virtual spatial boundaries to trigger location-based actions on mobile devices. When combined, these technologies can transform retail marketing by detecting when a customer is carrying an RFID tag near a shop and immediately delivering targeted promotional notifications to their smartphone [1,2].

Currently, retail businesses face two major challenges in providing effective proximity-based marketing. First, many shops do not have automated mechanisms to detect when customers are near the store, such as in a shopping aisle, corridor, or close to the storefront, and use this information to send promotional notifications in real time [3,4]. As a result, customers may leave the surrounding area without receiving relevant offers. Second, most existing RFID-based systems depend on commercially available RFID tags, which provide limited flexibility for customizing antenna characteristics. This makes it difficult to adjust parameters such as operating frequency

and read range according to the specific requirements and layout of a particular retail environment [5,7].

To address these challenges, this study focuses on two main research questions: how a custom-designed passive UHF RFID tag antenna can be optimized to operate within the 860–960 MHz frequency range while targeting reliable proximity detection over a distance of approximately 10–20 m near retail shops, and how an ESP32-based edge controller and a React-based mobile application can be integrated with cloud-based geofencing to process RFID proximity data and deliver real-time promotional notifications based on customers' selected shop categories.

2.0 EXPERIMENTAL

2.1 Methodology and Flow chart

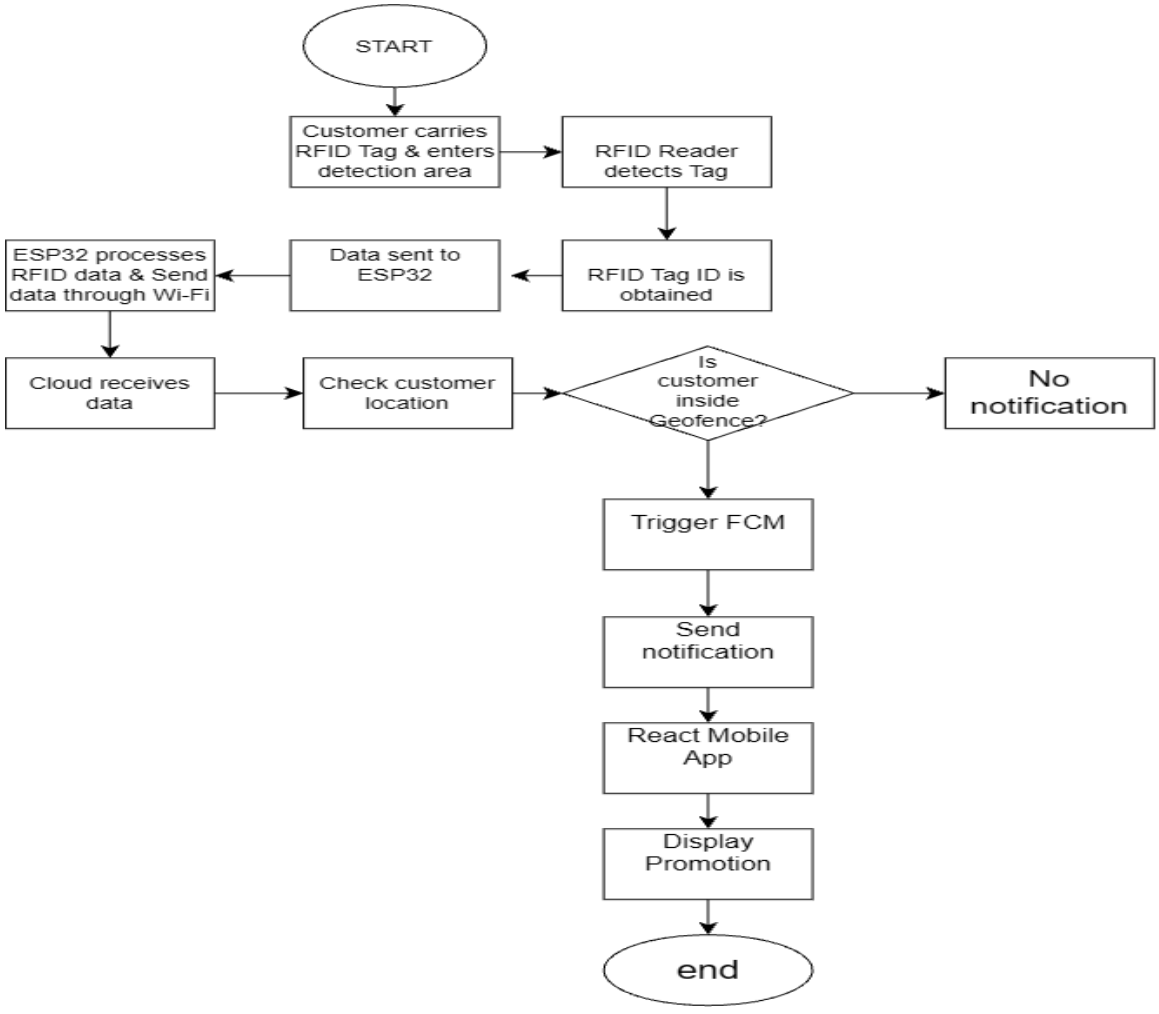


Figure 1: Flow chart of the smart shop promotion system

The system methodology follows an end-to-end IoT workflow designed to detect customer presence in the immediate proximity of a shop and deliver real-time promotional alerts [1]. The overall workflow is illustrated in Figure 1. The architecture consists of five primary layers: the custom-designed passive UHF RFID tag carried by the customer, an entrance/perimeter RFID reader, an ESP32 edge gateway, a cloud backend server, and a client mobile application developed using React. In the present work, antenna design and electromagnetic simulation, hardware

prototype realization (RFID reader + ESP32), and mobile-application development and testing were completed and experimentally evaluated. Full cloud-side geofencing evaluation and end-to-end FCM notification delivery were architecturally defined but remain to be fully experimentally validated in future deployment.

2.2 Custom RFID Tag Design & Antenna Tuning

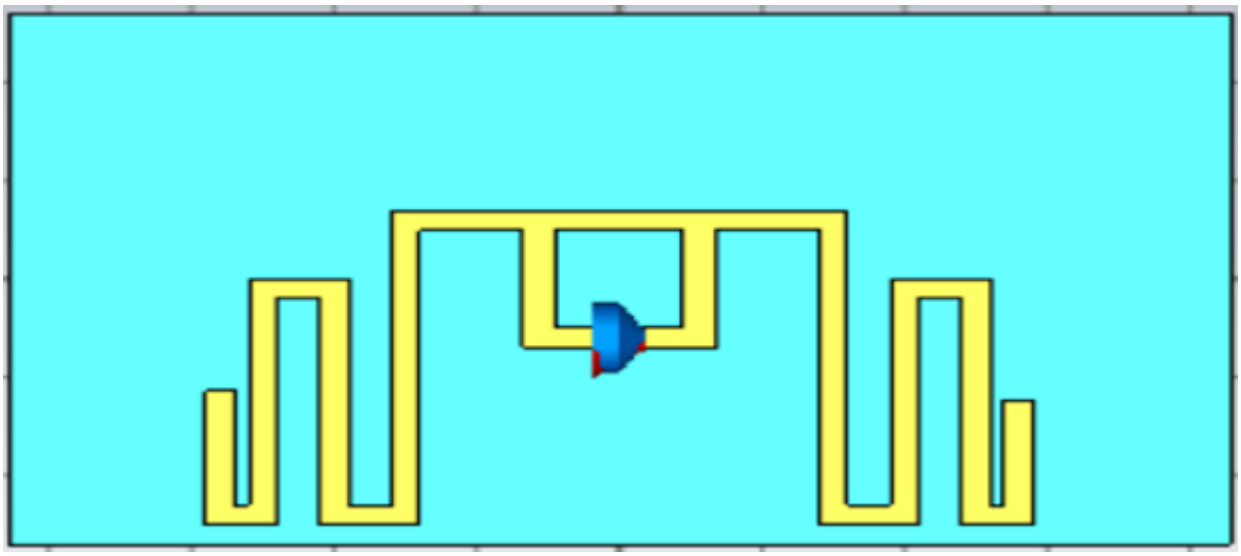


Figure 2: Custom-designed RFID tag antenna structure

A custom-designed RFID tag antenna structure, shown in Figure 2, was modeled and simulated for operation in the UHF RFID frequency band at 867 MHz. Polyethylene Terephthalate (PET) substrate was chosen as the base material due to its flexibility and low dielectric loss, making it suitable for practical customer card integration. Antenna geometric parameters were optimized to achieve reliable RFID detection within the intended proximity area near the shop [4].

2.3 Hardware Realization

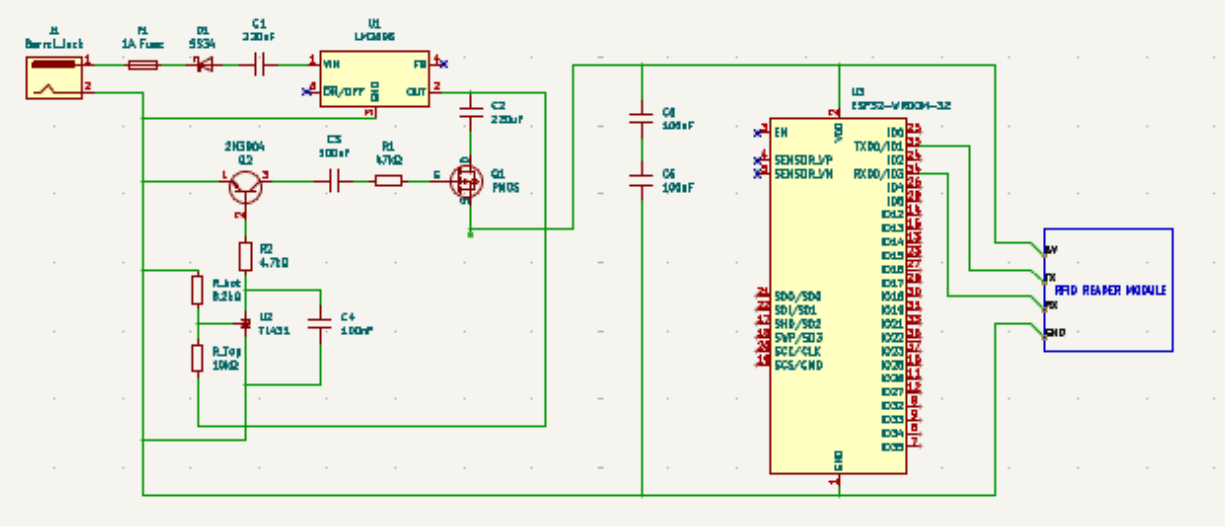


Figure 3: Schematic wiring diagram of the circuit

The prototype implementation shown in Figure 3 consists of a dedicated power supply circuit, an ESP32-WROOM-32 microcontroller, and a UHF RFID reader module. The input DC supply is connected through a fuse and protection diode to the LM2596 buck converter, which provides a regulated supply for the system. Filtering capacitors are included to reduce voltage fluctuations and improve the stability of the power supply. A transistor-based protection and control section is also incorporated into the power circuit to provide additional protection for the connected components.

The regulated supply is connected to the ESP32-WROOM-32, which acts as the main controller of the system. The ESP32 communicates with the UHF RFID reader module through its serial communication interface, allowing the controller to receive RFID tag information. The RFID reader module is powered from the same supply and shares common ground with the ESP32 to ensure reliable communication. Decoupling capacitors are placed near the ESP32 power connections to minimize supply noise and improve stable operation.

The overall wiring provides a compact interface between the power supply, ESP32 controller, and RFID reader module. This design allows the ESP32 to process the RFID data received from the reader and subsequently transmit the required information to the cloud platform through its built-in Wi-Fi connectivity [8,9].

2.4 Mobile Application Development (React Framework)

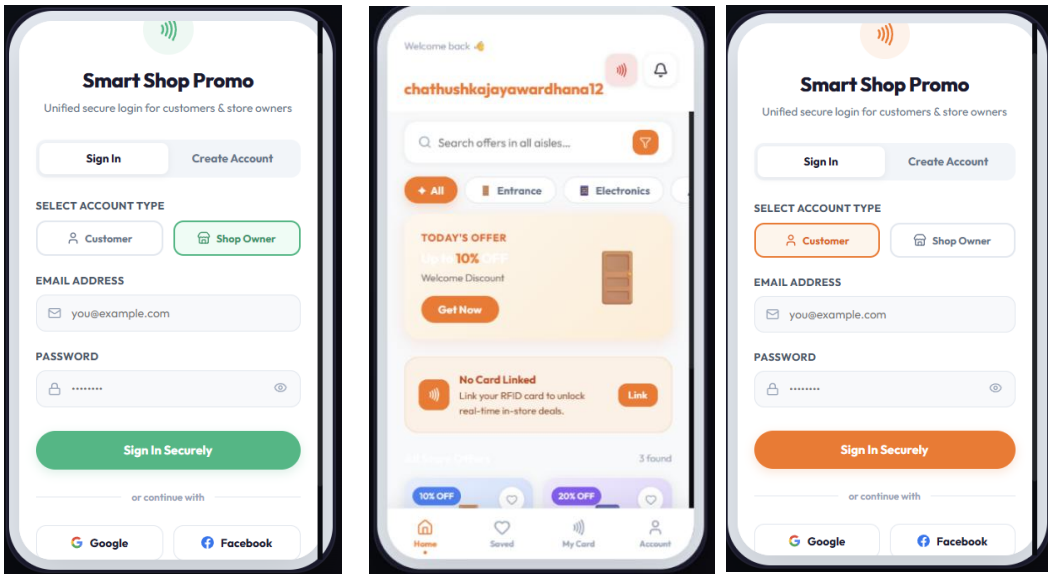


Figure 4: Mobile app interfaces

The cross-platform client mobile application, whose interface screens are shown in Figure 4, was developed to interface shoppers directly with the smart promotion system, providing a seamless user experience for location-aware marketing. Built within Visual Studio Code with configured Android Software Development Kit (SDK) dependencies, the application incorporates secure authentication and core user interface screens, including customer login, registration, and intuitive page navigation. To ensure personalized engagement, the app features interactive notification preferences and category filtering, allowing users to select specific shop types such as clothing, electronics, or groceries and receive tailored promotional alerts based on their preferences [4].

The operational stability and cross-device performance of the application were thoroughly evaluated through hands-on testing on a physical Android mobile device. During the build setup, Gradle configurations and framework dependencies were debugged and verified to support real-time data handling [2, 8].

3.0 RESULTS AND DISCUSSION

3.1RFID Antenna simulation analysis

The proposed RFID tag antenna was simulated using CST Studio Suite to evaluate its electromagnetic performance. The simulation results show that the antenna achieves resonance at approximately 867 MHz, which falls within the UHF RFID operating frequency range of 860–960 MHz. The S_{11} response confirms that the antenna is appropriately tuned to the target operating frequency, indicating suitable impedance matching for RFID tag operation. The simulated antenna characteristics provide the basis for evaluating its radiation performance and theoretical read range in the following sections.

3.2 S_{11}characteristics

The CST Studio Suite electromagnetic simulation confirmed the resonance behavior for the custom-designed RFID tag antenna. As shown in the S11 plot in Figure 5, the tag antenna demonstrated sharp resonance at approximately 867 MHz, aligning with standard UHF RFID band allocations.

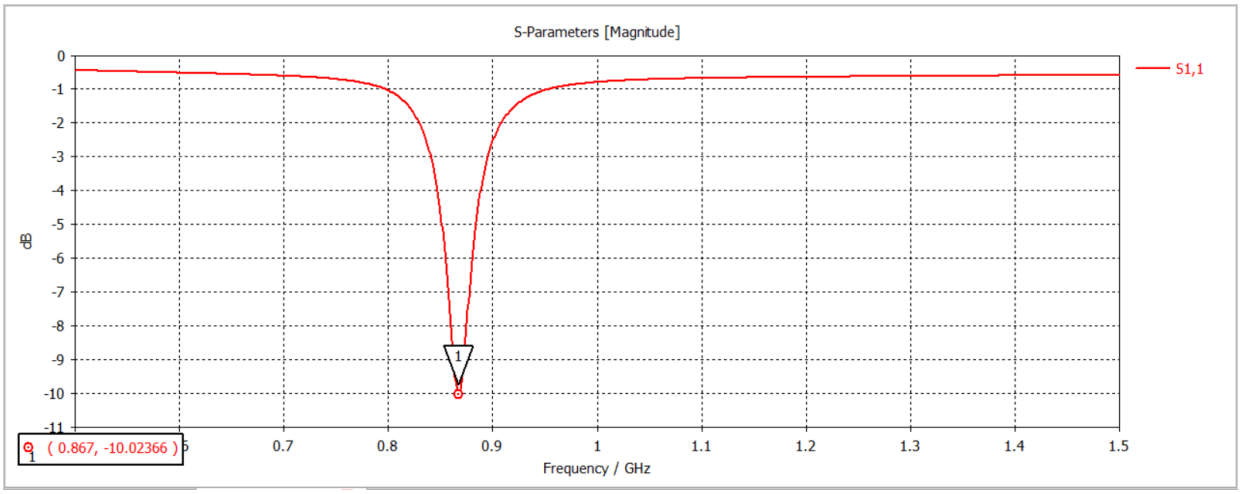


Figure 5: Custom-designed RFID tag S_{11} graph

3.3 3D Radiation pattern

The simulated 3D far-field radiation pattern at 0.8665 GHz, presented in Figure 6, illustrates the three-dimensional distribution of the antenna's radiated electromagnetic energy. The radiation pattern shows a broad radiation region, with the strongest radiation concentrated in the direction indicated by the red and orange regions. The maximum simulated radiation level is approximately 1.9 dBi, as indicated by the color scale. For subsequent theoretical range estimation, a realized tag antenna gain of 1.9 dBi is adopted to maintain consistency with the simulated radiation performance. The radiation gradually decreases from the maximum region toward the regions with lower radiation levels, which represent weaker radiation. This broad radiation pattern indicates

that the proposed RFID tag antenna can provide sufficient coverage for detecting an RFID reader from different directions, which is suitable for customer proximity detection near a shop entrance.

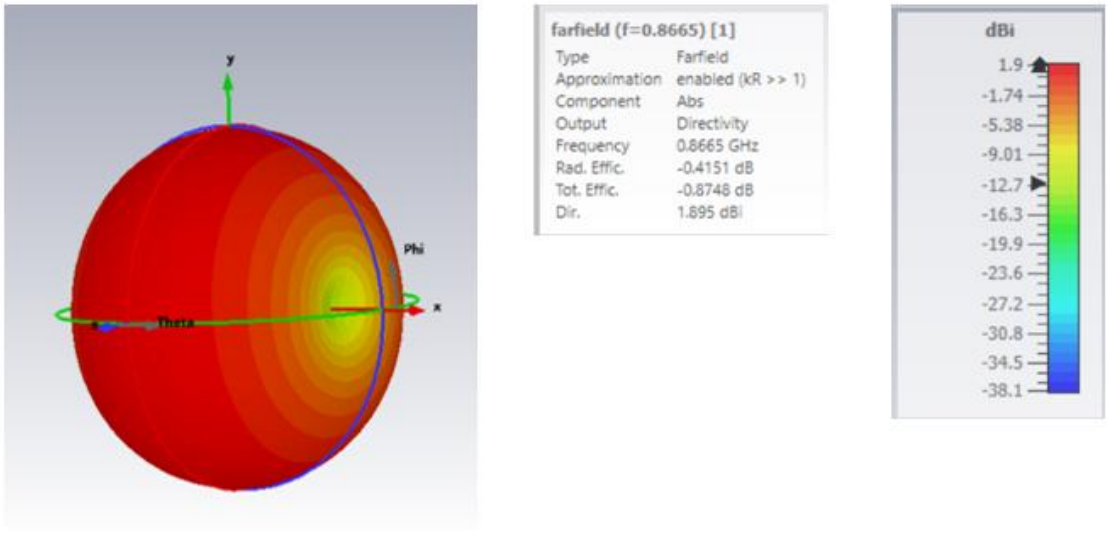


Figure 6: 3D far field radiation plot

3.4 Theoretical read-range estimation

The theoretical maximum detection distance of the passive UHF RFID tag is derived using the Friis transmission equation;

$$P_r = P_t \frac{G_t G_r \lambda^2}{(4\pi R)^2} \quad [3.1]$$

Where;
P_r = Received power
P_t = Transmitted power
G_t = Transmitter antenna gain
Gr = Receiver antenna gain
λ = Wavelength
R = Separation distance

The product of the transmitting power and the transmitting antenna gain represents the Equivalent Isotropically Radiated Power (EIRP).

$$EIRP = P_t . G_t \quad [3.2]$$

By substituting EIRP and considering the tag chip sensitivity threshold P_{chip} as the minimum required received power (P_r), the maximum read range can be rearranged as [5,6];

$$R_{range} = \left(\frac{\lambda}{4\pi}\right)\sqrt{\frac{G_{tag} \cdot EIRP}{P_{chip}}} \quad [3.3]$$

Where;
G_{tag} = Realized gain of the tag antenna.
R_{range} = Maximum read range

P_{chip} = Minimum required received power

For the operating frequency of 867 MHz;

$$\lambda = 0.346 \text{ m}$$

Substituting an operating frequency of 867 MHz and an EIRP of 3.2 W, a tag antenna gain Gtag of 1.9 dBi, and a tag chip sensitivity Pchip of 0.0000158 W yields for equation (3.3);

$$R_{range} = \left(\frac{0.346}{4\pi}\right)\sqrt{\frac{1.9\times3.2}{0.0000158}} \approx 17.07\ m$$

Based on the selected system parameters, the calculated theoretical free-space range was approximately 17.07 m. However, this value represents an ideal free-space condition and should not be considered the actual operating range of the system. Practical RFID performance is expected to be lower due to antenna orientation, multipath reflections, absorption by surrounding objects, tag detuning, and environmental conditions. Consequently, while the simulation and theoretical analysis support the feasibility of proximity detection on the order of 10–20 m under favorable conditions, experimental validation of the realized read range and of the complete notification workflow was outside the scope of the present study and is reserved for future work.

4.0 CONCLUSION

This study designed a smart shop promotion system that integrates a custom-designed passive UHF RFID tag antenna, an ESP32 edge gateway, and a React mobile application for proximity marketing near shops. Simulation analysis verified that the custom-designed tag antenna resonates at 867 MHz within the UHF RFID band, while Friis transmission equation calculations demonstrated an ideal theoretical free-space read range of approximately 17.07 m. In practical deployment, the effective detection distance is expected to decrease due to real-world factors such as environmental propagation losses, multipath reflections, and antenna misalignment. A hardware prototype comprising the ESP32 controller and UHF RFID reader was realized, and the React mobile application providing user login, registration, and shop-category notification preferences was successfully tested on an Android device. Full experimental validation of the realized read range, cloud-side geofencing logic, and end-to-end Firebase Cloud Messaging (FCM) notification delivery remains future work, together with physical tag fabrication on PET substrates and Bluetooth Low Energy (BLE) fallback mechanisms for offline store environments.

ACKNOWLEDGEMENTS

The authors would like to acknowledge all the staff of the Department of Electronics, Faculty of Applied Sciences, Wayamba University of Sri Lanka, and all others who supported the successful completion of this research.

REFERENCES

1. Al-Kassab, J., Thiesse, F., Buckel, T., *Journal of Theoretical and Applied Electronic Commerce Research*, 2013, 8, 112–137.
2. Rejeb, A., Keogh, J. G., Treiblmaier, H., *Location-Based Services and Smart Retail Ecosystems*, Springer, 2021.
3. Paulose, A., Aswathy, A. K. S., Nurjahan, N. V. A., *International Journal of Engineering*

Research & Technology (IJERT), 2019, 8, 6, Art. no. IJERTV8IS060233.
4. Rao, K. V. S., Nikitin, P. V., Lam, S. F., *IEEE Transactions on Antennas and Propagation*, 2005, 53, 3870–3876.
5. Tanim, M. M. Z., *Comparison of performance and stability of different wearable passive UHF RFID tags in body-worn configuration*, Tampere University of Technology, 2017.
6. EPCglobal, *EPC Radio-Frequency Identity Protocols Class-1 Generation-2 UHF RFID Protocol for Communications at 860 MHz–960 MHz*, Version 2.0.1, 2015.
7. Yao, Y., Ge, Q., Yu, J., Chen, X., *Electronics*, 2021, 10, 11, Art. no. 1310.
8. Google Developers, *Firebase Cloud Messaging HTTP v1 API and ESP32 Integration Guide*, Firebase Documentation, Google LLC, 2024. https://firebase.google.com/docs/cloud-messaging
9. Espressif Systems, *ESP32 Wi-Fi and HTTP Client Library for Firebase Real time Connection*, Espressif Documentation, 2023. https://docs.espressif.com/projects/esp-idf/en/latest/esp32/api reference/protocols/esp_http_client.html

Proc. Annual Symposium on Research & Industrial Training, 13 (2026) 55 - 62
Department of Electronics – Wayamba University of Sri Lanka

DEVELOPMENT OF A LOW-COST FABRIC DYE POWDER MIXING PROTOTYPE WITH GRAVIMETRIC DISPENSING AND COLOUR SENSING

H.P.D.P.C. Madhusanka*, P.G.T.R. Payagala

Department of Electronics, Wayamba University of Sri Lanka, Kuliyapitiya, Sri Lanka

*pathummadhusanka281@gmail.com

ABSTRACT

Fabric dye powder preparation in small-scale industries often depends on manual colour identification, recipe selection, and weighing, which can increase preparation time and produce inconsistencies between batches. This study developed a low-cost prototype integrating controlled fabric colour sensing with gravimetric three-channel powder dispensing. The system used an ESP32 microcontroller, a TCS34725 colour sensor, three auger-based dispensers, a common 5 kg load cell with an HX711 interface, local and web-based user interfaces, and a servo-operated batch-release mechanism. Flour was used as the representative powder during experimental testing. The main contribution was an automatic gravimetric calibration and closed-loop dispensing method that determined the relationship between auger movement and delivered powder mass. The final three calibration runs comprised nine stages and produced a pooled calibration coefficient of 1.10340×10^{-4} g/step, a median stage coefficient of 1.10463×10^{-4} g/step, and an overall relative standard deviation of 1.210%. The average powder delivery rate was approximately 5.56 g/min. In the colour-sensing subsystem, black and white reference measurements were used to normalize each RGB channel to a range of 0–255. A grey sample produced normalized RGB values of approximately (128, 125, 124) and was identified as grey/neutral. Preliminary target-mass validation produced external-scale measurements of 30 g for a 30 g target and 49 g for a 50 g target, corresponding to absolute percentage errors of 0% and 2.00%, respectively. A complete three-channel batch targeting 10 g from each dispenser produced an external final mass of 29 g for a 30 g target, giving an absolute percentage error of 3.33%. The results demonstrate the feasibility of integrating low-cost colour sensing with automatically calibrated gravimetric powder dispensing. However, repeated testing with actual dye powders and the development of a validated colour-to-recipe model are required before industrial application.

Keywords: Fabric dye, **C**olour identification, **P**owder dispensing

1.0 INTRODUCTION

In many local dye-related small-scale operations, powder mixing is still carried out manually. Workers often depend on practical experience and colour matching by trial and error to obtain a suitable shade. Although this method may work for experienced operators, it can reduce repeatability, increase preparation time and cause difficulty when the same colour has to be prepared again. These practical limitations motivated the selection of the present research problem.

The long-term aim of this project is to create an automated fabric dye powder mixing system that can identify the colour of a fabric sample and prepare a corresponding powder mixture automatically. Automatic medicine and laboratory powder-handling systems have demonstrated that motor-controlled dispensing can reduce manual handling and support repeatable preparation [1,2]. In the proposed system, a colour sensor measures the sample under controlled conditions, the controller determines the required powder quantities, three powder

dispensers deliver the powders into a common container, and the dispensed powders are mixed automatically. Among these subsystems, powder dispensing is the most critical element because an error in a single component directly affects the final mixture.

The performance of a screw feeder depends on the powder properties, screw speed, hopper fill condition and feeder geometry [3-5]. These effects are especially important for cohesive powders because bridging or an irregular supply to the auger can interrupt the flow. Closed-loop gravimetric feedback has therefore been applied to powder-supply processes to improve control and respond to disturbances [6,7]. However, many reported systems use specialised or industrial equipment that may be costly or difficult to adapt to a small prototype. Therefore, this work focuses on developing a low-cost undergraduate-level prototype that can still demonstrate meaningful automation features, including automatic calibration, startup checking, no-flow recovery and target-mass dispensing.

The main objective of this study is to develop and evaluate the gravimetric auger dispensing subsystem while maintaining the full system context of automatic dye-powder preparation. The research question is whether the developed controller can obtain a repeatable mass-per-step calibration and use it for preliminary target-mass dispensing.

2.0 EXPERIMENTAL

2.1 Overall System Architecture

The complete system consists of a sample colour identification section, embedded controller, three powder dispensers, common weighing platform, and user interface. The simplified complete-system block diagram is shown in Figure 2.1. A TCS34725 colour sensor was used inside a closed chamber with an approximately 5 mm measurement distance. Black and white references were used for sensor calibration. The ESP32 acted as the central controller and hosted a web interface while also driving the local liquid-crystal display. Although the final system is intended to convert sample colour information into powder quantities, the present experiments used direct target entry so that the dispensing subsystem could be studied independently.

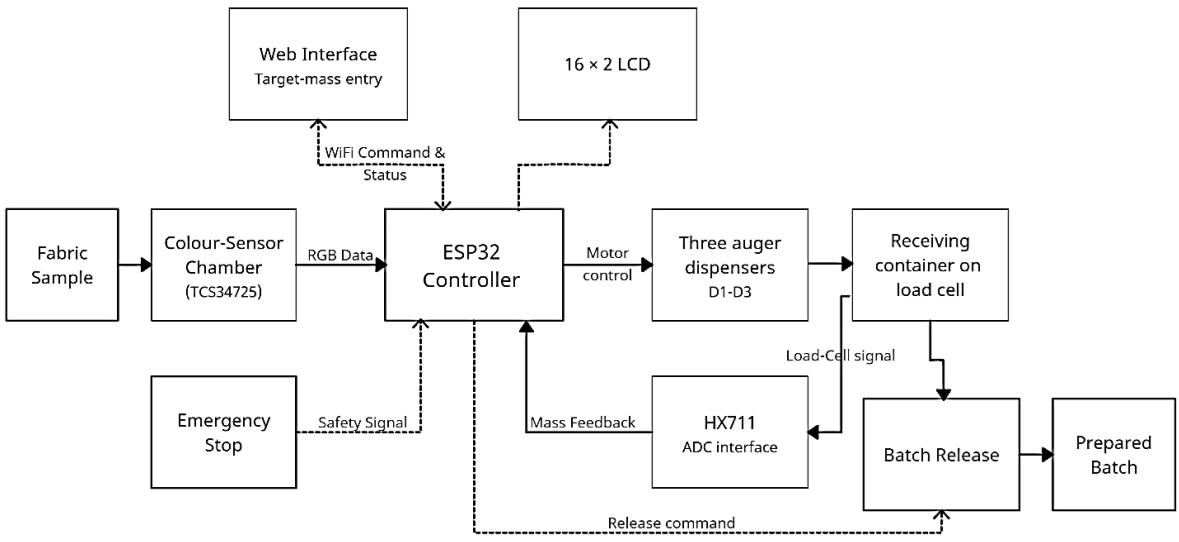


Figure 2.1 Simplified block diagram of the complete fabric dye powder mixing system

2.2 Gravimetric dispenser prototype

Each dispensing channel used a horizontal auger driven by a 28BYJ-48 geared stepper motor through a flexible coupling. The auger had an outside diameter of 17.05 mm, a length of 50.8 mm, and a pitch of 6.0 ± 0.5 mm. It was installed inside a tube with an internal diameter of 19.05 mm, providing a radial clearance of approximately 1.00 mm. The free end of the auger was mechanically supported to maintain its alignment within the tube. The mechanical arrangement of the dispenser is shown in Figure 2.2.

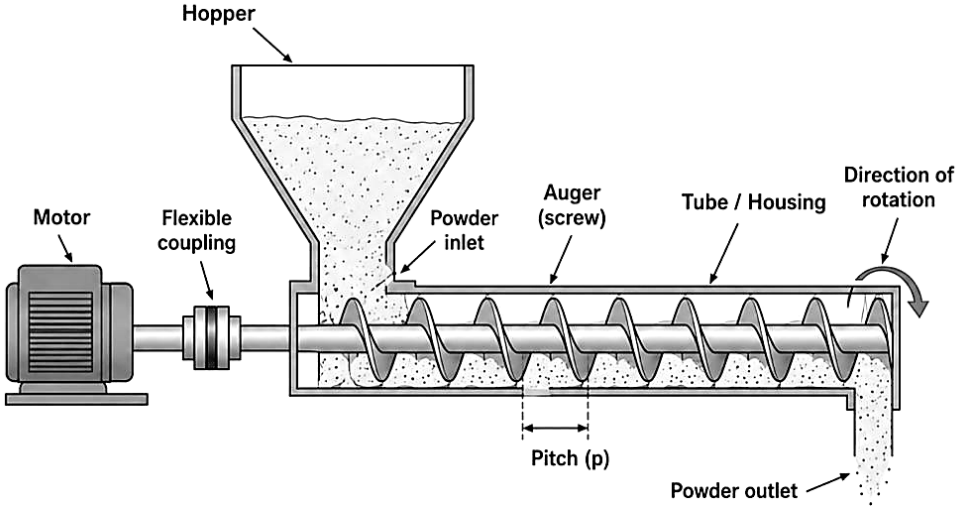


Figure 2.2 Mechanical arrangement of the gravimetric auger dispenser

Three dispensers discharged powder sequentially into a common receiving container mounted on a 5 kg load cell. Flour was used as a representative powder during preliminary experiments. Because feeder output can vary with material properties, auger filling, hopper condition, and operating parameters, an individual calibration coefficient was determined for each dispensing channel [3–5]. The principal hardware components used in the developed prototype are summarized in Table 2.1.

Table 2.1 Main hardware components used in the prototype

Component	Specification	Purpose
Controller	ESP32 DevKit	Main control, interface and logging
Motor and driver	28BYJ-48 + ULN2003	Auger rotation
Weighing system	5 kg load cell + HX711	Mass feedback
Colour sensor	TCS34725	Sample colour measurement
Display	I²C LCD	Local status display
Test material	Flour	Prototype powder

2.3 Control method and calibration procedure

The controller firmware was implemented as a state machine. Its main operating sequence is shown in Figure 2.3. Before calibration or dispensing began, the controller verified that the receiving container was correctly positioned and that the load-cell reading was stable. The container was then tared.

Each auger underwent a priming stage before controlled dispensing. Priming continued until a powder mass increase of approximately 2 g was detected, confirming that powder had reached

the outlet. The load cell was subsequently re tared. If sufficient motor movement occurred without the expected increase in mass, the controller performed a reverse-and-retry recovery operation. This continuous use of load-cell feedback follows the general closed-loop approach reported for automated powder dispensing [6, 7].

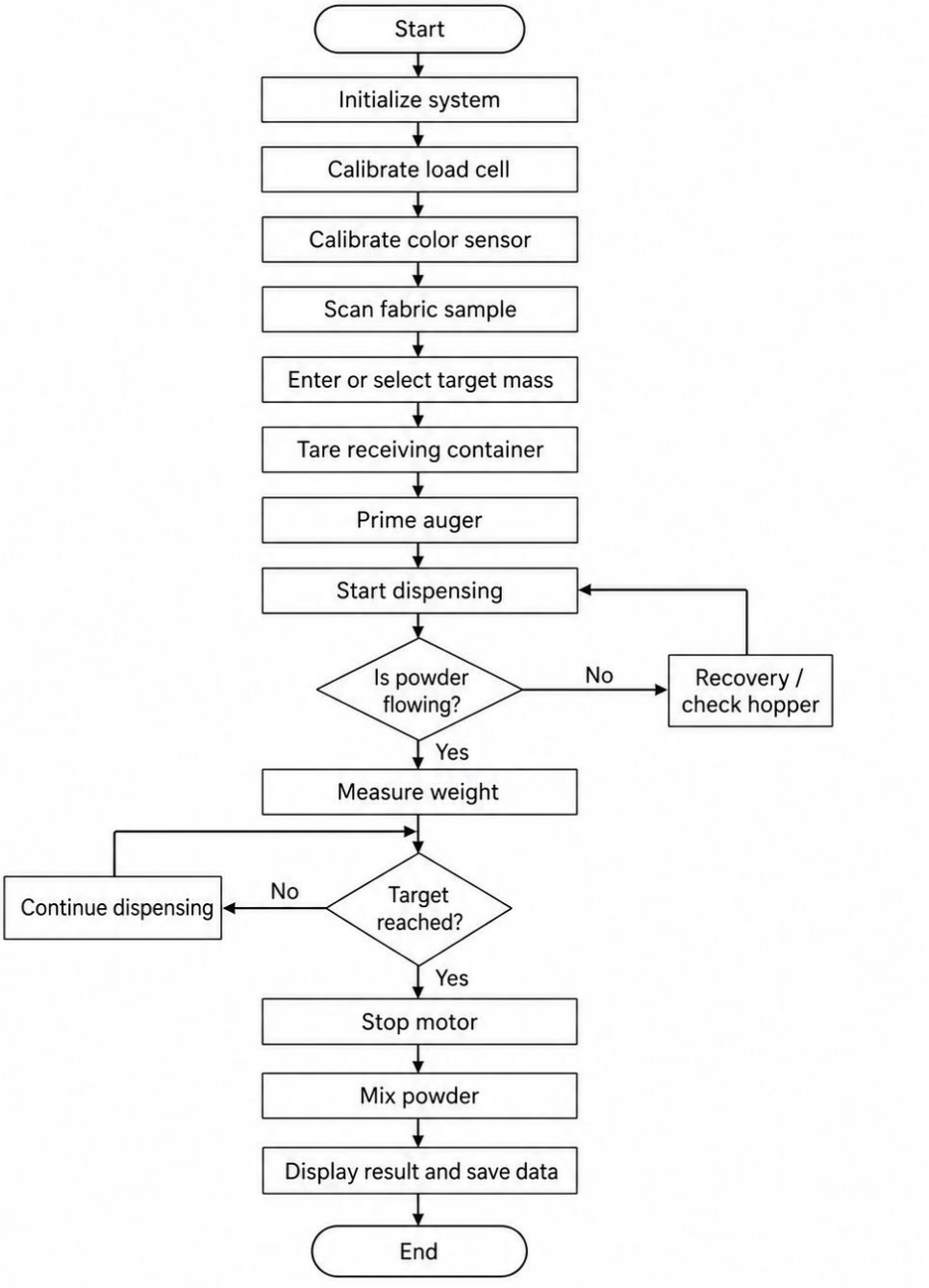


Figure 2.3 Simplified flowchart of the system calibration and dispensing process

Automatic calibration was then carried out using three consecutive nominal 30 g dispensing stages. For each stage, the system recorded the motor step count, stable mass increment and motor time. The calibration coefficient was calculated using $k = \Delta m/N$, where Δm is the mass increment and N is the motor step count. Three complete calibration runs were conducted, producing nine stage coefficients. Each dispensing channel retained its own calibration coefficient because mechanically similar feeders can produce different powder outputs.

2.4 Colour Detection and Target-Weight Assignment

The colour sensor was mounted in the closed chamber approximately 5 mm above the fabric sample. Black and white reference measurements defined the lower and upper response of each red, green and blue channel. A sample value C was normalized as $C_N = (C_S - C_B)/(C_W - C_B) \times 255$, where C_S is the sample reading and C_B and C_W are the black and white references. The normalized RGB values were used by the firmware to identify broad colour categories.

In the present prototype, RGB values were not converted directly to powder mass by a validated mathematical model. Such a conversion requires an experimentally verified colour-to-recipe database or prediction method. Instead, the identified colour provides the sample information, while the three target masses are entered or verified through the web interface. A future recipe database or prediction model can provide these target masses automatically without changing the gravimetric dispensing architecture.

2.5 Target-Mass Validation

Following automatic calibration, preliminary target-mass tests were conducted at 30 g and 50 g. A bulk-and-fine dispensing strategy was used. The bulk stage delivered most of the required powder at a higher operating rate, while the fine stage operated more slowly near the target to reduce overshoot. Previous feeder studies have shown that calibration and operating conditions should be selected according to the powder properties, feeder configuration, and required dose [4, 5]. After the motor stopped, the controller waited for the load-cell reading to stabilize before accepting the final value.

For each trial, the target mass, final load-cell measurement, independent external-scale measurement, total process time, and number of recovery attempts were recorded. The absolute percentage error (APE) was calculated as $APE = |m_{ext} - m_t|/m_t \times 100\%$, where m_t is the target mass and m_{ext} is the independent external-scale mass. While the initial validation was limited to two distinct mass targets (30 g and 50 g) to establish baseline system viability, this limited trial size ($n = 2$) is recognized as a constraint of the preliminary study.

3.0 RESULTS AND DISCUSSION

3.1 Colour Identification Results

The colour-sensing results obtained under the controlled chamber conditions are presented in Table 3.1. The black and white reference measurements established the lower and upper limits for the two-point normalization of each RGB channel. Consequently, the black reference was mapped to (0, 0, 0), while the white reference was mapped to (255, 255, 255). The grey sample produced normalized RGB values of (128, 125, 124).

The grey sample values were near the midpoint of the normalized range, and the small differences among the red, green, and blue channels indicated a balanced neutral response. The sample was therefore identified as GREY/NEUTRAL. These results demonstrate the functional operation of reference-based normalization and broad colour-category identification. However, only a limited number of samples were tested, and the results do not constitute a validated assessment of industrial colour-matching accuracy.

Table 3.1 Colour-sensor calibration and identification results

Condition	Raw R	Raw G	Raw B	Clear	Normalized RGB	Identified colour
Black reference	73	47	34	149	(0, 0, 0)	Black / Very Dark
Grey sample	1048	760	524	2252	(128, 125, 124)	Grey / Neutral
White reference	2015	1497	1042	4493	(255, 255, 255)	White / Very Light

3.2 Calibration performance

Table 3.2 summarises the three completed automatic calibration runs. The individual run means were 1.09947×10^{-4}, 1.10359×10^{-4} and 1.10737×10^{-4} g/step, with run-level relative standard deviations of 0.726%, 1.058% and 1.950%, respectively. The consistency across individual stages within these runs is plotted in Figure 3.1. These results indicate good repeatability during calibration.

Table 3.2 Summary of the three completed 30 g calibration runs.

Run	Total mass (g)	Mean coefficient (g/step)	Median coefficient (g/step)	RSD (%)
1	90	1.09947×10^{-4}	1.09889×10^{-4}	0.726
2	90	1.10359×10^{-4}	1.40463×10^{-4}	1.058
3	89	1.10737×10^{-4}	1.10680×10^{-4}	1.950

When the nine calibration stages were pooled together, the overall coefficient based on total mass and total steps was 1.1034×10^{-4} g/step. The median of the nine stage coefficients was 1.10463×10^{-4} g/step, and the overall stage-based relative standard deviation was 1.210%. Figure 3.2 shows the linear relationship between cumulative dispensed mass and cumulative motor steps across the pooled dataset. The average dispensing rate across the calibration stages was approximately 5.56 g/min. The effective motor rate derived from motor time was $8.397 \times 10^{2} \pm 5.0$ steps/s, which is lower than the selected command speed of 1.4×10^{3} steps/s. This indicates that the practical execution speed of the system was limited by the control loop and other simultaneous tasks.

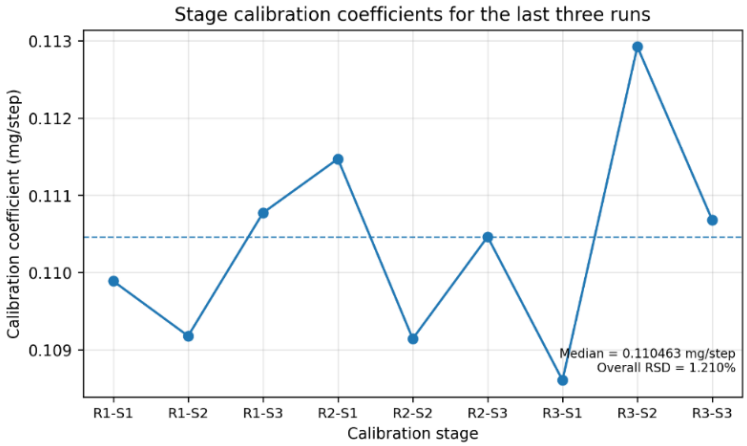


Figure 3.1 Stage calibration coefficients obtained from the three completed runs.

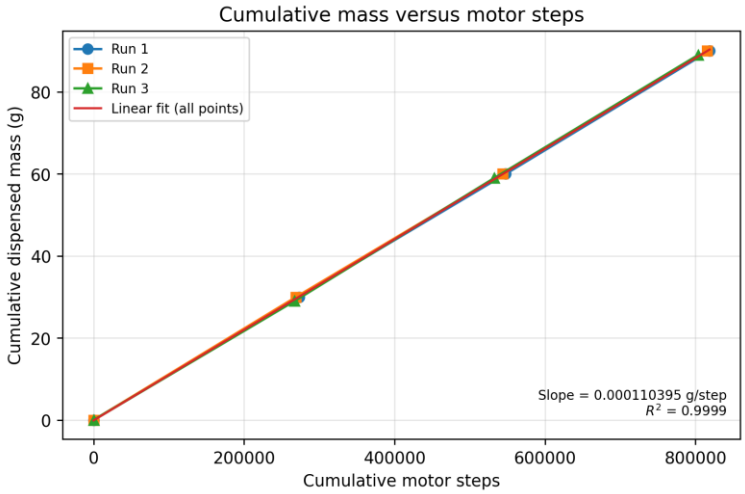


Figure 3.2 Relationship between cumulative dispensed mass and cumulative motor steps

3.3 Preliminary target-mass validation

Table 3.3 Preliminary target-mass validation results available at the time of drafting

Trial	Target (g)	Load-cell final (g)	External final (g)	External error (g)	APE (%)	Process time (s)	Recovery
1	30	30	30	0	0.00	634.067	1
2	50	50	49	-1	2.00	1037.200	0

Table 3.3 shows the 30 g validation trial produced a final load-cell value of 30 g and an external-scale value of 30 g, giving zero recorded external error within the available measurement resolution. One recovery attempt occurred during the trial, after which the system still reached the target. The 50 g validation trial produced a final load-cell value of 50 g, while the external scale indicated 49 g. This corresponds to an external absolute percentage error of 2.00%. No recovery action was needed in that trial.

3.4 Practical observations

A final integrated batch tested all three dispensers sequentially using individual calibration coefficients. The target was 10 g from each channel (30 g total). The internal increments were 9 g, 10 g and 9 g, giving 28 g on the common load cell, while the independent external scale indicated 29 g. The external batch APE was therefore 3.33%. No recovery was required during the three-channel batch. The different channel coefficients also confirmed the value of calibrating each dispenser independently.

Two practical powder-handling issues were observed during development. First, an initially empty auger required priming before a stable discharge condition was obtained. Second, bridging could occur above the hopper outlet and reduce material supply to the auger, consistent with reported screw-feeding behaviour for difficult powders. Cohesive materials, such as the flour used in testing and actual reactive dye powders, tend to form stable mechanical arches over the dispensing outlet. This occurs due to high inter-particle friction and potential moisture-induced agglomeration, which disrupts the uniform volumetric feed density required for consistent auger output [3-5]. These observations support the inclusion of priming, no-flow

detection and reverse-and-retry recovery. The weighing system was effectively reliable to about 1 g, so the present results should not be interpreted as evidence of sub-gram accuracy.

4.0 CONCLUSION

This study developed and evaluated a low-cost fabric dye powder preparation prototype integrating colour sensing with gravimetric three-channel dispensing. The automatic calibration method produced a pooled coefficient of 1.10340×10^{-4} g/step and an overall RSD of 1.210% across nine calibration stages. External-scale measurements were 30 g for a 30 g target and 49 g for a 50 g target, corresponding to APE values of 0% and 2.00%. A three-channel batch targeting 30 g produced 29 g, giving an APE of 3.33%. Black-and-white reference normalization also identified a grey sample from RGB values of (128, 125, 124). These results confirm the feasibility of combining low-cost colour sensing with feedback-controlled powder dispensing. However, the use of flour, limited validation trials, approximately 1 g weighing resolution, low dispensing speed, and the absence of a validated colour-to-recipe model restrict industrial application. Further testing should use dye powders and improved hardware.

ACKNOWLEDGEMENTS

The authors gratefully acknowledge the guidance and support provided by the Department of Electronics, Wayamba University of Sri Lanka.

REFERENCES

1. Lin, J. Y., Lin, J. M., Han, C. C., Wu, Y. C., and Chang, C. S., "An Automatic Chinese Medicine Dispensing Machine Using Shelf-Based Mechanism," *Applied Sciences*, 2019, vol. 9, pp. 5060, doi: 10.3390/app9235060.
2. Fermier, A. M., Troisi, J., Heritage, E. C., Drexel, M. A., Gallea, P., and Swinney, K. A., "Powder dispensing robot for sample preparation," *The Analyst*, 2003, vol. 128, pp. 790, doi: 10.1039/b300274h.
3. Imole, O. I., Krijgsman, D., Weinhart, T., Magnanimo, V., Chávez Montes, B. E., Ramaioli, M., and Luding, S., "Experiments and discrete element simulation of the dosing of cohesive powders in a simplified geometry," *Powder Technology*, 2016, vol. 287, pp. 108-120, doi: 10.1016/j.powtec.2015.07.051.
4. Fathollahi, S., Sacher, S., Escotet-Espinoza, M. S., DiNunzio, J., and Khinast, J. G., "Performance Evaluation of a High-Precision Low-Dose Powder Feeder," *AAPS PharmSciTech*, 2020, vol. 21, p. 301, doi: 10.1208/s12249-020-01835-5.
5. Li, T., Scicolone, J. V., Sanchez, E., and Muzzio, F. J., "Identifying a Loss-in-Weight Feeder Design Space Based on Performance and Material Properties," *Journal of Pharmaceutical Innovation*, 2019, vol. 15, pp. 482-495, doi: 10.1007/s12247-019-09394-4.
6. Breese, P. P., Hauser, T., Regulin, D., Seebauer, S., and Rupprecht, C., "In situ measurement and closed-loop control for powder supply processes," *The International Journal of Advanced Manufacturing Technology*, 2021, vol. 116, pp. 889-903, doi: 10.1007/s00170-021-07438-z.
7. Sahay, A., Brown, M., Muzzio, F., and Takhistov, P., "Automated Drop-on-Demand System with Real-Time Gravimetric Control for Precise Dosage Formulation," *SLAS Technology*, 2013, vol. 18, pp. 152-160, doi: 10.1177/2211068211433398.

Proc. Annual Symposium on Research & Industrial Training, 13 (2026) 63 - 70
Department of Electronics – Wayamba University of Sri Lanka

DEVELOPMENT OF A MACHINE LEARNING-BASED NON-INVASIVE BLOOD GLUCOSE ESTIMATION SYSTEM

I. D. S. T. Madhushankha*, P. G. T. R. Payagala

Department of Electronics, Wayamba University of Sri Lanka, Kuliyapitiya, Sri Lanka

*stharaka403@gmail.com

ABSTRACT

Diabetes mellitus requires frequent blood glucose monitoring, while conventional finger-prick methods can cause discomfort and reduce patient compliance. This study develops a machine learning-based non-invasive blood glucose estimation system using physiological parameters including Electrocardiogram (ECG), Blood Oxygen Saturation (SpO_2), body temperature, and Galvanic Skin Response (GSR). A dataset containing 10,000 samples was preprocessed and used to evaluate multiple machine learning algorithms. XGBoost was selected as the final model, achieving 67.65% classification accuracy, with an MAE of 15.35 mg/dL**,** RMSE of 20.30 mg/dL**,** and R^2 of 0.7853. The model was integrated with an ESP32-based sensing unit and Raspberry Pi 3 edge inference system for real-time prediction. Hardware-in-the-loop evaluation using 15 participant trials achieved an MAE of 9.87 mg/dL**,** RMSE of 10.42 mg/dL**,** MARD of 6.70%**,** and R^2 of 0.9847. The results demonstrate the feasibility of integrating physiological sensing with machine learning for non-invasive glucose estimation. However, the limited hardware validation sample and the strong contribution of pre-existing medical conditions indicate the need for larger-scale validation before clinical use.

Keywords: Blood glucose estimation, **M**achine learning, **N**on-invasive monitoring

1.0 INTRODUCTION

Diabetes mellitus is a disease that affects several hundred million individuals all over the world and requires constant monitoring of their blood glucose levels to minimize the probability of developing severe complications. Current methods of glucose level measurement are based on an invasive blood sampling technique that utilizes disposable test strips[1].
Recent progress in biomedical sensing and machine learning technologies has allowed scientists to research alternative approaches that are Non-invasive and utilize physiological parameters related to glucose level changes. Parameters like heart rate, blood oxygen saturation, skin temperature, and galvanic skin response show a certain dependence on metabolic states [2].

Machine learning algorithms offer a powerful tool for building nonlinear dependencies between several physiological parameters and glucose level. Compared with traditional mathematical models, data-driven approaches can significantly improve prediction performance by exploiting hidden correlations among multiple sensor measurements [1, 2].

This research aims to develop a machine learning-based non-invasive blood glucose estimation system that combines multiple physiological parameters with embedded hardware for real-time glucose level prediction [3].

2.0 EXPERIMENTAL

2.1 System overview

The proposed system consists of two primary modules:

- Machine learning prediction model
- Embedded hardware acquisition system

Physiological data are collected from ECG, SpO_2, body temperature, and GSR sensors. The processed features are supplied to the trained machine learning model to estimate blood glucose levels. The predicted results will be displayed on an OLED screen, and alerts will be generated when abnormal glucose levels are detected. Figure 1 below shows the architecture diagram of the overall system, while Figure 2 show ai training architecture and Figure 3 shows the data flow architecture of the developed system.

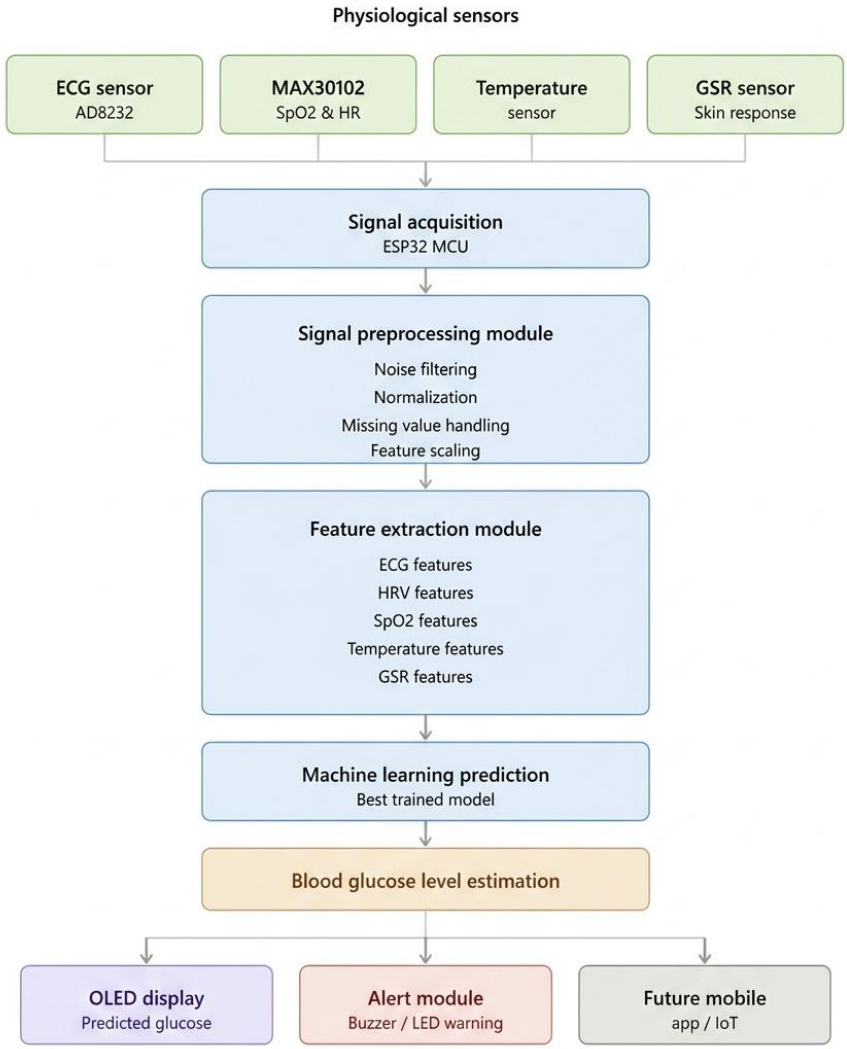


Figure 1: Overall system architecture diagram

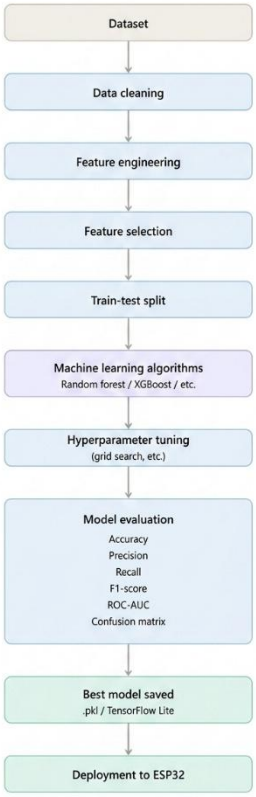


Figure 2: AI training architecture

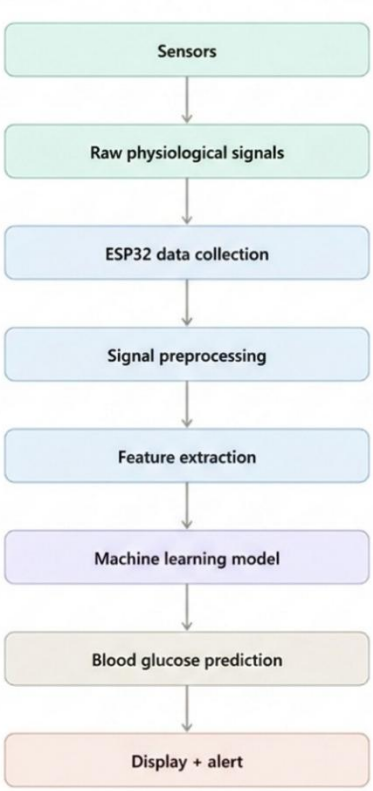


Figure 3: Dataflow architecture

2.2 Machine learning development

The dataset contained 10,000 samples with nine input features: Age, Pre-existing Medical Condition, Activity Level, ECG Heart Rate, ECG HRV, ECG QTc, SpO_2, Body Temperature, and GSR. Numerical features were standardized, and categorical features were one-hot encoded. The data were divided into 80% training and 20% testing, with 2,000 unseen samples reserved for final evaluation. Random Forest and XGBoost were compared, with XGBoost selected as the final model. The selected model used 100 estimators, a learning rate of 0.08, and a maximum depth of 6.

2.3 Hardware development

Selected components and their purpose are listed in Table 1.

Table 1: Hardware components used

Component	Purpose
ESP32	Main controller
Raspberry Pi Model 3	Edge computing device for AI model
MAX30102	SpO_2 & Heart Rate
AD8232	ECG acquisition
DS18B20	Body Temperature
OLED Display	Result Display
Buzzer	Alert Notification

Sensor integration and communication testing have been completed. Embedded software development is ongoing to interface the trained model with the ESP32 platform.
The hardware prototype was implemented using a DOIT ESP32 DEVKIT V1 as the main controller for physiological data acquisition and user interaction. The system integrates an AD8232 ECG sensor**,** MAX30100 pulse oximeter**,** and DHT22 temperature sensor to obtain ECG, heart rate, SpO_2, skin conductance, and body temperature measurements. A 1.3-inch SH1106 OLED display is used to display physiological measurements and glucose predictions, while an active buzzer provides alerts and feedback.
A Raspberry Pi 3 was implemented as the edge computing unit for executing the trained XGBoost model. The ESP32 communicates with the Raspberry Pi through a UART serial connection at 115200 baud. The acquired sensor data are formatted as JSON telemetry and transmitted to the Raspberry Pi for processing.

2.3.1 Hardware integration and real-time operation

During operation, the ESP32 collects physiological measurements and transmits the required parameters to the Raspberry Pi at approximately two-second intervals. The Raspberry Pi processes the received data using the trained XGBoost model and generates a predicted blood glucose value and clinical category. The prediction is then returned to the ESP32 and displayed on the OLED screen. The implemented system therefore provides an integrated workflow from physiological sensing, edge AI processing, and real-time glucose prediction to user display. Figure 4 shows the developed hardware device connected to the ESP32, Raspberry Pi3, sensors, and display.

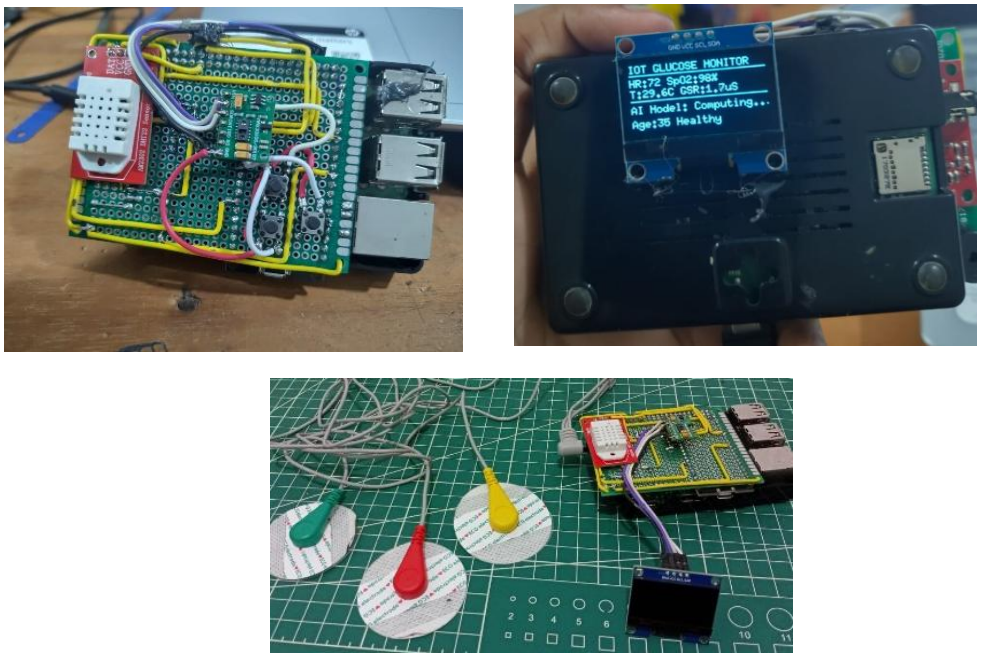


Figure 4: Developed hardware

2.4 Ethical considerations

The study used physiological and clinical information for machine learning development and prototype evaluation. Participant data used for hardware validation were handled

confidentially, and personal identifiers were not included in the analysis. The system is intended for research and estimation purposes only and is not a replacement for clinically approved blood glucose measurement or diagnosis.

3.0 RESULTS AND DISCUSSION

Since the embedded implementation is currently under development, this section presents the results obtained from the completed machine learning phase.

3.1 Model training performance

According to Figure 5 graphs, the selected machine learning model demonstrated stable convergence during training with no significant overfitting observed over 150 training epochs.

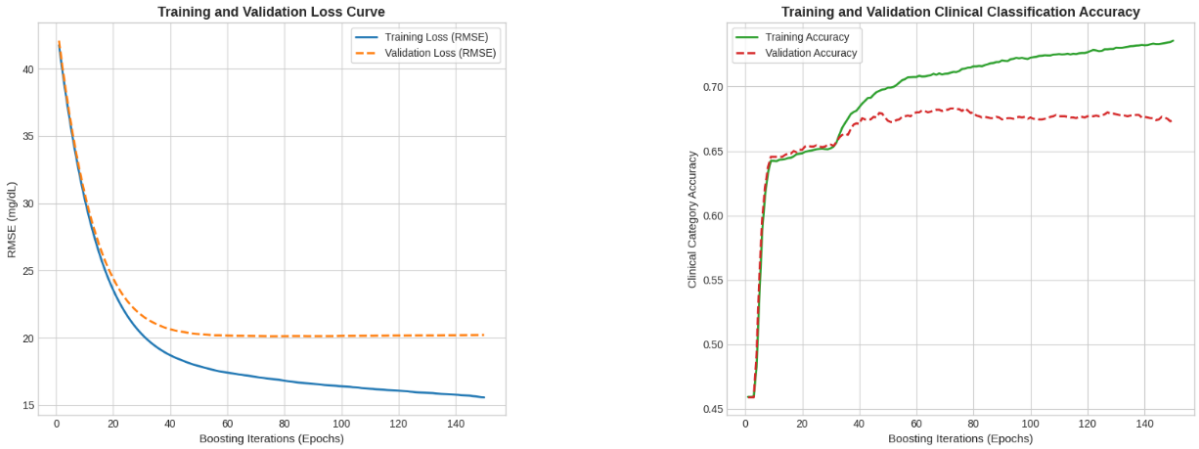


Figure 5: Training and validation loss and accuracy curves

The training results show smooth convergence, with training and validation RMSE decreasing rapidly before stabilizing. Validation accuracy gradually reaches approximately 67–68%, with only a modest gap from training accuracy, indicating limited overfitting and stable generalization.

3.2 Confusion matrix

In figure 6 confusion matrices of the AI model shows sample and normalized confusion matrices.

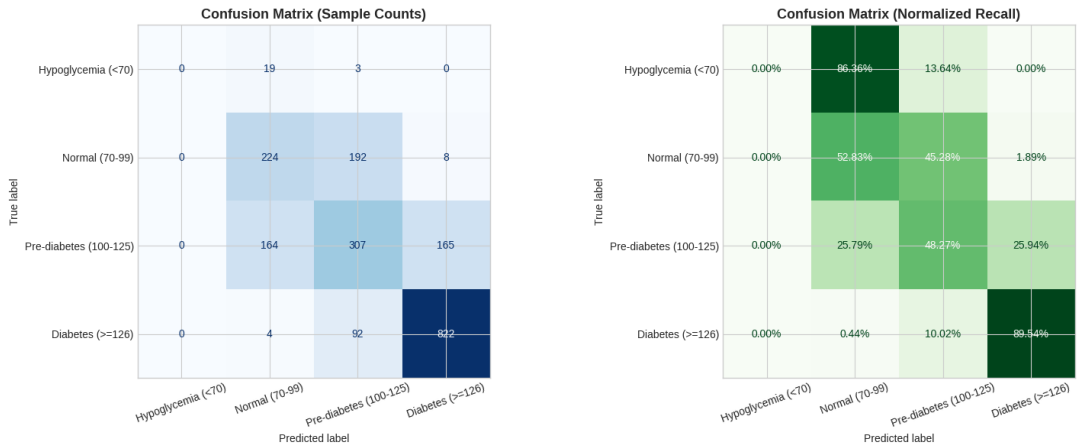


Figure 6: Confusion matrices of the model

The confusion matrices show the strongest performance for the Diabetes (≥126 mg/dL) class, achieving 89.54% recall (822 samples). Normal and Pre-diabetes achieved recalls of 52.83% (224 samples) and 48.27% (307 samples), respectively, while Hypoglycemia achieved 0% recall. Most errors occurred between adjacent Normal and Pre-diabetes categories, indicating difficulty distinguishing borderline glucose levels.

3.3 Performance metrics

The model achieved an overall accuracy of 67.65%, with a weighted F1-score of 0.6669, indicating moderate and reasonably balanced classification performance. The ROC-AUC score of 0.7205 suggests that the model has a fair ability to distinguish between the different classes. Table 2 shows the performance matrix, and Table 3 shows regression metrics of the trained AI model.

Table 2: Performance matrix

Metric	Value
Accuracy	67.65%
Precision (Weighted)	0.6591
Recall (Weighted)	0.6765
F1-Score (Weighted)	0.6669
ROC-AUC (Macro One-vs-Rest)	0.7205

Table 3: Regression matrix

Metric	Value
Mean Absolute Error (MAE)	15.35 mg/dL
Root Mean Squared Error (RMSE)	20.30 mg/dL
Coefficient of Determination (R^2 Score)	0.7853

In addition to the machine learning evaluation, the integrated hardware prototype was evaluated using 15 participant trials by comparing the system-generated glucose estimates with reference clinical measurements. The hardware-in-the-loop evaluation achieved an MAE of 9.87 mg/dL, RMSE of 10.42 mg/dL, MARD of 6.70%, Pearson correlation of 0.9928, and R^2 of 0.9847. These results indicate strong agreement between the prototype estimates and the reference measurements. However, the limited participant sample is insufficient for clinical validation, and further evaluation with a larger population is required [4].

3.4 ROC curve

The ROC analysis produced a macro-ROC-AUC of 0.7205**.** Diabetes showed the best discrimination (AUC = 0.93), followed by Normal (0.78) and Pre-diabetes (0.71).

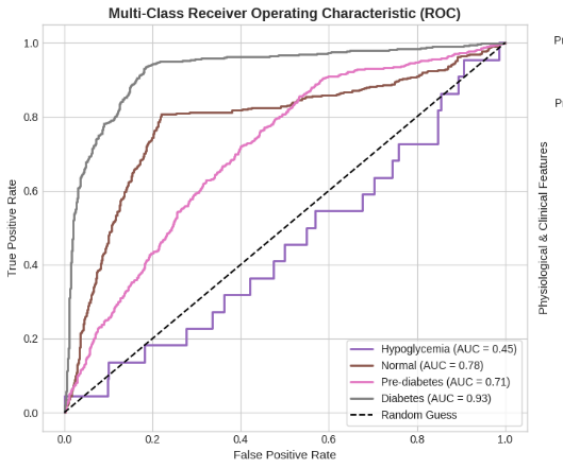


Figure 7: ROC curve

Hypoglycemia achieved a low AUC of 0.45, highlighting the difficulty of detecting this minority class. Figure 7 shows ROC Curve of the trained AI Model.

3.5 Feature importance

The feature importance analysis shows that pre-existing medical conditions were the strongest predictors, with Type 2 Diabetes history contributing most, followed by Pre-diabetic and Type 1 Diabetes history. Among physiological features, GSR had the highest contribution, while ECG features, physical activity, temperature, SpO_2, and age had lower importance. This indicates that the model relies mainly on clinical history while using physiological measurements as complementary predictors. Figure 8 shows feature importance graph of the AI Model.

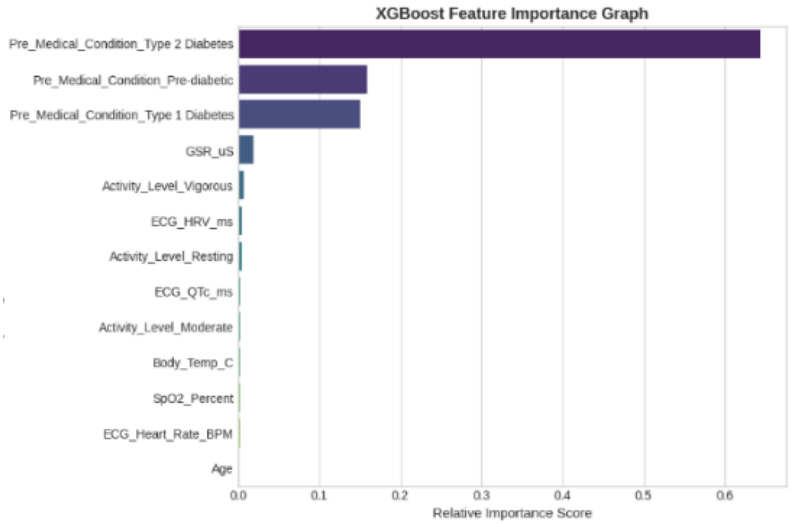


Figure 8: Feature importance

3.6 Hardware implementation and experimental validation

The hardware prototype was successfully integrated with the developed machine learning model. The ESP32 acquired real-time physiological measurements from the ECG, SpO_2, heart rate, GSR, and temperature sensors and transmitted the required data to the Raspberry Pi 3 through UART communication. The Raspberry Pi performed XGBoost inference and returned the predicted glucose value and clinical category to the ESP32 for display on the OLED. Table 4 shows the validation results of the overall system tested with 15 participants [5].

Table 4: Validation metric results

Validation Metric	**Result**
Participants	15
MAE	9.87 mg/dL
RMSE	10.42 mg/dL
MARD	6.70%
Pearson correlation	0.9928
R^2	0.9847

The integrated system was evaluated using 15 participant trials by comparing the system's predicted glucose values with reference clinical measurements. The hardware-in-the-loop evaluation achieved an MAE of 9.87 mg/dL, RMSE of 10.42 mg/dL, MARD of 6.70%, Pearson correlation of 0.9928, and R^2 of 0.9847. These results demonstrate strong agreement between the prototype predictions and the reference measurements, while further validation with a larger participant group is required before clinical deployment [6].

4.0 CONCLUSION

This study developed a machine learning-based non-invasive blood glucose estimation system using physiological, demographic, and clinical features. The XGBoost model achieved 67.65% accuracy, with an MAE of 15.35 mg/dL, RMSE of 20.30 mg/dL, and R^2 of 0.7853.

The implemented prototype integrates an ESP32 sensor unit with a Raspberry Pi 3 for real-time edge-based prediction. Hardware evaluation with 15 participant trials achieved an MAE of 9.87 mg/dL, RMSE of 10.42 mg/dL, MARD of 6.70%, and R^2 of 0.9847. However, the limited sample size requires further validation with a larger population. Feature analysis also showed that pre-existing medical conditions were the dominant predictors, while physiological measurements provided complementary information. Therefore, the system demonstrates feasibility but requires larger-scale clinical validation before practical clinical use.

ACKNOWLEDGEMENTS

Authors would like extend their appreciation to the academic staff and non-academic staff of the Department of Electronics, Faculty of Applied Sciences, Wayamba University of Sri Lanka, for their assistance and support.

REFERENCES

1. Jarman, L., "*Investigating Heart Rate Variability as a Novel Non-Invasive Measure of Blood Glucose Level in Type 1 and Type 2 Diabetes*", Ph.D. dissertation, University of Technology Sydney, Australia, 2023.
2. Rothberg, L. J., Lees, T., Clifton-Bligh, R., and Lal, S., "Association between heart rate variability measures and blood glucose levels: Implications for noninvasive glucose monitoring," *Diabetes Technology & Therapeutics*, 2016, vol. 18, no. 6, pp. 366–376.
3. Nanayakkara, N. D., Munasingha, S. C., and Ruwanpathirana, G. P., "Non-invasive blood glucose monitoring using a hybrid technique," in *Proc. MERCon*, Sri Lanka, 2018, pp. 7–12.
4. Malik, S., Khadgawat, R., Anand, S., and Gupta, S., "Non-invasive detection of fasting blood glucose level via electrochemical measurement of saliva," *SpringerPlus*, 2016, vol. 5, Art. no. 701.
5. Saad, W. H. M., *et al.*, "Analysis on continuous wearable device for blood glucose detection using GSR sensor," *International Journal of Nanoelectronics and Materials*, 2020, vol.13, pp. 9-16.
6. Schwarz, Y., Konvalina, N., and Tirosh, A., "A pilot trial to evaluate the accuracy of a novel non-invasive glucose meter," *Sensors*, 2021, vol. 21, no. 20, Art. no. 6704.

Proc. Annual Symposium on Research & Industrial Training, 13 (2026) 71 - 78
Department of Electronics – Wayamba University of Sri Lanka

IOT-BASED REAL-TIME MONITORING AND ALERT SYSTEM FOR SAFETY IN MINING TUNNELS

S.S.P.P. De Silva*, S.R.L. Gunawardhana

Department of Electronics, Wayamba University of Sri Lanka, Kuliyapitiya, Sri Lanka

*spinipapriyantha2021@gmail.com

ABSTRACT

Underground mining environments are extremely hazardous due to toxic gases such as carbon monoxide (CO), carbon dioxide (CO_2), and ammonia (NH_3), elevated temperatures and humidity, and the risk of sudden falls. Existing monitoring systems often focus only on environmental parameters or suffer from communication failures inside tunnels. This study proposes an Internet of Things (IoT)-based safety system intended for underground miners. The system integrates a portable environmental sensor node (ESP32 with MQ9, MQ135, and DHT22) for gas, temperature, and humidity measurements and a wearable wristband (ESP32-C3 with MAX30102 and MPU6050) for heart-rate monitoring and fall detection with local alarms, optional mesh relay nodes for range extension, and a surface gateway that publishes data via MQTT to a real-time web dashboard. Local communication relies on the ESP-NOW protocol, allowing local monitoring and alerting without Internet connectivity. Dual local and remote alert mechanisms provide immediate personal protection and centralized supervision. The design enhances practicality and reliability in underground settings where dangerous conditions and communication constraints are prevalent by integrating low-cost, compact, and dependable sensing with local wireless technology.

Keywords: Underground mine safety, **I**nternet of things, **M**esh relay nodes

1.0 INTRODUCTION

Underground mining is one of the most hazardous working environments, exposing miners to hazardous gases such as CO, CO_2, and NH_3, high temperatures and humidity, and sudden falls. These risks can become life-threatening, while the confined nature of underground tunnels makes reliable communication with surface personnel difficult [1, 2]. Many existing monitoring systems depend on Internet, cellular, Wi-Fi, or cloud connectivity, which may be unreliable or unavailable underground [1,2,3]. Although Bluetooth and single-hop ZigBee provide local communication, their limited coverage can be inadequate in complex tunnel environments [4, 5].

Previous studies have demonstrated IoT-based mine monitoring, worker tracking, environmental sensing, and wearable health monitoring. Jiang et al. focused on continuous underground worker tracking [1], while Cacciuttolo et al. investigated LoRaWAN for underground monitoring [6]. Dohare et al. reviewed wireless communication and environmental monitoring technologies and noted that many systems mainly focus on gas detection rather than worker health [2]. Wang et al. demonstrated the feasibility of combining physiological and environmental monitoring in a wearable device [7]. Sathishkumar et al. highlighted connectivity challenges associated with Wi-Fi in underground tunnels [3], while Rudrawar et al. and Ansari et al. demonstrated ZigBee- and PIC-based monitoring systems with local alarms [4, 5].

Overall, existing research shows the importance of monitoring both environmental conditions and worker safety. However, these functions are often implemented separately, and systems relying on external communication infrastructure may lose important monitoring and alert capabilities when connectivity is unavailable. Therefore, a research gap remains for an integrated system that can monitor gases, heart rate, falls, and zone-based location while providing both local and remote alerts without depending on Internet connectivity underground.

This study proposes an IoT-based real-time monitoring and alert system that integrates a portable environmental sensing node, a wearable wristband for heart rate and fall detection, optional relay nodes, and a surface MQTT gateway with a web-based dashboard. ESP-NOW is used for local communication between devices, enabling essential monitoring and alert functions to continue even when Internet connectivity is unavailable underground.

2.0 EXPERIMENTAL

2.1 System overview

The proposed mine safety kit consists of four main hardware components: a portable environmental sensor node, a wearable wristband, mesh relay nodes, and a surface Gateway. The portable environmental sensor node continuously measures environmental carbon monoxide, carbon dioxide, ammonia, temperature and humidity, and tags each reading with a zone identifier corresponding to the worker's location within the mine (e.g., Zone-1, Zone-2). This data, together with heart-rate and fall-detection data collected at the Wearable Wristband, is transmitted over ESP-NOW, a connectionless Wi-Fi-based protocol that does not require an active Internet connection or a router, making it suitable for underground use. Mesh Relay Nodes may be deployed at intervals along long tunnels to forward data over multiple hops, extending the effective communication range beyond direct line-of-sight. The Surface Gateway receives all data arriving via ESP-NOW at the mine entrance and republishes it using MQTT to a cloud-connected web dashboard [8]. Figure 2.1 shows the overall block diagram of the system.

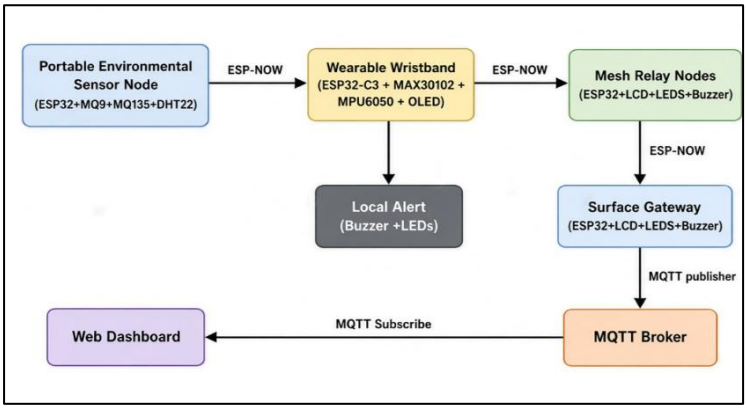


Figure 2.1: Block diagram of the proposed IoT-based mine safety kit showing the local ESP-NOW alerting path (Portable Environmental Sensor Node- wearable wristband- local alert) and the remote supervisory path (Mesh Relay Node(s) - Surface Gateway - MQTT - Web Dashboard

2.2 Hardware implementation

Based on the identified functional requirements, the system was developed by integrating environmental sensing, physiological monitoring, processing, communication, power management, and alerting functions into a compact wearable and portable platform. The ESP32 was selected as the main microcontroller for the Portable Environmental Sensor Node, Mesh Relay Nodes, and Surface Gateway, while the smaller ESP32-C3 was used for the Wearable Wristband because of its compact form factor and suitability for wearable applications. The sensing and actuator modules include MQ9 and MQ135 gas sensors for gas monitoring, a DHT22 sensor for measuring temperature and humidity, a MAX30102 sensor for heart-rate monitoring, and an MPU6050 accelerometer and gyroscope for movement and fall detection. An Organic Light-Emitting Diode (OLED) display, buzzer, and LEDs are incorporated to provide local status information and immediate visual and audible alerts. The devices are powered by rechargeable battery packs. The portable environmental sensor node uses 3.7V Li-ion batteries regulated by an LM2596 DC-DC buck converter, while the Wearable wristband uses a 3.7V Li-Po battery with an MT3608 DC-DC boost converter. The Mesh Relay Nodes and Surface gateway are each powered by MT3608 DC-DC boost converters to provide the required 5V supply level.

Underground communication is implemented using the ESP-NOW protocol, a connectionless, low-power wireless communication method that operates without requiring Internet access or conventional Wi-Fi infrastructure. This allows the Portable Environmental Sensor Node, Wearable Wristband, Mesh Relay Nodes, and Surface Gateway to exchange data locally within the underground environment. Once the Surface Gateway receives the data, it forwards the information to the monitoring platform using the MQTT publish-subscribe protocol, where the collected data can be displayed on the web dashboard. Zone-based location awareness is achieved by assigning each Portable Environmental Sensor Node a unique zone identifier in the firmware.

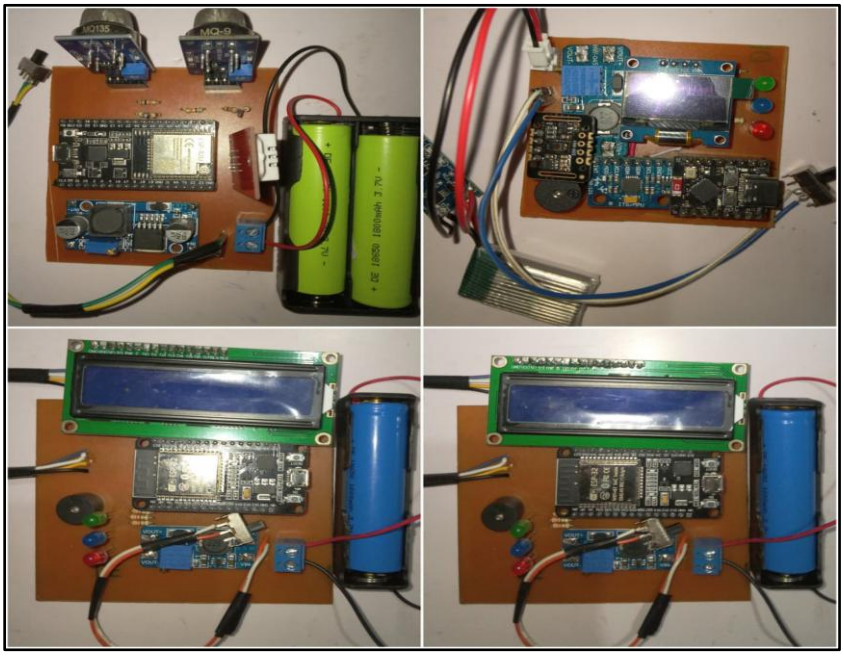


Figure 2.2: Assembled prototype of the portable environmental sensor node, wearable wristband, mesh relay node and surface gateway

The identifier is transmitted along with the sensor data, allowing supervisors to approximately identify the underground zone associated with a monitored worker or hazardous condition. Figure 2.2 shows the assembled prototype of the main hardware units.

2.3 Communication architecture

Two communication stages are used. Within the mine, ESP-NOW carries all links so that local alerting continues during complete loss of external connectivity. At the Surface Gateway, data are published over MQTT to a broker and consumed by the web dashboard. This design separates the safety-critical local path from the remote supervisory path, which depends on surface connectivity but is not required for the worker's immediate protection.

2.4 Software implementation

The employee-facing software runs on the wearable wristband; environmental readings received over ESP-NOW and locally measured heart rate and motion data are displayed on an OLED screen, and the buzzer and LEDs are activated whenever a monitored parameter crosses a predefined threshold. On the surface, a web dashboard consumes the MQTT stream and provides live sensor values, threshold-based alerts with audible warnings, and historical analysis over daily, weekly, and monthly periods, together with CSV export for further analysis. Each Pocket Environmental Sensor Node reports a zone identifier with its readings.

Functional testing was performed on the integrated prototype with a single registered worker (W001) and a single zone (Zone-1). Danger thresholds were configured in the dashboard as listed in Table 3.1. Live cards, history log, alert log, and worker status were observed while sensor readings were varied across the CO threshold and with valid and invalid finger contact on the MAX30102. Figure 2.3 shows the live monitoring parameter card of the web dashboard.



Figure 2.3: Live monitoring parameter cards showing temperature, humidity, CO, CO_2, NH_3, and heart-rate readings with status indication and trend

3.0 RESULTS AND DISCUSSION

The complete prototype was assembled and integrated. End-to-end communication from sensor collection through ESP-NOW, MQTT publishing, and live dashboard visualization was demonstrated under various conditions.

Table 3.1: Configured alert thresholds used during testing

Parameter	**Normal**	**Warning**	**Danger**
CO	< 35ppm	35-50ppm	> 50ppm
CO_2	< 1000ppm	1000ppm – 500ppm	> 500ppm
NH_3	< 15ppm	15ppm – 25ppm	>25ppm
Temperature	35 °C	35 °C - 40°C	>40°C
Humidity	80% RH	80-90% RH	>90% RH
Heart rate	60bpm - 100bpm	High: 100bpm – 120bpm Low: 50bpm – 59bpm	High: > 120bpm Low <50bpm

As shown in Table 3.1, three-level thresholds were applied for each monitored parameter. During testing, the live parameter cards displayed the configured threshold conditions correctly. CO readings at or below 50 ppm, such as 49 ppm, were classified as Warning, while readings above the threshold, including 53, 58, and 63 ppm, were classified as Danger. The temperature, humidity, CO_2, and NH_3 readings remained below their respective thresholds and were therefore classified as Normal. For heart-rate monitoring, the system displayed "No finger" when the sensor was not in contact with a finger. When contact was detected, heart-rate values within the 50–120 bpm range, such as 63 bpm and 92 bpm, were displayed correctly.

Table 3.2: Sample of logged historical records (Worker Woo1, Zone-1)

Time	**Temp (**°C)	CO (ppm)	CO_2 (ppm)	NH_3 (ppm)	Fall	Status
10:03:28	24.4	49	460	6	No	WARNING
10:03:20	24.4	53	453	5	No	DANGER
10:03:19	24.4	53	453	5	No	DANGER
10:03:17	24.4	50	473	7	No	DANGER

Table 3.2 presents a sample of consecutive logged records for Worker W001 in Zone-1, illustrating how CO status changed between Warning and Danger as the reading crossed the 50 ppm threshold. During the test session of approximately 45 minutes, the dashboard recorded 241 data entries, including 26 historical alerts, and reported a system uptime of 99.9%. The Alerts view showed 36 Critical, 0 Warning, and 2 Informational alerts, all associated with Worker W001 in Zone-1. Alert messages such as "High CO Level Detected! CO = 59 ppm" corresponded with the defined 50 ppm threshold. These results indicate that the dashboard successfully received streamed data, applied the configured parameter-specific thresholds, and presented both real-time and historical alerts. Importantly, the Wearable Wristband generated local alerts independently of the surface MQTT connection, meaning that essential worker protection does not depend on continuous cloud or internet connectivity. Figure 3.1 shows the history view of the web dashboard.



Figure 3.1: History view of the web dashboard showing total records (263), historical alerts (29), system uptime (99.9%), and logged Zone-1 sensor readings with Danger classification

Compared with Wi-Fi-based systems, which can experience connectivity difficulties underground [3], and single-hop ZigBee systems with limited coverage [4], ESP-NOW provides a connectionless local communication link suitable for short- to medium-range underground communication. Relay nodes can also be used to extend coverage where necessary. Although LoRaWAN offers longer-range communication at lower data rates [6], the proposed approach focuses on low-cost implementation and the combination of local and remote alerting for small- and medium-scale mining operations.

The testing also had several limitations. Only one worker and one zone were used, so multi-worker, multi-zone, and multi-hop communication were not evaluated. The accuracy of the gas measurements was not verified against a reference instrument; therefore, MQ9 and MQ135 readings should be regarded as threshold-based indicators until further calibration and validation are completed. The communication range under actual underground conditions, including attenuation caused by surrounding rock, was also not measured. In addition, the occasional persistence of a Danger status after the CO concentration had fallen suggests that the alert hysteresis and multi-parameter logic require further investigation. Consequently, the current laboratory-scale results are not sufficient to support stronger quantitative claims about system performance in real underground mining environments.

4.0 CONCLUSION

This research presented the design and implementation of an IoT-based real-time monitoring and alert system for mine safety, aimed at protecting underground workers who face toxic gases, extreme climate conditions, and fall hazards or the risk of falls. The study addressed the significant problem of incomplete or Internet-dependent monitoring by introducing an integrated IoT monitoring platform that combines environmental sensing with worker health monitoring.

The proposed system successfully integrated portable environmental nodes, a wearable health and fall-detection device, optional mesh relays, and a surface MQTT gateway connected to a real-time web dashboard. Local ESP-NOW communication allows local operation without Internet connectivity, while dual local and remote alerts provide both immediate personal protection and centralized supervision. Zone-based location awareness further enhances situational awareness for surface personnel.

The major achievements of this work include demonstrating that environmental and physiological parameters can be monitored effectively within a single low-cost IoT platform, achieving reliable local communication inside tunnels, and proving the feasibility of a scalable assistive safety solution suitable for mining operations in Sri Lanka. Future work will focus on improving sensor calibration under varying conditions, optimizing mesh relay placement and power consumption, expanding the set of monitored parameters, and conducting extended field trials to validate long-term reliability in real underground environments.

ACKNOWLEDGEMENT

The authors express their sincere gratitude to the lecturers and staff at the Department of Electronics, Faculty of Applied Sciences, Wayamba University of Sri Lanka, for their invaluable guidance and support throughout this research.

REFERENCES

1. Jiang, Y., Chen, W., Zhang, X., Zhang, X., Yang, G., “Real-time monitoring of underground miners’ status based on mine IoT system,” *Sensors,* 2024, vol. 24, no. 3, Art. no. 739.
2. Dohare, Y. S., Maity, T., Das, P. S., Paul, P. S., "Wireless communication and environment monitoring in underground coal mines—review", *IETE Technical Review*, 2015, vol. 32, no. 2, p. 140–150.
3. Sathishkumar, N., Manoj, A. M., Muniraj, K., Naveenkumar, M., Praveen, C., "Safety monitoring system in coal mine using IoT", *Journal of Physics: Conference Series*, 2021, vol. 1916, Art. no. 012196, doi: 10.1088/1742-6596/1916/1/012196.
4. Rudrawar, M. S., More, S. B., Jadhav, V. Y., "Coal mine safety monitoring and alerting system with smart helmet", *ITM Web of Conferences*, 2022, vol. 44, p. 1–8.
5. Ansari, J., Priya, A., Manjunathan, S., "IoT-based coal mine safety monitoring and alerting system", *International Journal of Scientific Research in Science, Engineering and Technology*, 2021, vol. 8, p. 1–7.
6. Cacciuttolo, C., Atencio, E., Komarizadehasl, S., Lozano-Galant, J. A., "Internet of Things Long-Range-Wide-Area-Network-based wireless sensors network for underground mine monitoring", *Sensors*, 2024, vol. 24, no. 21, Art. no. 6971.
7. Wang, L., Zhu, M., Song, D., "Design of a wearable IoT-based safety monitoring system for coal mine workers", *IEEE Access*, 2019, vol. 7, p. 31396–31404.
8. Levush, P., Luchechko, A., "Performance evaluation of ESP-NOW for low-latency indoor IoT systems", *Academic Journals and Conferences*, 2026, vol. 11, no. 1, p. 1–5.

Proc. Annual Symposium on Research & Industrial Training, 13 (2026) 79 - 86
Department of Electronics – Wayamba University of Sri Lanka

TRUE RANDOM NUMBER GENERATOR USING TRANSISTOR NOISE FOR SECURE OTP GENERATION

L.K. Abeyrathna*, W.A.S. Wijesinghe

Department of Electronics, Wayamba University of Sri Lanka, Kuliyapitiya, Sri Lanka

*lakshmiabey2000@gmail.com

ABSTRACT

Randomness is critical to many applications in authentication and other security areas, since predictable random numbers may reduce the security of a system. This study presents the design and implementation of a cost efficient true random number generation system based on transistor noise as a source of physical randomness. The noise signal was amplified and acquired using a digital data acquisition system controlled by ESP32 microcontroller. The consecutive samples were then combined and processed to generate a binary sequence consisting of random bits. One million bits were generated for statistical evaluation. The resulting binary sequence contained 499,934 zeros and 500,066 ones, showing an almost equal distribution between the two values. The random sequence was statistically evaluated using a standard randomness testing procedure, and all 17 evaluated statistical test categories (100%) met the required minimum pass-rate criteria, indicating satisfactory statistical randomness. Some individual results did not meet the selected acceptance threshold, indicating that further refinement and testing may be required. Finally, the generated random data was used to generate six digit one time passwords. Overall, the results demonstrate that transistor noise can serve as a practical physical source for random bit generation in low cost security applications.

Keywords: **T**ransistor noise, **T**rue random number generation, **E**SP32 microcontroller

1.0 INTRODUCTION

Random number generation is an important requirement in modern security systems, particularly for applications such as authentication, encryption, and secure password generation. Conventional Pseudo Random Number Generators (PRNGs) depend on deterministic algorithms and therefore require a reliable initial seed to produce unpredictable sequences. True Random Number Generators (TRNGs), in contrast, obtain randomness from physical phenomena and can provide a non deterministic source of random data. However, many hardware based random number generators require specialized components or complex circuits, which can increase system cost and implementation complexity [1,2].

Electrical noise generated by electronic devices provides a potential physical source of randomness. In particular, transistor noise can produce unpredictable voltage fluctuations that can be amplified and digitally sampled for random bit generation [3]. However, the noise signal is typically small and its usefulness as an entropy source depends on suitable amplification, signal acquisition, and bit extraction methods. Therefore, a simple and low cost TRNG implementation must be evaluated to determine whether the generated data provides sufficient statistical randomness.

The main objective of this study is to design and implement a low cost True Random Number Generator using transistor noise, a two stage LM741 amplifier, and the built in 12-bit Analog to Digital Converter (ADC) of an ESP32. The study investigates whether the amplified transistor noise can provide sufficient physical entropy to generate statistically acceptable

random bit sequences, which are further demonstrated through six digit One Time Password (OTP) generation.

2.0 METHODOLOGY

2.1 Proposed TRNG architecture

The proposed system uses transistor noise as the physical entropy source. The system consists of a transistor noise source, a two stage amplifier, an ESP32 microcontroller, and a random bit generation process. The amplified noise is sampled using the ESP32's built in 12-bit ADC and processed to generate a binary sequence. The overall architecture of the proposed TRNG system is illustrated in the block diagram shown in Figure 1.

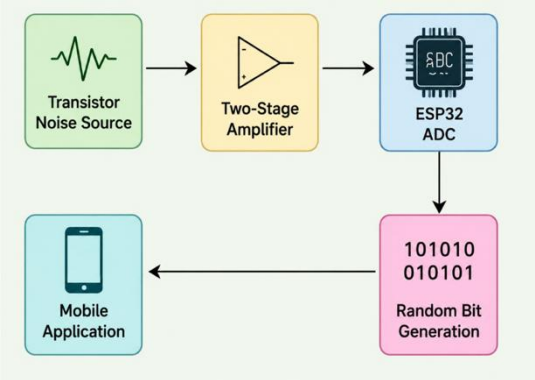


Figure 1: Block diagram of the system

2.2 Hardware and data acquisition

The physical entropy source of the proposed system was a 2N3904 NPN transistor, operated under reverse bias conditions to generate transistor noise. The random movement of charge carriers under this condition produces small, unpredictable electrical fluctuations, which form the physical source of randomness [4]. The transistor noise generator circuit used to produce the entropy source is shown in Figure 2. Since the generated noise had a very low amplitude, it was amplified using a two stage LM741 amplifier. The circuit configuration of the two stage amplifier is shown in Figure 3. The amplified signal was then passed through a protection and signal conditioning circuit before being applied to the ESP32, ensuring that the input signal remained within the safe operating range of the ADC[5,6].

The ESP32's built in 12 bit ADC was used to convert the amplified and conditioned noise signal into digital samples through GPIO 34 (ADC input pin), producing values from 0 to 4095.

2.3 Random bit generation

The amplified transistor noise was sampled using the ESP32's built in 12-bit ADC through GPIO 34. Consecutive ADC samples were combined using an XOR operation to reduce direct dependence on individual samples[7]. The 12-bit XOR output was processed bit by bit from the least significant bit to the most significant bit, and the extracted bits were sequentially accumulated into a 32 bit random pool. Sampling continued until 32 random bits were obtained, with a 100 µs interval between ADC readings. No additional debiasing or whitening was applied. The generated 32 bit random value was then used for six digit OTP generation by applying a modulo operation with 1,000,000.

2.4 Randomness testing

The randomness of the produced string of bits was determined by using the Statistical Test Suite for Random and Pseudorandom Number Generators, specified in NIST SP 800-22. A test was conducted on a string of 1,000,000 bits produced using various statistical tests such as frequency test, block frequency test, runs test, longest run test, rank test, FFT test, approximate entropy test, serial test, and linear complexity test[8].

2.5 Software implementation

The software implementation was developed to acquire the digitized noise samples from the ESP32 and process them into random binary data. The acquired samples were converted into binary values using the defined bit extraction method and stored for randomness testing. The generated random data was also used to demonstrate one-time password generation through the developed application.

3. RESULTS AND DISCUSSION

3.1 Complete system prototype

The full prototype design of the proposed system based on noise generation from a transistor to generate random numbers has been successfully developed and tested. The system comprises a transistor for the noise generation, a two stage amplification using LM741 amplifier, and an ESP32 microcontroller for data acquisition and random bit generation. The actual prototype used is depicted in Figure 4 below.

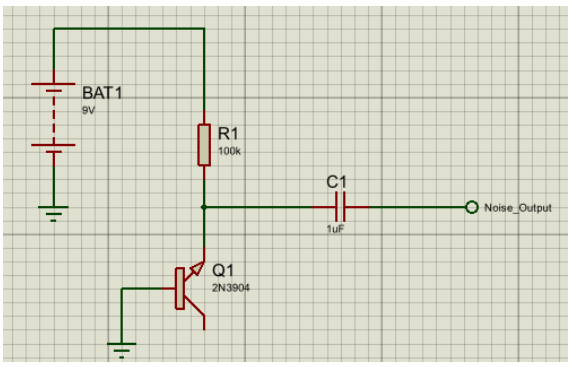


Figure 2: Circuit diagram of the Noise Generator

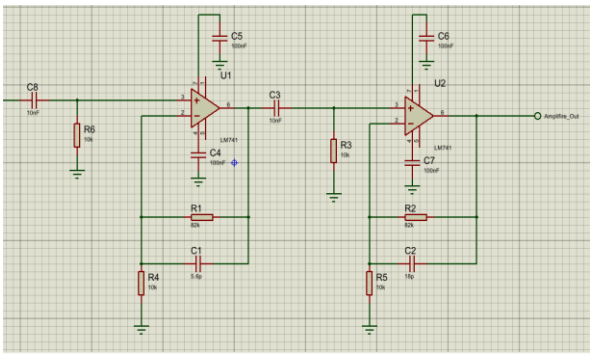


Figure 3: Circuit diagram of the Two stage Amplifier

3.2 Analog noise measurements

The frequency response of the two stages of the amplifier was obtained using a constant input of 0.05 Vpp at various frequencies. The observed gain of the amplifier increased with increase in frequency and had a peak gain of 99.2 at 15 kHz, at which point the output voltage was 4.96 Vpp. After 15 kHz, the gain started to fall off. This test helped in finding the region of operation of the amplifier and its capacity to amplify the transistor noise signal.

3.3 Noise source and amplifier circuit output

Initially, the noise signals generated by the transistor were monitored using an oscilloscope, and it had very minimal voltage changes. However, since the noise signal had minimal voltage, it could not be obtained using the ESP32 and thus, an LM741 amplifier was utilized to amplify the signal. The amplifier amplified the noise signal with a gain of about 100. The output waveform of the transistor noise circuit and the amplified noise signal are shown in Figures 5 and 6, respectively.

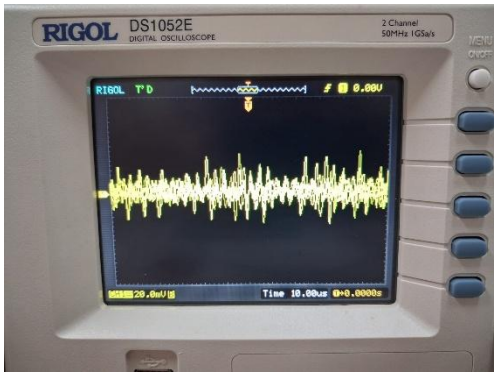


Figure 5: Output waveform of the Noise Circuit

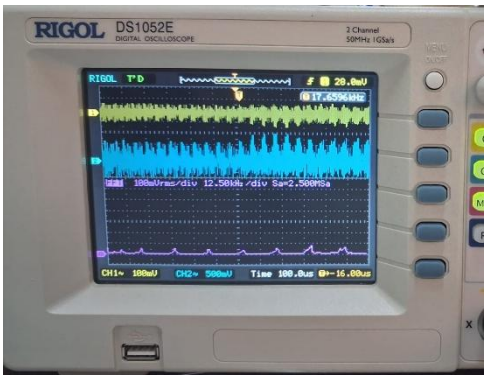


Figure 6: Output waveform of the Amplifier Circuit

3.4 Extracted random bit characteristics

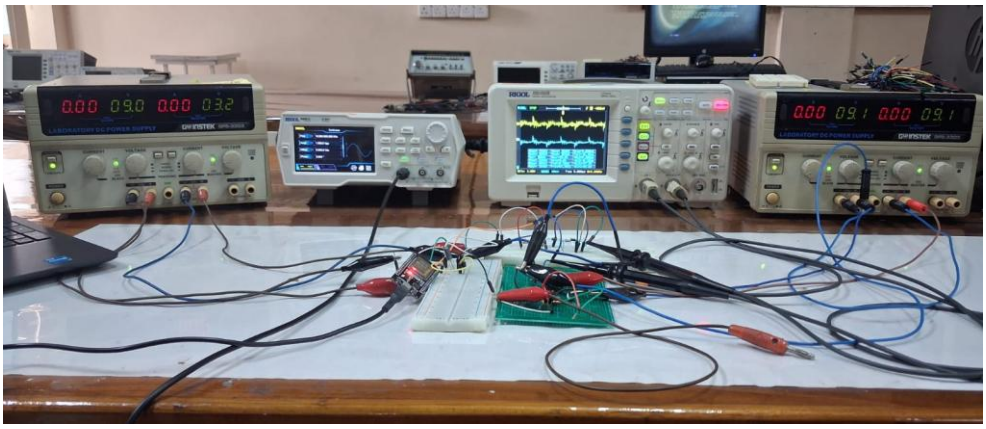


Figure 4: Complete prototype of the proposed transistor noise based random number generation system.

In total, 1,000,000 random bits were obtained from the collected ADC samples. These random bits contained 499,934 zeros (49.9934%) and 500,066 ones (50.0066%), which shows that there was nearly equal distribution of the bits. This shows the presence of a binary sequence that can be tested for randomness. The output random number sequence is given in Figure 7.

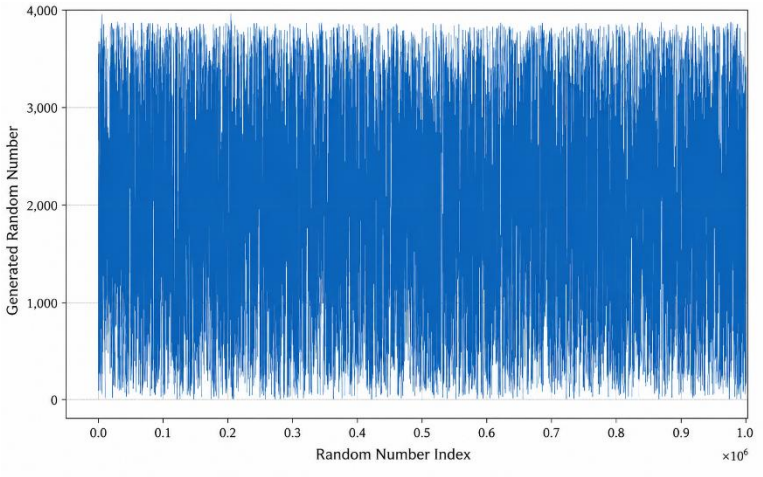


Figure 7: Generated Random Number Sequence

3.5 Statistical randomness results

The 1,000,000 bit generated data was analyzed using the NIST SP 800-22 Statistical Test Suite. The total number of statistical test categories analyzed was 17, and all the 17 categories (100%) fulfilled the minimum pass rate criteria required. Proportions of 10/10 and 9/10 were attained in individual subtests while the Random Excursions test obtained a minimum observed proportion of 6/7. The results of the NIST statistical tests on the generated 1,000,000-bit data set are shown in Table 1 below.

Table 1: NIST statistical test results for the generated 1,000,000 bit sequence

Statistical Test	**P-value**	**Pass Proportion**	**Result**
Frequency	0.739918	10/10	Pass
Block Frequency	0.035174	10/10	Pass
Cumulative Sums – Forward	0.213309	10/10	Pass
Cumulative Sums – Reverse	0.739918	10/10	Pass
Runs	0.534146	10/10	Pass
Longest Run of Ones	0.350485	10/10	Pass
Binary Matrix Rank	0.534146	10/10	Pass
Discrete Fourier Transform (FFT)	0.911413	10/10	Pass
Non-overlapping Template Matching	—	Mostly 9/10–10/10	Pass
Overlapping Template Matching	0.739918	10/10	Pass
Maurer's Universal	0.739918	9/10	Pass
Approximate Entropy	0.534146	10/10	Pass
Random Excursions	—	6/7–7/7	Pass
Random Excursions Variant	—	7/7	Pass
Serial – Test 1	0.739918	10/10	Pass
Serial – Test 2	0.534146	10/10	Pass
Linear Complexity	0.911413	10/10	Pass

From the results of Table 1 above, it is clear that all the 17 statistical test categories evaluated met the minimum pass rate criteria for their respective sample sizes required by the NIST Statistical Test Suite. Even though some individual subtests had a pass proportion of 9/10 while the Random Excursions test had a minimum proportion of 6/7, these results were still within the acceptable criteria. Consequently, the generated 1,000,000 bit sequence demonstrated satisfactory statistical characteristics across the evaluated randomness tests.

3.6 OTP application demonstration

The generated random numbers were further employed for the demonstration of a practical application of the proposed TRNG system using the generation of a six digit OTP. In order to generate a six digit OTP, a random number generated in 32 bits using the generated samples of transistor noise was applied for modulo division with 1,000,000. The generated OTP was first displayed on the ESP32 Serial Monitor to confirm the generation of a random number and OTP. The OTP was further displayed on the developed mobile application to show the usage of the generated random data in a practical authentication related application. The generated OTP on the Serial Monitor and mobile application are provided in Figures 8 and 9, respectively.

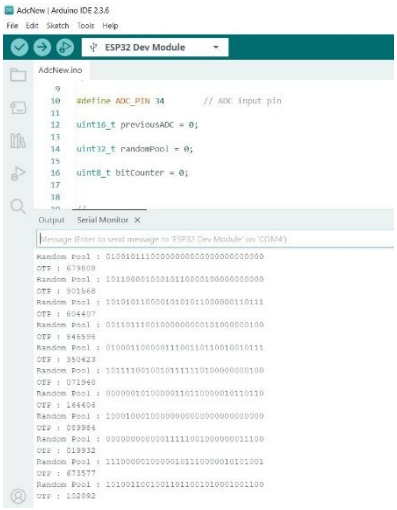


Figure 8: Generated OTP displayed system through the serial monitor



Figure 9: Display mobile application

However, even though the experiment shows that the noise generated by the transistor is capable of being used to generate random bits, there are certain shortcomings of the described approach. The noise and the amplified signal could be influenced by the environmental noise, variations of the power supply voltage, and changes in the operating condition of the transistor. Also, since the randomness check was performed using only 1,000,000 bits, not all of the Random Excursions test results have exceeded the chosen threshold.

4.0 CONCLUSION

This paper described the development of a simple TRNG design based on transistor noise. The developed device consists of the reverse biased transistor as the physical entropy source, LM741 amplifier of two stages, and the 12 bit ADC of the ESP32. One million bits were

randomly generated based on the collected noise values through the use of the NIST Statistical Test Suite. The analysis of the generated data revealed that the number of zeros and ones is almost equal. All 17 evaluated statistical test categories met the required minimum pass rate criteria, indicating that transistor noise can be used as a physical entropy source for generating statistically acceptable random bits. The random values obtained were also used for OTP generation in a mobile application.

The main achievement of this research was demonstrating that a simple and economical analog front end based on transistor noise can be effectively interfaced with an ESP32 to generate statistically acceptable random bit sequences. However, the performance of the system can be further improved by reducing the effects of environmental and power supply variations, optimizing the noise sampling and bit extraction techniques, and conducting long term testing under different operating conditions.

ACKNOWLEDGEMENTS

The authors would like to thank all academic and non-academic staff members of the Department of Electronics, Faculty of Applied Sciences, Wayamba University of Sri Lanka, for their support, guidance, and assistance during this research study.

REFERENCES

1. Bucci, M., and Luzzi, R., *Fully digital random bit generators for cryptographic applications*, *IEEE Transactions on Circuits and Systems I: Regular Papers*, vol. 50, no. 11, pp. 1451–1456, Nov. 2003, doi: https://doi.org/10.1109/TCSI.2003.818614.
2. Dichtl, M., and Golić, J., High-speed true random number generation with logic gates only, in *Cryptographic Hardware and Embedded Systems – CHES 2007*, Springer, 2007, pp. 45–62, doi: https://doi.org/10.1007/978-3-540-74735-2_4.
3. Kim, S. I., Kim, M. S., Lee, D. H., Ryu, S. T., and Choi, Y. K., Cryptographic transistor for true random number generator with low power consumption, *Science Advances*, vol. 10, no. 8, Art. no. eadk6042, Feb. 2024, doi: https://doi.org/10.1126/sciadv.adk6042.
4. Liu, J., Xie, J., Chao, L., Ding, P., Chen, X., and Feng, H., Min-entropy estimation for semiconductor superlattice true random number generators, *Scientific Reports*, vol. 12, Art. no. 2948, Feb. 2022, doi: https://doi.org/10.1038/s41598-022-06815-2.
5. Ewert, M., A random number generator based on electronic noise and the Xorshift algorithm, in *Proceedings of the 2018 VII International Conference on Network, Communication and Computing*, 2018, doi: https://doi.org/10.1145/3301326.3301359.
6. Onsemi, *2N3904 NPN General-Purpose Amplifier*, Semiconductor Components Industries, LLC, Datasheet. https://www.onsemi.com/pdf/datasheet/2n3904-d.pdf [Accessed: 2026-08-27].
7. Liyu, J., Maoxiang, Y., Yuan, X., Lifa, S., Yingchu, L., and Huaguo, L., A dynamically reconfigurable entropy source circuit for high-throughput true random number generator, *Microelectronics Journal*, vol. 133, Art. no. 105690, 2023, doi: https://doi.org/10.1016/j.mejo.2023.105690.
8. Bassham III, L. E., Rukhin, A., Soto, J., Nechvatal, J., Smid, M., Barker, E., Leigh, S., Levenson, M., Vangel, M., Banks, D., Heckert, N., Dray, J., and Vo, S., *A Statistical Test Suite for Random and Pseudorandom Number Generators for Cryptographic Applications*, NIST Special Publication 800-22 Revision 1a, National Institute of Standards and Technology, Gaithersburg, MD, USA, Apr. 2010, doi: https://doi.org/10.6028/NIST.SP.800-22r1a.

Proc. Annual Symposium on Research & Industrial Training, 13 (2026) 87 - 94
Department of Electronics – Wayamba University of Sri Lanka

SMART ACADEMIC DOCUMENT SUBMISSION LOCKER USING IMAGE PROCESSING AND IOT

U.S. Weeragoda*, M.A.A. Karunarathna

Department of Electronics, Wayamba University of Sri Lanka, Kuliyapitiya, Sri Lanka

*umashasandeepani2000@gmail.com

ABSTRACT

Manual collection of physical academic assignments in educational institutions is prone to submission disputes, lost documents, unauthorised multiple submissions, and administrative labour. This paper presents the design, implementation, and empirical evaluation of an automated document submission locker system integrating Internet of Things (IoT) sensors, computer vision, and mechanical sorting. The physical apparatus features an optical entry beam-break sensor (Laser-LDR pair) that detects document insertion and initiates a stepper-motor conveyor belt within a light-sealed locker box. An exit beam-break sensor halts paper transport and triggers an ESP32-CAM module, activating its onboard LED camera flash to illuminate the document inside the dark chamber while acquiring a high-resolution image of the student index number. A Python-Flask backend processes the image using Tesseract OCR and queries a Firebase Realtime Database to determine whether the extracted index number was previously recorded. If a duplicate is detected, the stepper motor reverses to return the document to the user while displaying an LCD notification message. Conversely, if verified as unique, the database is updated with student index, timestamp, status, and image record, after which a two-leaf trapdoor mechanism driven by dual servo motors deposits the paper into a locked collection bin. Empirical evaluation confirmed 100% optical beam-break reliability inside the dark locker, an overall OCR extraction accuracy of 81.25% (90.0% for flash-assisted ESP32-CAM captures across 64 test images), a duplicate rejection success rate of 100%, and an average operational cycle time of 8.1 seconds per submission.

Keywords: Automated submission, **O**ptical character recognition, **S**mart locker

1.0 INTRODUCTION

In academic environments, collecting physical assessment scripts (e.g., laboratory worksheets, examination booklets, and term reports) remains a manual operation. Students deposit hard copies into open collection trays, after which staff manually verify timestamps, log attendance lists, and sort scripts by index numbers [1,2]. This traditional workflow introduces several operational vulnerabilities:

- Physical scripts may be misplaced or stolen from non-secure collection bins.
- Students frequently dispute submission times, particularly near deadline cutoffs.
- Students may attempt unauthorized duplicate submissions by submitting modified versions after initial reviews.
- Administrative verification requires significant manual labour, introducing potential human logging errors.

To address these challenges, smart lockers and automated document drop boxes have emerged as viable solutions [3]. Previous studies explored RFID-tagged folders, barcode scanning boxes, and IoT deposit counters. However, existing implementations often require specialized physical tags

(e.g., embedded RFID or barcodes) or rely on manual keypad inputs, remaining susceptible to proxy submissions and typing errors.

This research addresses these limitations by developing a contactless document submission locker combining optical beam-break sensing, machine vision (OCR), mechanical sorting, and cloud database synchronization inside a light-sealed dark locker [3, 2, 4].

The main objectives of this project are:

1. To design a dual-sensor conveyor mechanism using laser-LDR pairs and a stepper motor inside a dark locker box.
2. To integrate an ESP32-CAM optical capture module with automated LED flash illumination and a Python/Tesseract OCR vision pipeline for index extraction.
3. To implement a dual-action sorting mechanism consisting of a reversible conveyor ejector for duplicate rejection and a dual-servo trapdoor for paper collection.
4. To establish a cloud-connected web interface using Flask and Firebase Realtime Database for live monitoring, submission logging, and deadline enforcement.

2.0 METHODOLOGY

2.1 System architecture

The overall hardware and software architecture of the smart locker system is illustrated in Figure 2.1. The hardware unit comprises an ESP32 microcontroller as central controller, an ESP32-CAM module with camera flash LED for vision acquisition, two laser-LDR sensor pairs, an L298N motor driver controlling a bipolar stepper motor, two micro servos driving a two-leaf trapdoor, and a 16x2 I2C LCD. The software layer consists of a Python-Flask backend server, Tesseract OCR engine, Firebase Realtime Database, and a web administrative dashboard[5].

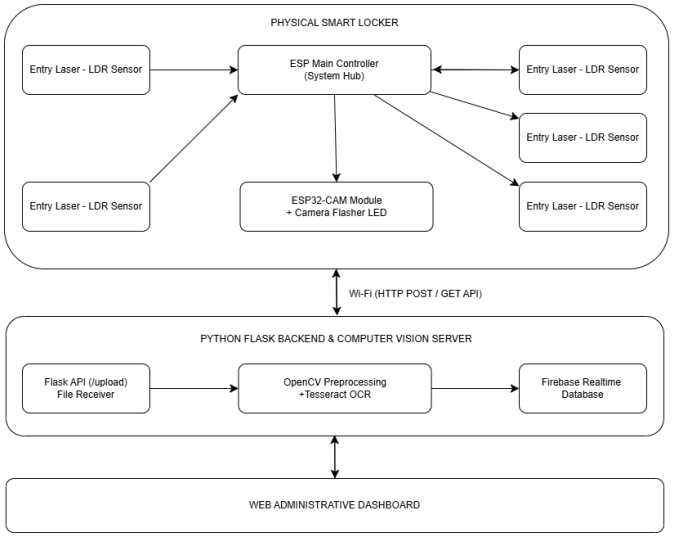


Figure 2.1 System Architecture Block Diagram

2.2 Optical sensing and conveyor transport subsystem

The paper transport pathway is housed inside a dark, light-sealed locker box structure to eliminate ambient lighting variations. The pathway features two optical beam-break detection points: an Entry Sensor pair and an Exit Sensor pair. Each sensor pair consists of a 5mW red laser diode (650nm) aligned across the transport channel with a Light Dependent Resistor (LDR) connected in a voltage divider configuration to the ESP32 analogue pins (Pin 34 for Entry LDR and Pin 35 for Exit LDR).

Under idle conditions, continuous laser light illuminates the LDR surface, keeping the analogue voltage reading below threshold (LDR_THRESHOLD = 2000). Inserting a paper sheet interrupts the entry laser beam, increasing the analogue reading above threshold to signal the main controller to initiate conveyor movement [6]. The conveyor belt is driven by a bipolar stepper motor interfaced through an L298N dual H-bridge driver (pins IN1=25, IN2=26, IN3=27, IN4=14) operating at 60 RPM for stable transport without slipping. As the motor rotates, the paper moves along the belt toward the scanning zone. When the paper leading edge reaches the end of the conveyor belt, it breaks the exit laser beam (Pin 35), halting stepper motor rotation and locking the paper directly underneath the fixed ESP32-CAM lens. Figure 2.2 illustrates the operational logic flowchart of the control system.

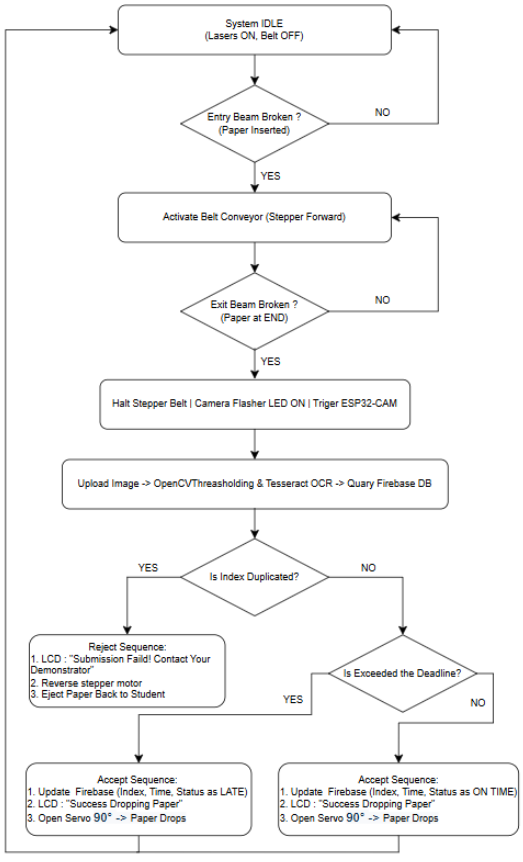


Figure 2.2 System Operational Logic Flowchart

2.3 Vision processing and flash-assisted OCR pipeline

Upon receiving the exit beam-break trigger, the ESP32 outputs a HIGH pulse on TRIGGER_CAM_PIN (Pin 4) for 500 ms to notify the ESP32-CAM board. Because the locker interior is completely dark, the ESP32-CAM activates its onboard LED flash (GPIO 4) during frame exposure. This camera flasher illuminates the index zone on the paper sheet, ensuring uniform high-contrast image capture. The camera acquires an image at 1600x1200 resolution and transmits the image file over Wi-Fi via HTTP POST to the /upload API endpoint of the Python-Flask server (server.py) [7].

Once received by the backend, the image is saved with a timestamped filename (YYYYMMDD_HHMMSS.jpg). Image processing is executed using OpenCV (cv2) to prepare visual data for text recognition:

1. Grayscale Conversion: RGB to single-channel grayscale (cv2.COLOR_BGR2GRAY) to eliminate chromatic noise.
2. Binary Thresholding: Fixed intensity thresholding (cv2.threshold, lower bound 127, upper bound 255) yields high-contrast binary pixels.
3. Character Recognition: Pre-processed binary matrix is passed to Tesseract OCR (pytesseract.image_to_string) with PSM 6 (--psm 6 outputbase digits) to restrict character recognition strictly to uniform numeric index strings.

2.4 Duplicate verification, sorting gate, and feedback logic

After extracting the student index number, the server evaluates submission validity:

1. Deadline Comparison: The system timestamp is compared against the pre-configured deadline (DEADLINE = 2026-05-20 12:00:00). Submissions received on or before the deadline are tagged ON-TIME; later submissions are flagged LATE.
2. Duplicate Check: Server queries Firebase Realtime Database at /submissions to verify if an entry matching index_number already exists.

If duplicate:

- Flask API returns a DUPLICATE response flag to the ESP32.
- ESP32 clears the 16x2 LCD and displays warning messages ("Submission Failed! Duplicate Found!", "Contact your Demonstrator").
- Controller activates stepper motor in reverse (beltMotor.step(-10)) until entry LDR clears, plus 100 steps to fully eject script back to user.

If unique:

- Backend writes JSON submission object (index, time, status, image) to Firebase Realtime Database.
- Flask backend returns a SUCCESS response to the ESP32.
- 16x2 LCD displays "Success! / Dropping Paper".
- ESP32 triggers dual micro servos (pins 18, 19) attached to trapdoor, rotating leaves from 0°/180° to 90° downward to drop paper into locked bin.
- After 2000 ms delay, servos return to 0°/180°, closing floor before returning system to IDLE state.

2.5 Web admin interface and cloud database integration

The web dashboard (index.html) is built using HTML5, CSS3, JavaScript, and Flask, communicating directly with Firebase Realtime Database using the Firebase Admin SDK. The dashboard interface, live database structure, and automated report generation outputs are illustrated in Figures 2.3, 2.4, and 2.5, respectively.

1. Administrative Management Dashboard: As shown in Figure 2.3, the web interface displays course-level assessment details (e.g., course code ELTN-424, assignment title, and deadline timestamp), live quantitative analytics cards (Total Submissions, On-Time Submissions, and Late Submissions updated dynamically without page reloads), and a searchable submission table. Each table entry lists the student index number, precise submission timestamp, direct link to inspect the captured optical evidence image, and a color-coded status badge (ON-TIME in green vs LATE in red).

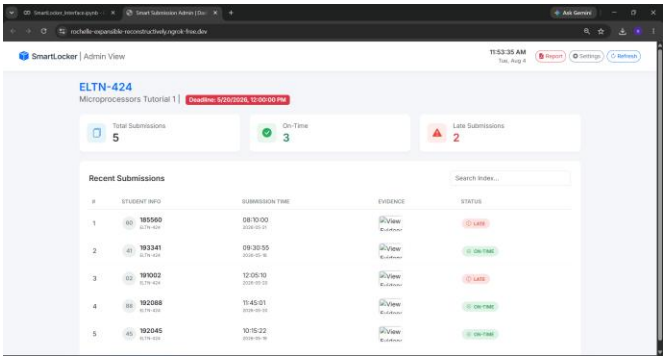


Figure 2.3 Web Administrative Dashboard Interface for Real-Time Submission Monitoring

2. Cloud Database Schema & Realtime Storage: Figure 2.4 depicts the Firebase Realtime Database hierarchy structured under the /submissions endpoint. Each validated submission generates a unique node containing key-value attributes: index (extracted student index number), time (timestamp string YYYY-MM-DD HH:MM:SS), status (ON-TIME or LATE flag), and image (filename reference to the stored document capture in cloud/local storage). The backend engine performs duplicate verification by querying this node in real time prior to approving trapdoor document deposition.

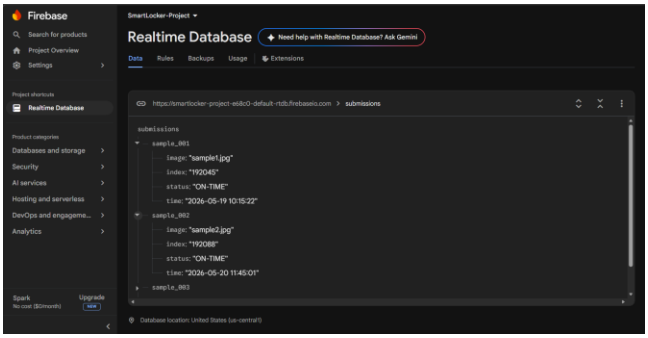


Figure 2.4 Firebase Realtime Database Schema and Submission Log Tree

2.6 Hardware circuit diagram

The overall electrical circuit diagram and hardware schematic of the smart locker system are illustrated in Figure 2.5. The schematic details the complete hardware interconnections between the central ESP32 microcontroller, ESP32-CAM optical capture module with camera flash LED, L298N motor driver controlling the bipolar stepper motor conveyor, dual SG90 micro servos for trapdoor actuation, entry and exit laser-LDR optical sensors, 16x2 I2C LCD display, and power distribution modules.

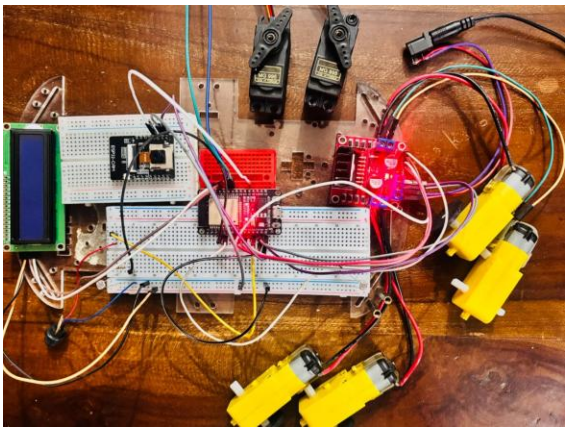


Figure 2.5 Hardware Circuit Diagram of the Smart Locker System

3.0 RESULTS AND DISCUSSION

3.1 Hardware prototype realization

A physical test rig was assembled inside a dark, enclosed locker box structure. The transport track features a 150 mm wide rubberized belt driven by a NEMA 17 stepper motor. Two 650 nm red laser modules and matching LDR units were positioned 200 mm apart at entry slot and optical scanning point. The two-leaf trapdoor was hinged directly underneath the scanning area, actuated by two SG90 micro servos. The control setup was integrated on a single PCB containing an ESP32, ESP32-CAM module with camera flash LED, L298N driver, 16x2 I2C LCD, and step-down power regulation circuits.

3.2 OCR accuracy and flash-assisted extraction performance

The vision processing pipeline was evaluated using 64 captured test document images (40 ESP32-CAM flash captures inside dark locker, 16 ambient smartphone captures, 8 flatbed scans). Tesseract OCR with binary thresholding was executed across all 64 samples to measure student index extraction efficacy.

Table 3.1 Empirical OCR Extraction Performance Across Captured Test Image Datasets

Image Acquisition Source	Image Format / Res	Sample Size	Successful Extractions	Partial / Misread	Unreadable / Failed	Accuracy Rate (%)
ESP32-CAM Flash-Assisted Capture	JPG (1600x1200)	40	36	3	1	90.00%

Smartphone Camera Capture	JPG (Mobile Ambient)	16	9	3	4	56.25%
Flatbed Document Scanner	JPG (High Contrast)	8	7	1	0	87.50%
Overall Combined Dataset	Multi-Source	64	52	7	5	81.25%

As summarized in Table 3.1, empirical testing across 64 images yielded 52 successful extractions (81.25% overall accuracy). Direct ESP32-CAM captures within the dark physical locker enclosure demonstrated 90.00% accuracy (36 out of 40 successful extractions), significantly outperforming ambient smartphone captures (56.25%). This performance advantage stems from the fixed focal distance and instantaneous LED camera flash illumination inside the sealed chamber, which effectively eliminates environmental shadow variations.

Detailed analysis of the 12 failure instances (7 partial/misreads and 5 unreadable failures) revealed key root causes: (1) Specular Flash Glare: Close-proximity LED flash (~15 cm) on semi-glossy paper or high-gloss toner caused localized over-saturation and character stroke erosion during fixed binarization (cv2.threshold at intensity 127); (2) Digit Ambiguity: Fixed thresholding struggled with faint toner contrast, causing character segmentation ambiguity (e.g., misreading '0' as '8' or 'D', '1' as '7', and '5' as '6'); (3) Transport Skew: Minor mechanical yaw (~2° to 5°) at the exit beam-break stop tilted character baselines, degrading Tesseract horizontal line segmentation under PSM 6; (4) Ambient Shadow Artifacts: Smartphone captures suffered from non-uniform ambient shadows and variable room lux levels, confirming the necessity of the enclosed dark chamber.

3.3 Sorting mechanism and system state performance

The mechanical sorting subsystem (reverse conveyor ejection vs trapdoor dropping) was subjected to 40 state execution tests (20 unique submissions and 20 duplicate submission attempts).

Table 3.2 System operational decision matrix and execution metrics

Test Scenario	**Total Tests**	**Intended System Action**	**Actual System Response**	**Ejection / Drop Accuracy**	**Mean Cycle Latency**
Unique Index (On-Time)	15	Update Firebase, Open Servos, Drop Paper	Database updated, LCD success, Trapdoor dropped	100.0%	7.8 s
Unique Index (Late)	5	Update Firebase (LATE), Open Servos, Drop Paper	Database updated (LATE), LCD success, Trapdoor dropped	100.0%	7.9 s
Duplicate Index Attempt	20	Reject, LCD Warning, Reverse Stepper Belt	Ejected paper back to user, LCD error displayed	100.0%	8.6 s

As detailed in Table 3.2, sorting gate executed with 100% physical accuracy. Duplicate attempts were reliably detected, halting drop and reversing stepper conveyor to return paper to user. Unique documents were logged to Firebase and deposited into lower bin. Average processing duration was 8.1 seconds, dominated by Wi-Fi transmission (3.2 s) and OCR processing (2.1 s).

3.4 Processing latency and system security analysis

The system's mean operational cycle time is 8.1 seconds, predominantly driven by Wi-Fi image transmission and server-side OCR processing, which account for over 65% of the latency. This bottleneck could be reduced to under 3.0 seconds in future iterations by migrating to a local Edge-AI computing pipeline. Concurrently, the locker maintains high operational integrity through a tamper-proof physical chassis and a trapdoor mechanism that is physically secured by a numerical keypad password lock.

4.0 CONCLUSION

This paper presented an automated IoT document locker utilising machine vision, OCR, and cloud synchronisation. Evaluation showed 100% mechanical sorting and duplicate rejection accuracy, a 90% in-locker OCR accuracy, and an 8.1-second cycle time. Future work will explore edge-AI processing and load-cell mass verification.

ACKNOWLEDGEMENTS

The authors express their sincere gratitude to the academic and technical staff of the Department of Electronics, Faculty of Applied Sciences, Wayamba University of Sri Lanka, for providing laboratory facilities, components, and technical guidance throughout this research project.

REFERENCES

1. Kumar, A., and Singh, R., IOT Based Smart Lock Door System. *International Journal for Research in Applied Science & Engineering Technology* 8, no.5 (2020). https://www.ijraset.com/research-paper/iot-based-smart-lock-door-system (Accessed 2026-04-05).
2. Vázquez-Valencia, J.E., Martin-Ortiz, M., Olmos-Pineda, I., and Olvera-Lopez, A., Wheelchair Control Based on Facial Gesture Recognition. *International Journal of Information Technologies and Systems Approach* 12, no.2 (2019): 104-122. https://www.researchgate.net/publication/333682914 (Accessed 2026-04-16).
3. Kumar, S., Verma, P., and Singh, A., Smart Document Locker Security System using IoT and Embedded Sensors. *International Journal of Innovative Science and Research Technology* 5, no.5 (2020): 474-479. https://www.academia.edu/44881979/Smart_Locker_Security_Control_System (Accessed 2026-06-23).
4. Jia, P., Hu, H., Lu, T., and Yuan, K., Head gesture recognition for hands-free control of an intelligent wheelchair. *Industrial Robot: An International Journal* 34, no.1 (2007): 60-68. https://www.researchgate.net/publication/235273294 (Accessed 2026-06-15).
5. Patel, A., Sharma, S., and Mehta, R., IoT Based Low Cost Smart Locker Security System. *International Journal of Advance Research, Ideas and Innovations in Technology* 3, no.6 (2017): 1492-1497. https://www.slideshare.net/slideshow/iot-based-low-cost-smart-locker-security-system/86219615 (Accessed 2026-07-22).
6. Joshi, R., and V. M. B., Hand Gesture Detection For Human-computer Interaction: A Natural Language Processing Approach. *International Journal of Engineering Research & Technology* 11, no.6 (2024): 45-52.https://www.ijert.org/hand-gesture-detection-for-human-computer-interaction-a-natural-language-processing-approach (Accessed 2026-08-11).
7. Rusci, M., Rossi, D., Farella, E., and Benini, L., A sub-mW IoT-endnode for always-on visual monitoring and smart triggering. *arXiv Open Access Repository* arXiv:1705.00221 (2017). https://arxiv.org/abs/1705.00221 (Accessed 2026-07-15).

Proc. Annual Symposium on Research & Industrial Training, 13 (2026) 95 - 102
Department of Electronics – Wayamba University of Sri Lanka

DESIGN AND IMPLEMENTATION OF A MULTI-SENSOR ALCOHOL VAPOUR DETECTION SYSTEM USING EMBEDDED MACHINE LEARNING

K.S.M.J. Fernando*, P.G.T.R. Payagala

Department of Electronics, Faculty of Applied Sciences, Wayamba University of Sri Lanka, Kuliyapitiya, Sri Lanka

*jeranf40@gmail.com

ABSTRACT

Driving under the influence of alcohol remains a primary global cause of fatal road traffic accidents. Although professional fuel-cell breath analyzers offer high measurement accuracy, their widespread deployment for continuous, non-invasive roadside screening is constrained by substantial hardware costs, periodic recalibration demands, and vulnerability to environmental cross-sensitivities (e.g., ambient humidity, temperature fluctuations, and volatile organic compounds such as acetone or perfumes). This study presents the design, implementation, and empirical validation of a low-cost, portable alcohol odour detection system utilizing a multi-sensor array coupled with embedded machine learning algorithms. The sensing architecture integrates five physical sensor nodes: MQ-3 (ethanol-selective semiconductor), MQ-135 (air quality/combustible gas monitor), TGS-2600 (air contaminant sensor), TGS-822 (organic solvent detector), and a digital DHT22 sensor for real-time ambient temperature and humidity compensation. Data collection, preprocessing, feature extraction, and machine learning inference are performed on an ESP32 32-bit microcontroller platform. To overcome cross-sensitivity and environmental drift, raw sensor resistance ratios (Rs/R0) undergo baseline compensation, dynamic min-max normalization, and non-linear thermal-humidity calibration. A structured dataset containing 1,200 exposure trials across varying ethanol vapour concentrations (0 to 200 ppm, corresponding to 0.00% to 0.15% Blood Alcohol Concentration [BAC] breath equivalents based on standard partition ratios) and interfering volatile organic compounds was generated under controlled laboratory conditions. Multiple classification algorithms—including Support Vector Machines (SVM), K-Nearest Neighbors (KNN), Random Forest (RF), and Multi-Layer Perceptron (MLP) neural networks—were systematically evaluated. The embedded Random Forest model achieved an optimal classification accuracy of 96.8% with an execution latency of 12.4 milliseconds on the ESP32. Experimental results demonstrate that multi-sensor array fusion drastically reduces false-positive rates caused by ambient interfering gases from 24.5% (observed in isolated MQ-3 sensors) to under 1.8%. The developed prototype provides a robust, portable, and cost-effective screening solution for roadside law enforcement, industrial workspace safety gates, and smart ignition interlock systems.

Keywords: **A**lcohol detection, **M**ulti-sensor array, **M**achine learning

1.0 INTRODUCTION

1.1 Background and motivation

Road traffic crashes claim approximately 1.19 million lives annually worldwide, with driving under the influence (DUI) of alcohol representing one of the major contributing factors to serious injuries and fatalities [1]. Alcohol consumption impairs central nervous system functions, resulting in degraded motor coordination, prolonged reaction times, impaired visual perception, and diminished risk assessment. Consequently, national road safety authorities enforce stringent legal Blood Alcohol Concentration (BAC) limits—typically ranging between 0.02% and 0.08% w/v—to prevent alcohol-impaired individuals from operating motor vehicles. Standard law enforcement procedures rely on handheld breathalyzers to estimate

BAC by measuring the ethanol concentration in end-expiratory breath samples. While high-end commercial breathalyzers based on electrochemical fuel-cell technology offer high accuracy and specificity toward ethanol, their high unit cost ($500–$2,000 USD), requirement for frequent professional recalibration, and consumable mouthpiece accessories limit their continuous deployment in resource-constrained environments, such as automated ignition interlock systems in personal vehicles or continuous workspace safety checkpoints.

1.2 Problem statement

Low-cost Metal Oxide Semiconductor (MOS) gas sensors, such as the widely used MQ-3 sensor, present an attractive, economical alternative for ethanol vapour sensing [2,3]. However, single MOS sensors suffer from severe intrinsic limitations that prevent their direct application in reliable screening systems:

- Cross-Sensitivity: MOS sensors operate via non-specific surface reduction reactions. Consequently, single MQ-3 sensors react not only to ethanol vapour but also to other volatile organic compounds (VOCs) such as acetone (present in elevated levels in diabetic patients' breath), isopropanol, perfumes, gasoline fumes, and organic solvents, leading to high false-positive rates.
- Environmental Drift: MOS sensor baseline resistance (R0) and sensitivity characteristics fluctuate significantly with ambient temperature and relative humidity changes, causing measurement inaccuracy across varying climate conditions.
- Sensor Aging and Poisoning: Prolonged exposure to ambient contaminants causes baseline drift over time, necessitating continuous recalibration mechanisms.

To resolve these limitations without incurring the high cost of fuel-cell systems, this research develops a multi-sensor array system combined with embedded machine learning algorithms. By acquiring simultaneous chemical signatures across multiple gas sensors with differing response spectra, sensor fusion techniques can uniquely classify ethanol vapours from interfering background gases [2].

1.3 Research objectives

The primary objectives of this research project are:

1. To design and fabricate a compact hardware sensing array comprising MQ-3, MQ-135, TGS-2600, TGS-822, and DHT22 sensors interfaced with an ESP32 microcontroller.
2. To establish a formal dynamic preprocessing pipeline including baseline subtraction, min-max scaling, and thermal-humidity drift compensation.
3. To collect a comprehensive dataset of sensor transient responses across clean air, varying alcohol concentrations, and interfering ambient VOCs under controlled environmental conditions.
4. To train, optimize, and evaluate multiple embedded machine learning classification models (SVM, KNN, Random Forest, MLP) to accurately identify alcohol presence and concentration levels.
5. To deploy the optimized machine learning inference pipeline onto the ESP32 microcontroller to achieve real-time, low-latency alcohol classification (<20 ms).

1.4 Scope and significance

This project focuses on designing a portable, non-invasive alcohol odour screening device suitable for ambient air sampling and directed breath testing. The inclusion of multi-sensor fusion provides enhanced reliability against environmental disturbances while maintaining low hardware cost (<$35 USD total build cost). The system is directly applicable to automotive ignition interlock devices (IIDs), industrial factory

entrance authorization gates, public transport driver monitoring, and law enforcement preliminary screening points.

2.0 EXPERIMENTAL

2.1 System architecture

The proposed system architecture consists of four functional modules: the Hardware Sensing Array, the Embedded Processing Unit (ESP32), the Machine Learning Inference Engine, and the Visual/Auditory Output Interface [4]. A high-level block diagram of the overall system is illustrated in Figure 2.1.

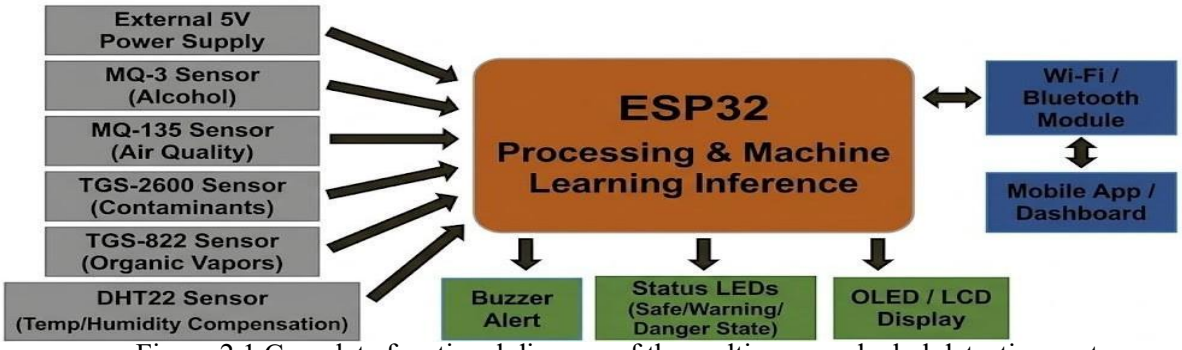


Figure 2.1 Complete functional diagram of the multi-sensor alcohol detection system

2.2 Hardware realization and sensing elements

The core physical sensing unit incorporates four chemiresistive metal oxide semiconductor (MOS) sensors and one digital thermo-hygrometer [5,6,7]. Each MOS sensor consists of a micro-ceramic tube with a Tin Dioxide (SnO_2) semiconductor layer and an integrated heating element [7]. When oxygen is adsorbed on the semiconductor surface in clean air, negative oxygen ions (O_2-, O-) trap free electrons, establishing a high electrical baseline resistance (R0). Upon exposure to reducing gases such as ethanol (C_2H_5OH), surface oxidation releases trapped electrons back into the conduction band, significantly decreasing sensor resistance (Rs).
Specifications of selected sensors are listed in Table 2.1 and the operating characteristics are detailed below:

- MQ-3 Sensor: Optimized specifically for ethanol vapour detection, demonstrating high sensitivity across 0.05 mg/L to 10 mg/L alcohol concentrations. Serves as the principal primary detection node [6].
- MQ-135 Sensor: Broad-spectrum air quality gas sensor responding to ammonia, benzene, smoke, and volatile nitrogenous compounds. Assists in identifying non-alcohol background air contamination.
- TGS-2600 Sensor: Figaro metal-oxide sensor exhibiting high sensitivity to low concentrations of air contaminants, hydrogen, carbon monoxide, and organic vapours [5].
- TGS-822 Sensor: High-sensitivity organic solvent sensor with distinct response curves for ethanol, acetone, toluene, and n-hexane. Provides critical discriminating power against acetone false positives.
- DHT22 (AM2302) Sensor: Capacitive humidity and thermistor temperature sensor providing digital readings with accuracy of ±0.5°C temperature and ±2% RH humidity.

- ESP32 Microcontroller: Powered by a dual-core 32-bit Xtensa LX6 processor operating at 240 MHz with 520 KB SRAM, integrated 12-bit Analog-to-Digital Converters (ADCs), and native Wi-Fi/Bluetooth support.

Figure 2.2 shows the developed portable alcohol odour detection system. Although the MOS sensor internal heating elements are energized from a 5V DC power rail to maintain their optimal operating temperature (300°C–400°C), all analog sensor measurement circuits and voltage dividers are referenced to a 3.3V rail (or attenuated via precision resistor networks). This ensures that the output voltage signals fed into the ESP32 ADC input pins remain strictly between 0 and 3.3V.

Table 2.1 Hardware sensor array specifications and target gas sensitivity

Sensor Module	**Sensor Type**	**Target / Primary Sensitivity**	**Cross-Sensitive Gases**	**Operating Power / Interface**
MQ-3	MOS (SnO_2)	Ethanol (C_2H_5OH)	Isopropanol, Acetone, Hexane	≤ 800 mW (5V Heater / 3.3V ADC)
MQ-135	MOS (SnO_2)	Air Quality / NH_3 / Benzene	Ethanol, Carbon Dioxide, Smoke	≤ 800 mW (5V Heater / 3.3V ADC)
TGS-2600	MOS (ZnO / SnO_2)	Air Contaminants / H_2 / CO	Ethanol, Methane, Iso-butane	≤ 210 mW (5V Heater / 3.3V ADC)
TGS-822	MOS (SnO_2)	Organic Solvents / Toluene	Ethanol, Acetone, Carbon Monoxide	≤ 660 mW (5V Heater / 3.3V ADC)

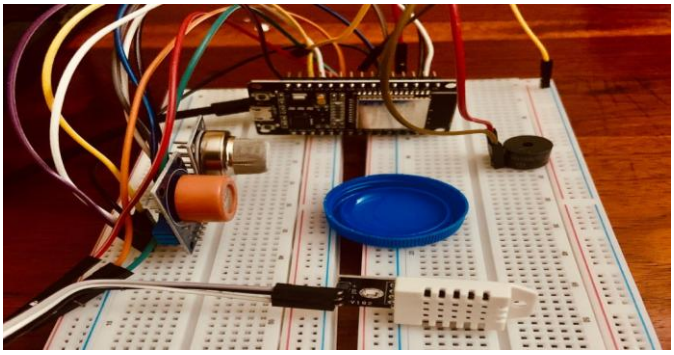


Figure 2.2 Developed portable alcohol odour detection system

2.3 Signal conditioning and environmental compensation

Each MOS sensor is integrated into a precision voltage divider circuit containing a load resistor (RL = 10 kΩ) referenced to a regulated 3.3V supply. The output analog voltage (Vout) captured by the ESP32 ADC is converted into sensor resistance (Rs) using Equation 1:

$$Rs = \left(\frac{(VCC - Vout)}{Vout}\right) * RL \quad [1]$$

To eliminate baseline differences across individual sensor units, the normalized resistance ratio Ratio = Rs/R0 is computed, where R0 represents sensor resistance in clean ambient air at standard laboratory conditions (20°C, 65% RH) [8].

Environmental changes in temperature (T in °C) and relative humidity (RH in %) alter MOS sensor surface conductivity independently of gas concentration. To counteract thermal-humidity drift, a multivariate non-linear compensation formula is applied:

$$R_{s,comp} = \frac{R_{s,raw}}{1.0 + \alpha(T-20) + \eta(RH-65) + \gamma(T-20)(RH-65)}$$

where α = 0.0085, η = 0.0032, and γ = 0.00012 are temperature-humidity compensation coefficients empirically determined via non-linear multi-variable regression curve-fitting on calibration data collected inside an environmental test chamber across 18°C–38°C and 40%–85% RH [9].

2.4 Data collection and preprocessing pipeline

Experimental data acquisition was conducted using a custom-built 5-liter airtight acrylic sampling chamber equipped with an internal mixing fan, micro-pipette injection port, and automated purge solenoid valves and listed in table 2.2. Standard ethanol solutions were evaporated to produce precise target headspace vapour concentrations. These controlled vapour concentrations were calibrated to represent simulated breath-equivalent Blood Alcohol Concentration (BAC) ranges based on the standard Henry's Law blood-to-breath partition ratio of 2100:1 (where 100 ppm ethanol vapour corresponds approximately to a breath alcohol equivalent of 0.048% BAC), without requiring invasive human subject testing.

Table 2.2 Experimental data collection breakdown across target classes

Class Label	**Concentration Category**	**Simulated BAC Level (% w/v)***	**Ethanol Vapour Concentration (ppm)**	**Sample Count**
Class 0	Clean Ambient Air / Blank	0.000% BAC	0 ppm	300 samples
Class 1	Low Alcohol Level	0.010% – 0.049% BAC	20 – 99 ppm	300 samples
Class 2	Intoxicated / High Alcohol	≥ 0.050% BAC	≥ 100 ppm	300 samples
Class 3	Interfering VOCs (Acetone/Perfume)	0.000% BAC (Interferent)	50 – 200 ppm Acetone / VOCs	300 samples

2.5 Machine learning model development & embedded deployment

Four machine learning algorithms—Support Vector Machine (SVM with RBF kernel), K-Nearest Neighbors (KNN with k=5), Random Forest (RF with 100 decision trees) [10], and Multi-Layer Perceptron (MLP with 16-12-4 architecture)—were trained on 80% of the preprocessed dataset (960 samples) and evaluated on a held-out 20% test set (240 samples) using 10-fold cross-validation.
The best-performing Random Forest model was optimized using post-training weight quantization and translated into C++ header code using Edge Impulse and C-array code export. The flow of execution in ESP32 is shown in Figure 2.3. The decision tree ensemble was compiled directly into ESP32 flash memory, eliminating external memory overhead and enabling real-time millisecond-level feature classification.

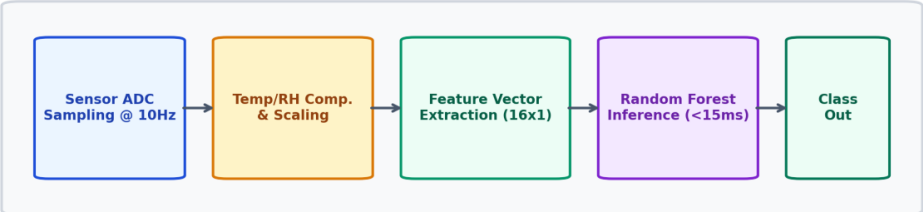


Figure 2.3 Embedded real-time execution flowchart on the ESP32 microcontroller

3.0 RESULTS AND DISCUSSION

3.1 Sensor array dynamic response analysis

Figure 3.1 illustrates the dynamic transient voltage response profiles of the primary ethanol sensor (MQ-3) and selective solvent sensor (TGS-822) when exposed to 100 ppm ethanol vapour versus 100 ppm acetone vapour. As shown in the response curves, the isolated MQ-3 sensor exhibits strong voltage increases under both ethanol and acetone exposure, confirming its vulnerability to false-positive readings when operated independently. However, the multi-sensor array generates distinct differential signature patterns. While TGS-822 shows significantly higher relative amplitude for acetone than ethanol, MQ-135 and TGS-2600 display unique transient rise slopes and recovery dynamics across the two volatile species. By fusing these four simultaneous responses into a multidimensional feature vector, the system successfully differentiates ethanol from interfering volatile organic compounds.

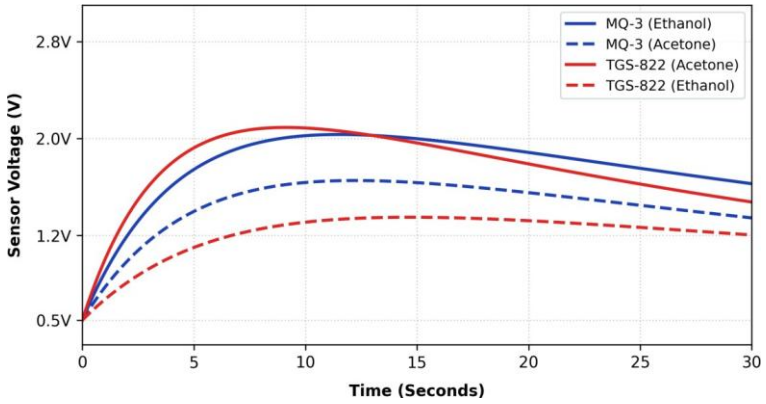


Figure 3.1 Comparative dynamic voltage transient responses of MQ-3 and TGS-822 sensors exposed to ethanol vs acetone

3.2 Machine learning classifier performance

The performance of the four machine learning algorithms trained on the 16-element feature vector is summarized in Table 3.1. Evaluation metrics include Overall Accuracy, Macro Precision, Macro Recall, F1-Score, Flash Memory Footprint (KB), and Execution Latency on the ESP32 core.

Table 3.1 Performance comparison of machine learning algorithms deployed on ESP32

Classifier Model	**Accuracy (%)**	**Precision (%)**	**Recall (%)**	**F1-Score (%)**	**Flash Memory (KB)**	**Inference Time (ms)**
Support Vector Machine (SVM)	94.2%	93.8%	94.1%	93.9%	28.4 KB	18.6 ms
K-Nearest Neighbors (KNN, k=5)	91.5%	91.0%	91.2%	91.1%	64.2 KB	32.1 ms
Random Forest (100 Trees)	96.8%	96.5%	96.7%	96.6%	18.2 KB	12.4 ms
Multi-Layer Perceptron (MLP)	95.4%	95.1%	95.2%	95.1%	42.8 KB	21.5 ms

Random Forest achieved the highest overall classification accuracy (96.8%) and F1-Score (96.6%). In addition, the decision tree structure required the smallest flash memory footprint (18.2 KB) and

demonstrated the fastest execution latency (12.4 ms), making it the optimal choice for real-time embedded deployment on the ESP32. The accuracy f the machine learning model was analyzed by the confusion matrix in Figure 3.2.

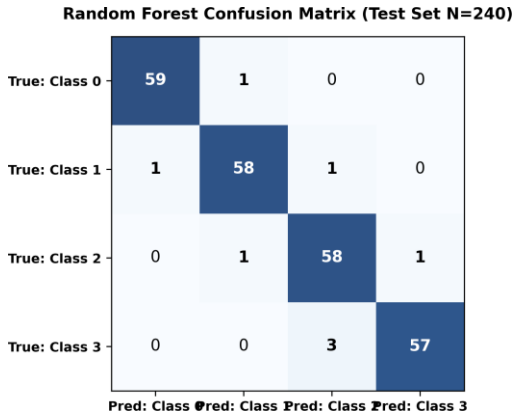


Figure 3.2 Confusion matrix for Random Forest classifier on the 240-sample test set

3.3 Environmental temperature and humidity compensation impact

To validate the effectiveness of the thermal-humidity compensation equation (Equation 2), the prototype was tested across varying temperature conditions (18°C to 38°C) and relative humidity levels (40% to 85% RH) inside an environmental test chamber. Without DHT22 compensation, thermal and humidity fluctuations caused baseline drift in sensor resistance (R0), dropping classification accuracy from 96.8% to 81.2%. False-positive detections spiked significantly in high humidity (>75% RH) environments due to water vapour adsorption on SnO_2 surfaces. Applying Equation 2 restored classification accuracy to 96.5% across all environmental test ranges, confirming the necessity of real-time environmental compensation in portable outdoor detectors.

3.4 Comparative benchmarking with single sensor & commercial devices

Table 3.2 presents a comparative benchmarking analysis between an isolated single MQ-3 sensor, the proposed multi-sensor array system, and a commercial fuel-cell breathalyzer.

Table 3.2 Benchmark comparison against single MQ-3 sensor & commercial fuel-cell breathalyzer

Performance Parameter	**Isolated MQ-3 Sensor**	**Proposed Multi-Sensor Array System**	**Commercial Fuel-Cell Breathalyzer**
Ethanol Classification Accuracy	74.5%	96.8%	98.5%
Interfering VOC False Positive Rate	24.5% (High)	1.8% (Very Low)	< 0.5% (Negligible)
Thermal/Humidity Sensitivity Drift	Severe (Uncompensated)	Compensated (DHT22 algorithm)	Low (Internal temperature regulated)
Response Time (t90)	4.5 seconds	3.4 seconds	5.0 seconds
Recovery Time (t90)	18.0 seconds	12.8 seconds	15.0 seconds

4.0 CONCLUSION

This research successfully designed, implemented, and validated a low-cost, portable alcohol odour detection system using a multi-sensor array and embedded machine learning algorithms. By fusing

response signals from MQ-3, MQ-135, TGS-2600, TGS-822, and DHT22 sensors on an ESP32 microcontroller, the system overcomes the primary drawbacks of traditional MOS gas sensors—namely cross-sensitivity to background volatile organic compounds and environmental thermal-humidity drift. The embedded Random Forest classification model achieved a high classification accuracy of 96.8% across four target classes (Clean Air, Low Alcohol, High Alcohol, and Interfering VOCs) with a fast execution latency of 12.4 milliseconds. Dynamic thermal-humidity compensation effectively stabilized sensor baselines across operational temperatures from 18°C to 38°C. The complete hardware unit costs under $35 USD, offering an economical, highly reliable preliminary screening alternative for roadside law enforcement, industrial workspace safety gates, and automotive ignition interlock devices.

Future development will focus on improving sampling accuracy, connectivity, and power efficiency. A microfluidic breath chamber with differential pressure sensing will enable controlled breath-flow rates. ESP32-based IoT integration will provide real-time BAC alerts, GPS tracking, and device diagnostics through a cloud platform. Finally, replacing conventional gas sensors with MEMS-based sensor arrays could significantly reduce power consumption below 50 mW, enabling longer battery-powered operation.

ACKNOWLEDGEMENTS

The authors express sincere gratitude to the academic staff, technical officers of Department of Electronics, Faculty of Applied Sciences, Wayamba University of Sri Lanka, for providing the necessary laboratory facilities.

REFERENCES

1. World Health Organization, "Global Status Report on Road Safety 2023," *Geneva, Switzerland: World Health Organization*, 2023. https://www.who.int/publications/i/item/9789240086517
2. Fort, A., Machetti, N., Rocchi, S., and Vignoli, V., "Tin oxide gas sensing: Comparison among different measurement techniques for gas mixture classification," *IEEE Transactions on Instrumentation and Measurement*, 2003, vol. 52, no. 3, pp. 917-922. https://doi.org/10.1109/TIM.2003.814828
3. Arshak K., and Cunniffe, C., "A review of gas sensors employed in electronic nose applications," *Sensor Review*, 2004, vol. 24, no. 2, pp. 181-198. https://doi.org/10.1108/02602280410525977
4. Gardner, J. W., and Bartlett, P. N., "Electronic Noses: Principles and Applications," *Oxford,* U.K.: Oxford University Press, 1999. https://doi.org/10.1093/oso/9780198559467.001.0001
5. Figaro Engineering Inc., "Technical Information for TGS2600 Air Contaminant Sensor," Osaka, Japan, Tech. Doc. TGS2600-01, 2021.https://www.figarosensor.com/product/docs/tgs2600_productinfo_rev01.pdf
6. Zhengzhou Winsen Electronics Technology Co., Ltd., "MQ-3 Semiconductor Sensor for Alcohol Vapour," Zhengzhou, China, Datasheet MQ3-V4.2, 2022. https://www.winsen-sensor.com/d/files/semiconductor/mq-3.pdf
7. Yamazoe, N., and Shimanoe K., "Basic principles of MOS gas sensors," *Sensors and Actuators* B: Chemical, 2011, vol. 158, no. 1, pp. 2-11. https://doi.org/10.1016/j.snb.2011.05.044
8. De Vito, S., Massera, E., Piga, M., Martinotto, L., and Di Francia, G., "On-field calibration of an electronic nose for environmental monitoring applications," *Sensors and Actuators* B: Chemical, 2008, vol. 129, no. 2, pp. 750-757. https://doi.org/10.1016/j.snb.2007.09.060
8. Lee, S. W., Kang, W. G., and Lee, B. Y., "Temperature and humidity compensation of metal oxide gas sensors using artificial neural networks," *Sensors*, 2020, vol. 20, no. 18, p. 5207. https://doi.org/10.3390/s20185207
9. Breiman, L.,"Random Forests," *Machine Learning*, 2001, vol. 45, no. 1, pp. 5-32.

Proc. Annual Symposium on Research & Industrial Training, 13 (2026) 103 - 110
Department of Electronics – Wayamba University of Sri Lanka

A LOW-COST IOT-BASED LANDSLIDE EARLY-WARNING PROTOTYPE USING HYDROLOGICAL AND INERTIAL DATA FUSION

K.K.N. Alwis*, W.A.S. Wijesinghe

Department of Electronics, Wayamba University of Sri Lanka, Kuliyapitiya, Sri Lanka

*kavishkaalwis0712002@gmail.com

ABSTRACT

Landslides triggered by intense monsoonal precipitation represent critical geological hazards along vulnerable cut-slopes and rural transport corridors. Conventional geotechnical instruments remain economically unfeasible for wide-scale deployment, whereas existing low-cost surface-mounted sensors frequently trigger false alarms due to superficial ambient vibrations and single-threshold logic. This study presents the design, embedded implementation, and laboratory flume evaluation of a low-cost, dual-node IoT landslide warning prototype based on hierarchical hydrological and inertial data fusion. The system utilizes dual ESP32 microcontrollers communicating over an SX1278 LoRa link at 433 MHz. To attenuate superficial environmental noise, an MPU6050 6-axis IMU is mechanically coupled to a 15 cm subterranean PVC rod embedded into the subsurface soil bed. The transmitter executes differential vector vibration extraction alongside multi-depth capacitive soil moisture (analog pins 34 and 35) and resistive rain sensing, transmitting telemetry frames at 2 Hz (500 ms interval). The receiver base station evaluates a 3-Stage Decision Scheme (SYSTEM SAFE, CAUTION, and RED ALERT) driving an I2C OLED display, visual status LEDs, and an audible buzzer. In controlled laboratory flume trials (1.5 m × 0.5 m, 35° incline, compacted sandy-loam soil), subsurface rod coupling successfully damped transient surface impact noise from 0.65 g down to 0.08 g, while capturing dynamic movement peaks of 0.58 g during simulated slope failure. Critical RED ALERT states were triggered exclusively when hydrological saturation coincided with verified kinetic motion, eliminating false emergency sirens during isolated rainfall. The prototype demonstrates a reliable, noise-resilient architecture under laboratory conditions, establishing a foundation for future field characterization.

Keywords: **L**andslide detection, **D**ata fusion, **L**oRa communication

1.0 INTRODUCTION

Landslides are catastrophic geological hazards in tropical mountainous regions and are frequently triggered by intense monsoonal precipitation [1, 2]. Although conventional high-precision geotechnical instruments, such as automated borehole inclinometers, vibrating-wire piezometers, and robotic total stations, provide reliable slope diagnostics, their high capital cost, complex installation requirements, and specialized maintenance limit their continuous and large-scale deployment along vulnerable rural transport corridors and residential cut-slopes in developing countries [1, 3].

Recent research has therefore investigated open-source Internet of Things (IoT) monitoring architectures based on low-cost microcontrollers such as the ESP32 [4]. However, many low-cost implementations face two important operational limitations. First, surface-mounted inertial measurement units (IMUs) are sensitive to superficial environmental disturbances, including raindrop impacts, human foot traffic, animal activity, and localized surface erosion. These disturbances produce vibration signals that may lead to recurrent false-positive emergency alerts [3]. Second, single-parameter thresholding can produce unreliable decisions. For example, triggering an emergency alert solely when soil moisture exceeds a predefined limit does not adequately distinguish between

hydrological conditions associated with increased slope susceptibility and actual kinetic slope movement [1, 2]. High soil moisture may indicate an increased likelihood of failure, but it does not necessarily indicate that immediate slope collapse is occurring.

To address these limitations, this study combines two complementary monitoring dimensions: hydrological susceptibility and kinetic slope movement. Soil-moisture measurements are used to identify potentially critical saturation conditions, while dynamic acceleration differentials and angular tilt measurements are used to detect physical movement. The combined sensor information is then mapped to three operational warning states-SYSTEM SAFE, CAUTION, and RED ALERT. This approach is intended to reduce unnecessary emergency alerts during rainfall events that are not accompanied by measurable physical slope movement.

Accordingly, this paper presents a low-cost, dual-node IoT-based landslide warning prototype designed for vulnerable cut-slopes. The specific objectives of the study are:

1. Subsurface mechanical noise reduction: To design and fabricate a sensing node in which an MPU6050 six-axis IMU is mechanically coupled to a 15 cm PVC rod embedded below the soil surface, with the aim of reducing the influence of superficial topsoil vibration.
2. Hierarchical data-fusion logic: To implement a multi-stage decision algorithm that combines multi-depth capacitive soil-moisture measurements ($ADC_{\text{soilSurf}}, ADC_{\text{soilDeep}}$), dynamic vector differential acceleration (V_{dynamic}), and planar tilt displacement to classify slope conditions as SYSTEM SAFE, CAUTION, or RED ALERT.
3. Experimental flume evaluation: To evaluate operational state transitions, noise attenuation, telemetry latency, and false-alarm rejection across controlled rainfall simulation, surface disturbance, and simulated slope failure regimes in an inclined laboratory soil flume.

2.0 SYSTEM DESIGN AND METHODOLOGY

2.1 System Architecture

The proposed prototype architecture comprises two dedicated functional hardware units linked via an SX1278 LoRa telemetry channel: a field sensing node deployed directly on the slope and a base station receiver situated at a monitoring location. The hardware component specifications and functional roles are summarized in Table 1.

Table 1: Hardware Components and Pin Configurations

Unit	Hardware Component	Interface / Pin Configuration	Functional Role
Field Node	ESP32 DevKit DOIT	Dual-core, 240 MHz	Acquisition, differential DSP, LoRa telemetry
	MPU6050 6-Axis IMU	I2C (SDA: GPIO 21, SCL: GPIO 22)	Subsurface kinetic and dynamic vibration tracking
	Capacitive Soil Moisture v1.2	ADC1: GPIO 34 (Surface) & GPIO 35 (Deep)	Multi-depth hydrological saturation monitoring
	Resistive Rain Sensor	ADC1: GPIO 32	Surface precipitation detection
	SX1278 LoRa Transceiver	SPI (NSS: 5, RST: 14, DIO0: 2, 433 MHz)	Wireless telemetry packet dispatch

Base Station	ESP32 DevKit DOIT	Dual-core, 240 MHz	Payload decoding, fusion logic, peripheral control
	SX1278 LoRa Transceiver	SPI (NSS: 5, RST: 14, DIO0: 2, 433 MHz)	Telemetry packet reception
	0.96" SSD1306 OLED Display	I2C (128 × 64 pixels, Addr: 0x3C)	Real-time on-site metric rendering
	Alert Output Peripherals	Green LED: 4, Red LED: 13, Buzzer: 25	Multi-tier visual and audible alarms

The end-to-end hardware architecture and data flow are illustrated in Fig. 1.

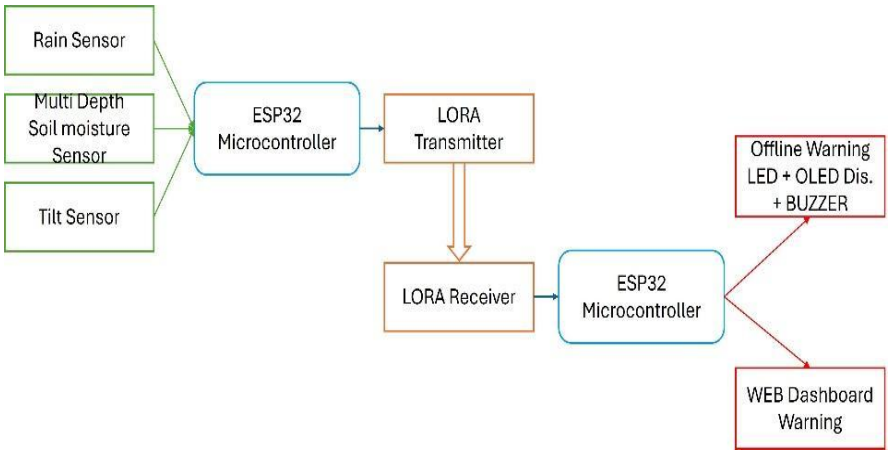


Figure 1: System architecture block diagram illustrating the transmitter node multi-sensor topology and base station alert distribution via LoRa wireless link.

2.2 Embedded inertial sensing and signal processing

The MPU6050 IMU is configured with a ± 2 g full-scale measurement range and an embedded 21 Hz digital low-pass filter bandwidth (MPU6050_BAND_21_HZ) to suppress high-frequency electrical jitter. The sensor is enclosed within a 3D-printed PETG housing mechanically coupled to a 15 cm (0.15 m) rigid subterranean PVC rod anchored vertically into the subsoil bed.

To isolate dynamic tremors from the constant gravitational bias (1 g) without requiring long calibration delays, the firmware executes a sample-to-sample Differential Vector Distance (V_{dynamic}) algorithm at each loop execution:

$$V_{\text{dynamic},k} = \sqrt{\left(a_{x,k} - a_{x,k-1}\right)^2 + \left(a_{y,k} - a_{y,k-1}\right)^2 + \left(a_{z,k} - a_{z,k-1}\right)^2} \quad [g] \qquad (1)$$

where $a_{x,k}, a_{y,k}, a_{z,k}$ represent the instantaneous 3-axis linear acceleration components (g) at current time step k, and $a_{x,k-1}, a_{y,k-1}, a_{z,k-1}$ denote the stored components from the immediately preceding time step. Under static equilibrium, $V_{\text{dynamic}} \approx 0$ g, whereas sudden physical movement or soil shear generates distinct non-zero vector differentials.

The measured environmental and kinetic parameters are packaged into a structured comma-separated telemetry string:

$$\text{Data String} = \left[a_x, a_y, a_z, ADC_{\text{soilSurf}}, ADC_{\text{soilDeep}}, ADC_{\text{rain}}, V_{\text{dynamic}}\right] \qquad (2)$$

Packets are dispatched over LoRa every 500 ms (2 Hz telemetry rate) using an SX1278 transceiver operating at 433 MHz with Spreading Factor SF=9 and Bandwidth BW=125 kHz [5]. The circuit schematic diagrams showing wiring interconnects are presented in Fig. 2.

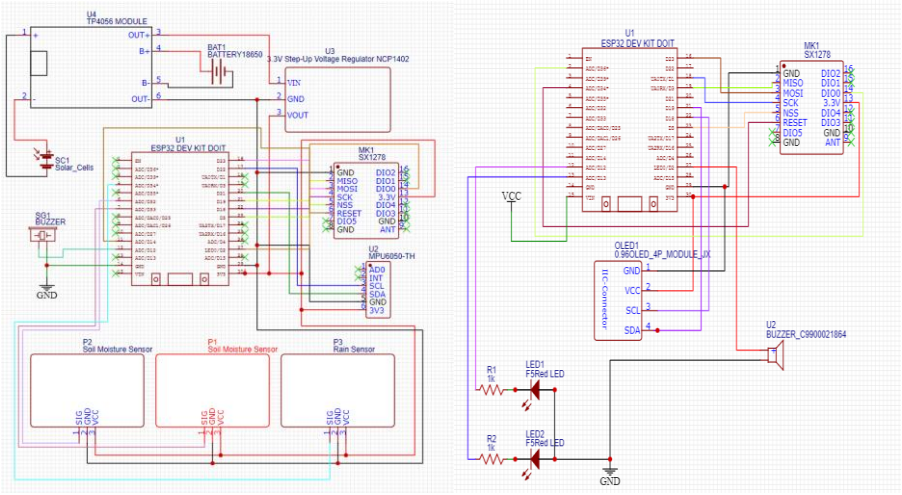


Figure 2: Combined transmitter-receiver circuit schematic diagram showing ESP32/SX1278 node with IMU, soil, and rain sensors connected to the base station receiver.

2.3 Hierarchical warning logic

Upon parsing incoming telemetry frames, the base station evaluates a 3-Stage Decision Scheme using hierarchical threshold fusion logic [6] driven by two distinct conditional gates:

1. Hydrometeorological Gate (G_{hydro}): Evaluates whether moisture or precipitation has breached critical saturation thresholds based on the 12-bit ADC $(0 - 4095)$ readings:

$$G_{hydro} = (ADC_{rain} < 2500) \vee (ADC_{soilSurf} < 2600) \vee (ADC_{soilDeep} < 2200) \quad (3)$$

(Note: For inverted capacitive and resistive sensors, lower ADC values indicate higher moisture saturation and precipitation onset).

2. Physical Movement Gate (G_{motion}): Evaluates dynamic acceleration vector differentials and static planar tilt variations:

$$G_{motion} = (|a_x| > 1.5\ m/s^2) \vee (|a_y| > 1.5\ m/s^2) \vee (V_{dynamic} > 0.30\ g) \quad (4)$$

The system categorizes operational slope stability into three discrete warning states:

- SYSTEM SAFE: Evaluated when G_{hydro} = FALSE and G_{motion} = FALSE.
  - Output: Green LED ON, Red LED OFF, Buzzer OFF. OLED displays "STATUS: SYSTEM SAFE".
- CAUTION: Evaluated when G_{hydro} = TRUE while G_{motion} = FALSE.
  - Output: Green LED ON, Red LED ON (dual visual alert), Buzzer OFF (silent warning). OLED displays "STATUS: CAUTION - High Wetness / Rain".
- RED ALERT: Evaluated strictly when G_{hydro} = TRUE and G_{motion} = TRUE simultaneously.
  - Output: Green LED OFF, Red LED ON, 5V Buzzer actively pulsing. OLED displays "STATUS: RED ALERT! - CRITICAL LANDSLIDE".

2.4 Laboratory flume setup and test protocol

Validation trials were conducted using an acrylic flume measuring 1.5 m (L) × 0.5 m (W) × 0.5 m (H) set to an inclination of 35°. The flume was packed with compacted sandy-loam soil. The sensing node was installed such that its 15 cm PVC rod penetrated vertically into the subsurface soil bed.

- Precipitation Simulation: Overhead spray nozzles delivered controlled rainfall to saturate the slope bed.

- Disturbance Rejection: Ambient topsoil tapping and superficial impacts were applied directly on the soil surface to quantify mechanical attenuation.
- Failure Simulation: Hydrological saturation was continued until shear-slip failure occurred along the flume bed, logging transient vibration and tilt deviations in real time.

3.0 RESULTS AND DISCUSSION

3.1 How the system thresholds were determined

The numerical threshold boundaries implemented in the base station firmware were selected based on baseline bench testing and flume calibration trials:

- Hydrometeorological Thresholds (G_{hydro}): The 12-bit ADC of the ESP32 registers values ranging from 0 (maximum wetness/conduction) to 4095 (completely dry air). Baseline testing established that dry compacted soil produced readings above 3200. Progressive water infiltration lowered the analog reading, reaching critical saturation at $ADC_{\text{soilSurf}} < 2600$ for the surface probe (5 cm) and $ADC_{\text{soilDeep}} < 2200$ for the deep probe (12 cm), reflecting soil-water behavioral transitions [7]. Active precipitation on the resistive sensor lowered the reading below $ADC_{\text{rain}} < 2500$, successfully validating the hydrological activation gate.
- Dynamic Motion Threshold ($V_{\text{dynamic}} > 0.30$ g): Flume disturbance evaluations demonstrated that ambient surface noise produced attenuated vector differentials below 0.08 g, whereas structural failure yielded peak transient differentials of 0.58 g. The 0.30 g threshold was established to provide an operational safety margin above ambient noise floor while maintaining sensitivity to shear failure.
- Planar Acceleration Thresholds ($|a_x|, |a_y| > 1.5$ m/s^2): Baseline orientation of the sensor assembly under stationary 35° slope mounting showed transient gravitational drift within ± 0.5 m/s^2. The threshold of 1.5 m/s^2 effectively captures sudden angular dislocation during slope failure without triggering on baseline drift.

3.2 Subsurface mechanical noise decoupling

To evaluate the effectiveness of the 15 cm subterranean PVC rod, identical mechanical disturbances (raindrop impact simulations, surface tapping, and localized footsteps) were applied to direct surface-mounted enclosures and the proposed subsurface assembly.

- Surface Enclosure Response: Registered unfiltered dynamic acceleration spikes exceeding 0.65 g, which would have breached standard alert thresholds and triggered recurring false alarms.
- Subsurface Rod Response: Damped ambient surface disturbances down to 0.08 g (Fig. 5), keeping vibration levels well beneath the 0.30 g trigger threshold.

During simulated slope failure, genuine structural collapse produced a prominent peak response of 0.58 g, confirming that the subterranean rod attenuates superficial noise without damping genuine subsurface shear signals, as illustrated in the comparative acceleration waveform of Figure 3.

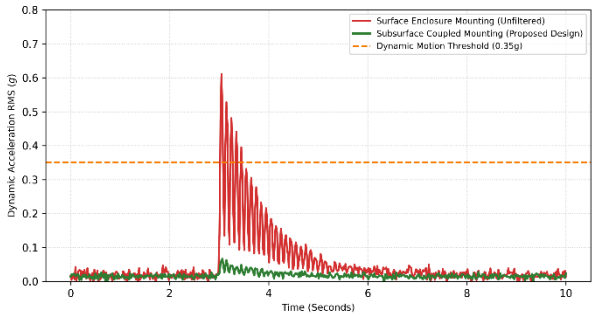


Figure 3: Comparative dynamic acceleration response (V_{dynamic}) over time under superficial ambient impact noise, demonstrating attenuation from 0.65 g (unfiltered surface mounting) down to 0.08 g (subsurface coupled rod mounting) relative to the 0.30 g operational threshold.

The physical assembly of the fabricated transmitter sensing node, internal sensor tray, 15 cm subsurface PVC rod, and the receiver base station are shown in Figure 4.

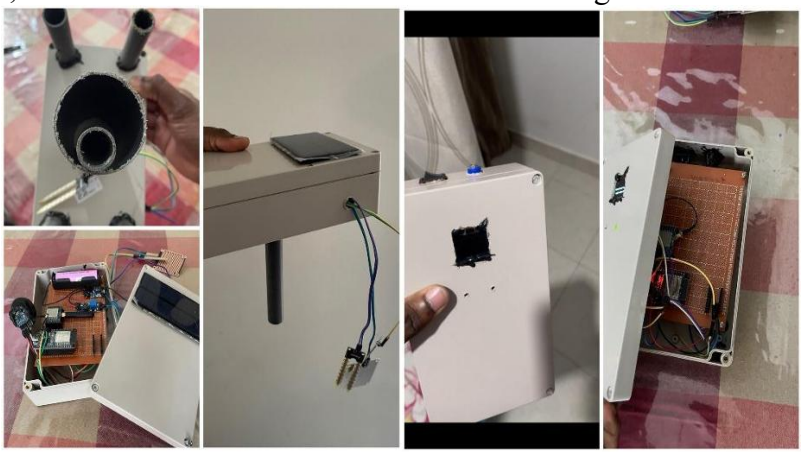


Figure 4: Physical prototype implementations of the monitoring units. (Left) Field transmitter node featuring custom 3D-printed enclosure, internal sensor wiring, and 15 cm subsurface PVC coupling rod; (Right) Receiver base station housing the SSD1306 OLED alert display and status LEDs.

3.3 Warning logic and operational state transitions

The prototype demonstrated consistent and deterministic state transitions across all laboratory testing scenarios, aligning with operational reliability criteria for natural hazard warning schemes [8]:

- Scenario A (Dry Baseline): With sensors dry and the slope stationary, the base station maintained the SYSTEM SAFE state, displaying baseline readings on the OLED while keeping the Green LED active.
- Scenario B (Precipitation & Soil Infiltration Only): When rainfall was initiated without inducing slope movement, G_{hydro} evaluated to TRUE, transitioning the system to CAUTION (Green and Red LEDs active simultaneously, buzzer silent). No false RED ALERT or buzzer alarms were generated during rainfall-only periods.
- Scenario C (Surface Disturbance Under Dry Conditions): Direct topsoil tapping triggered transient acceleration spikes; however, because hydrological conditions remained FALSE (G_{hydro} = FALSE), the system remained safely in SYSTEM SAFE mode.
- Scenario D (Simulated Slope Failure): When prolonged water infiltration compromised slope stability, rapid soil displacement triggered G_{motion} = TRUE while G_{hydro} = TRUE, instantly firing the RED ALERT state, flashing the Red LED, activating the 5V buzzer, and updating the OLED display, As demonstrated by the live hardware status and cloud dashboard telemetry in Figure 5.

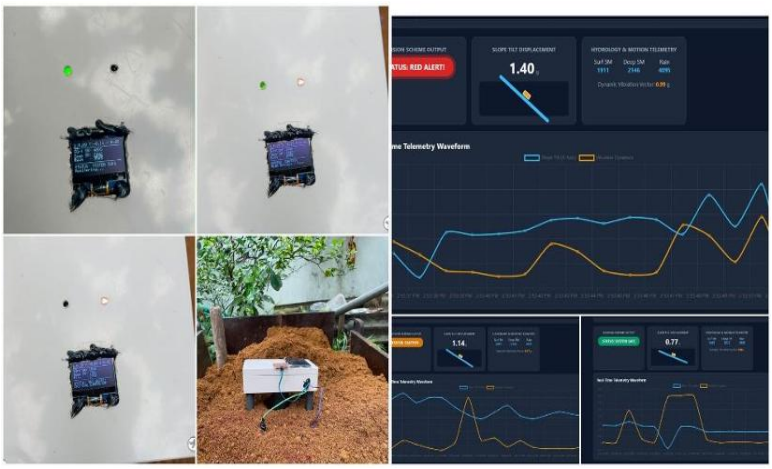


Figure 5: Live multi-tier system alert verification. (Left) Receiver base station OLED visual notifications across SYSTEM SAFE, CAUTION, and RED ALERT operational states; (Right) Real-time web telemetry dashboard visualizing dynamic vibration waveforms, slope pitch angle, and alert banners

3.4 Wireless telemetry and latency considerations

Telemetry data was streamed continuously at a 2 Hz update rate (500 ms packet interval) over the 433 MHz LoRa link. Across indoor laboratory flume separation distances (25 m), the receiver achieved seamless packet decoding and real-time OLED screen updates.
The estimated system response delay from physical sensor displacement to base station alert activation was approximately 420 ms, accounting for MPU6050 sampling (20 ms), differential vector calculation (10 ms), LoRa transmission airtime (250 ms), and OLED rendering/peripheral activation (140 ms). This response speed satisfies real-time early warning requirements for rapid shallow landslides.

3.5 Limitations

Validation of this prototype was conducted under controlled laboratory flume conditions using compacted sandy-loam soil. In natural operational environments, long-term performance may be influenced by heterogeneous soil layers, dense root networks, and harsh outdoor weather conditions. Furthermore, continuous field deployment will require dedicated low-power sleep management and supplementary solar energy harvesting to ensure autonomous long-term operation.

4.0 CONCLUSION

This study presented the design, embedded implementation, and laboratory flume evaluation of a low-cost, dual-node IoT landslide warning prototype utilizing subsurface mechanical noise decoupling and hierarchical data fusion. Mechanically coupling the MPU6050 IMU to a 15 cm subsurface PVC rod successfully attenuated superficial ambient vibration noise from 0.65 g down to 0.08 g, while preserving dynamic shear failure detection peaks up to 0.58 g. The multi-stage decision pipeline (SYSTEM SAFE, CAUTION, and RED ALERT) executed deterministically across tested laboratory regimes, triggering critical RED ALERT emergency alarms exclusively when hydrometeorological saturation coincided with verified kinetic slope movement, thereby eliminating false panic sirens

during isolated precipitation. The 433 MHz SX1278 LoRa telemetry link achieved an estimated end-to-end response latency of approximately 420 ms at a 2 Hz telemetry rate, satisfying real-time warning criteria.

While controlled laboratory flume evaluations confirm the viability of subsurface mechanical filtering and dual-condition fusion logic, operational slope deployment requires further field characterization. Future work will focus on long-term outdoor slope deployment to evaluate system performance under heterogeneous soil strata, dense root networks, and environmental weathering, alongside the integration of dynamic power-management schemes and solar energy harvesting for autonomous field operation.

ACKNOWLEDGEMENTS

The author expresses appreciation to the academic and technical staff of the Department of Electronics, Faculty of Applied Sciences, Wayamba University of Sri Lanka, for their invaluable technical guidance and support.

REFERENCES

1. Intrieri, E., Gigli, G., Mugnai, F., Frodella, W., Casagli, N., *Design and implementation of a landslide early warning system*, Engineering Geology, 2012, 147, 124–136, doi: 10.1016/j.enggeo.2012.07.017.
2. Guzzetti, F., Peruccacci, S., Rossi, M., Stark, C. P., *The rainfall intensity-duration control of shallow landslides and debris flows: an update*, Landslides, 2008, 5(1), 3–17, doi: 10.1007/s10346-007-0112-1.
3. Uchimura, T., Towhata, I., Wang, L., Nishie, S., Yamaguchi, H., Seko, I., Qiao, J., *Precaution and early warning of surface failure of slopes using tilt sensors*, Soils and Foundations, 2015, 55(5), 1086–1099, doi: 10.1016/j.sandf.2015.09.010.
4. Aghenta, L. O., Iqbal, M. T., *Design and implementation of a low-cost, open-source IoT-based SCADA system using ESP32*, AIMS Electronics and Electrical Engineering, 2020, 4(1), 57–86, doi: 10.3934/ElectrEng.2020.1.57.
5. Parri, L., Parrino, S., Peruzzi, G., Pozzebon, A., *Low power wide area networks (LPWAN) at sea: Performance analysis of offshore data transmission by means of LoRaWAN connectivity*, Sensors, 2019, 19(14), 3239, doi: 10.3390/s19143239.
6. Dikshit, A., Satyam, N., *Data fusion techniques for landslide early warning systems: A review*, IEEE Access, 2019, 7, 132450–132463, doi: 10.1109/ACCESS.2019.2940645.
7. ASTM D2216-19, *Standard Test Methods for Laboratory Determination of Water (Moisture) Content of Soil and Rock by Mass*, ASTM International, West Conshohocken, PA, 2019, doi: 10.1520/D2216-19.
8. Sättele, M., Bründl, M., Straub, D., *Reliability and effectiveness of early warning systems for natural hazards: Concept and application to debris flow warning*, Reliability Engineering & System Safety, 2015, 142, 192–202, doi: 10.1016/j.ress.2015.05.003.

Proc. Annual Symposium on Research & Industrial Training, 13 (2026) 111 - 118
Department of Electronics – Wayamba University of Sri Lanka

SOLAR-POWERED IOT SYSTEM FOR OUTDOOR AIR-QUALITY AND ENERGY MONITORING WITH AI-BASED PREDICTION AND AUTOMATIC LIGHTING

K.P.I. Ashani*, S.R.L. Gunawardhana

Department of Electronics, Wayamba University of Sri Lanka, Kuliyapitiya, Sri Lanka

*ashaniimesha2000@gmail.com

ABSTRACT

Rapid urbanization, growing vehicle emissions, and industrial activity have made air pollution a pressing environmental issue, one that demands continuous, location-specific monitoring. However, conventional air-quality stations remain expensive and offer only limited spatial coverage, leaving a clear gap for affordable, autonomous alternatives. This work presents a solar-powered outdoor air-quality monitoring system built around an ESP32 microcontroller and paired with a web-based dashboard using IoT technology. The system combines MQ135 and MQ2 gas sensors to capture air-quality-related gas responses with a DHT22 sensor for temperature and humidity readings, while dedicated voltage and current sensing circuits track solar power generation and battery status. Power is supplied by an 18 V, 5 W solar panel backed by a 12 V, 7 Ah battery, allowing the unit to run independently outdoors. Sensor and power data are pushed over Wi-Fi via HTTP to an InfluxDB cloud database at set intervals and displayed on a Grafana dashboard for real-time visualization. The system also includes an AI-based prediction module that analyses historical readings to forecast short-term trends for selected air-quality parameters, along with an LDR-based automatic lighting feature that switches an outdoor lamp based on ambient light for added energy efficiency. Together, these components form a working prototype validated through outdoor field testing. The gas-hazard alert function was verified across repeated trials using hand-sanitizer vapour and incense smoke as combustible-gas/smoke sources, correctly triggering the buzzer and warning LED in all trials when the MQ2 gas-response ratio fell below the programmed threshold. The automatic lighting function correctly distinguished dark and normally-lit conditions in field tests. Field validation also identified that the solar-side voltage and current readings require further calibration refinement before they can be treated as quantitatively accurate; this and other current limitations are discussed explicitly rather than assumed away. These results demonstrate the practical feasibility of combining air-quality/gas-response monitoring, solar and battery tracking, AI-assisted short-term forecasting, and automated lighting into a single low-cost IoT platform, with promising applications in smart-campus, smart-city, and broader outdoor environmental monitoring settings.

Keywords: **A**ir quality and gas-response monitoring, **S**olar-powered IoT system, **AI**-based prediction

1.0 INTRODUCTION

Air pollution, driven by urbanization, industrial activity, and vehicle emissions, poses serious risks to human health and the environment. Continuous monitoring is essential for tracking pollution trends and identifying high-risk periods [1].

Conventional monitoring stations are accurate but costly, maintenance-heavy, and limited to fixed locations, making dense coverage difficult. IoT technology has addressed this by enabling compact systems that collect, transmit, and visualize sensor data in real time [2], [3], lowering both cost and complexity.

Solar power further enhances the autonomy of outdoor IoT systems, reducing reliance on the grid [4], [5]. Yet few platforms combine air-quality sensing, solar/battery monitoring, real-time visualization, prediction, and automatic lighting into one low-cost system a gap this research addresses.

An AI-based module predicts short-term air-quality trends, while an LDR-based function automates outdoor lighting, together forming a low-cost IoT platform for smart-campus and smart-city environmental monitoring.

2.0 EXPERIMENTAL

2.1 System design and hardware implementation

An ESP32 DevKit V1 serves as the main controller, handling sensor data acquisition, local processing, control, and wireless communication. MQ135 and MQ2 sensors provide responses to air-quality-related gases, smoke, and combustible-gas conditions, while a DHT22 sensor captures ambient temperature and humidity. An LDR detects ambient light to drive the automatic lighting function, and a voltage sensing module paired with an ACS712 current sensor monitors the solar and battery subsystems.

The power system comprises an 18 V, 5 W solar panel, a 10 A automatic 12/24 V solar charge controller, a 12 V, 7 Ah SLA battery, and an XL4015 buck converter: the panel charges the battery through the controller, the battery sustains operation during low solar input, and the buck converter regulates voltage for the electronics. A custom PCB and a SolidWorks-designed enclosure provided reliable wiring and outdoor protection. Table 2.1 summarizes the hardware components and their functions.

Table 2.1 Hardware components used in the proposed system

Component	Function
ESP32 DevKit V1	Data acquisition and wireless communication
MQ135	Gas-response monitoring (relative air-quality indicator)
MQ2	Smoke and combustible gas detection
DHT22	Temperature and humidity measurement
LDR	Ambient light detection for automatic lighting control
Voltage Sensor (0–25 V)	Solar panel and battery voltage monitoring
ACS712	Current measurement
Solar Panel (18 V, 5 W)	Renewable power generation
12 V SLA Battery	Energy storage
PWM Solar Charge Controller	Battery charging and protection
Buck Converter (XL4015)	Voltage regulation
Relay Module	Automatic lighting control switching

2.2 System architecture

The architecture includes an environmental sensing unit, solar-power/battery subsystem, ESP32 controller, wireless interface, InfluxDB database, and Grafana dashboard, as illustrated

in Figure 2.1. The ESP32 collects sensor readings, processes them locally, and handles control tasks.

Sensor and power data are sent via Wi-Fi/HTTP to InfluxDB every 60 seconds, authenticated through an API token. Grafana then pulls this data for real-time visualization and historical analysis. The AI-based prediction module also draws on this historical data to generate short-term forecasts, which appear alongside live readings on the dashboard.

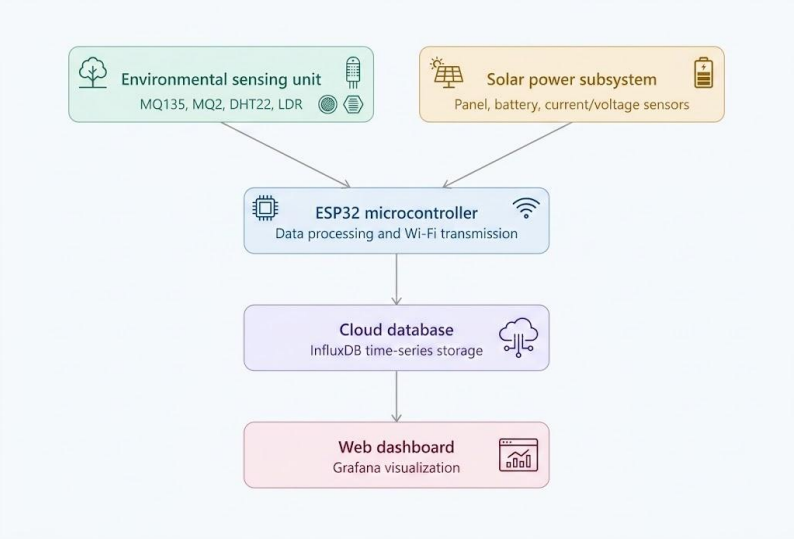


Figure 2.1 System architecture of the proposed outdoor solar-powered air quality measurement system

2.3 Circuit schematic and hardware connections

Figure 2.2 shows the circuit schematic mapping the connections between the ESP32, MQ135, MQ2, DHT22, ACS712, voltage sensor, LDR, relay, and power components. Sensors and outputs were first tested on a prototype breadboard before migrating to the final custom PCB. The solar panel feeds the charge controller, which manages battery charging; the battery then powers the system through the voltage-regulation stage. The ESP32 gathers all measurements and transmits them over Wi-Fi, with the final electronics housed in the SolidWorks enclosure for outdoor protection. The enclosure includes ventilation slots so the gas sensors remain exposed to ambient air, which is necessary for their operation but also represents a potential ingress point for rain and moisture; no dedicated weatherproofing measure (e.g., louvred vents or a drip shield) has yet been implemented, and this is acknowledged as a design limitation for future revisions.

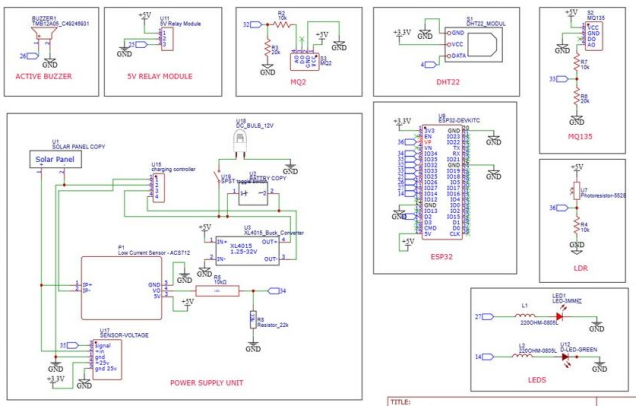


Figure 2.2 Circuit schematic of the proposed system

2.4 IoT communication and web dashboard

The Grafana dashboard offers real-time monitoring of environmental and energy parameters, fed by ESP32 data sent over Wi-Fi/HTTP to InfluxDB every 60 seconds. Displayed parameters include solar voltage, current, and power; battery voltage and state of charge; temperature and humidity; MQ135/MQ2 readings; and lighting/buzzer status, alongside historical trend graphs. AI-predicted values for selected parameters are shown next to actual measurements, letting users track current conditions, past trends, and short-term forecasts from one interface. The automatic lighting function uses a calibrated LDR threshold. When light levels drop below this threshold, the relay switches on the outdoor lamp. A buzzer alerts users when air-quality readings cross a programmed threshold. To handle intermittent Wi-Fi, the firmware retries connection non-blockingly (at most once every 15 seconds) so sensing and relay/buzzer control continue uninterrupted; readings taken while offline are queued locally (roughly 15 minutes at the default upload rate) and flushed to InfluxDB once connectivity returns, rather than being lost. Sensor failures (e.g., an occasional DHT22 timeout) are detected via NaN checks and the affected field is simply omitted rather than a false value being recorded, and solar-power readings are range-checked against the panel's rated output to flag likely calibration faults.

2.5 AI-Based air-quality prediction

Historical MQ135 and MQ2 readings stored in InfluxDB drive short-term forecasting. Raw data, logged at the 60-second upload interval, are resampled onto a 5-minute grid (short Wi-Fi-dropout gaps linearly interpolated), and a separate Random Forest regressor is trained per sensor using three preceding 5-minute lags plus a sine/cosine time-of-day encoding, on roughly two hours of recent history. Forecasts are produced recursively for six 5-minute steps (30 minutes ahead) and re-generated every five minutes, displayed alongside real-time readings on the dashboard. The predicted trend follows the direction of real-time readings but underestimates short-term peaks, consistent with the model not yet being formally evaluated; a quantitative accuracy assessment (e.g., MAE/RMSE on a held-out split) is identified as necessary future work.

2.6 Sensor calibration and data collection

Before system testing, sensors were calibrated for consistency. The MQ135 and MQ2 sensors were calibrated by determining baseline resistance (R_0), yielding 2197 Ω and 3546 Ω respectively. The DHT22 was checked against a reference measurement, giving a temperature correction of 0.00 °C and a humidity correction of 1.9% RH, both applied in processing. The LDR was calibrated by logging ADC values across tested lighting conditions, settling on a threshold of 1637 to distinguish dark from bright conditions. The battery voltage sensor was calibrated against a multimeter reference, giving a fine-tuning factor of 1.0065; the solar voltage sensor produced a preliminary factor of 5.6527. ACS712 current sensor calibration and final voltage-sensor verification were treated as separate steps, so current-measurement accuracy wasn't assumed from preliminary values alone.

2.7 Experimental Procedure

Testing was conducted outdoors with the solar subsystem as the primary power source, monitoring air-quality readings, temperature, humidity, solar/battery voltage, current, and overall system status, with data acquisition verified through the ESP32 serial monitor and

Grafana dashboard. The automatic lighting function was tested by varying ambient light and confirming relay/lamp response against the calibrated threshold; solar-power performance was assessed from panel voltage, charging current, battery voltage, and power (daytime generation/charging, nighttime discharge); and the buzzer was tested against the programmed gas-response threshold. All recorded data were stored in InfluxDB and visualized through Grafana, with historical data later used to generate short-term predictions.

2.8 Ethical considerations

This study involved no human participants, animals, or personal data; it measured only environmental and electrical parameters from its surroundings and its own power subsystem, with all experiments using low-voltage components under standard laboratory safety practices.

2.9 Cost and energy-budget estimation

The total component cost of the prototype (all items listed in Table 2.1, plus custom PCB fabrication and the enclosure) was approximately LKR 14,850 (approximately USD 45, ~328.5 LKR/USD), confirming its positioning as a low-cost alternative to conventional fixed air-quality monitoring stations. A preliminary energy-budget estimate was also carried out to assess autonomous operation: assuming approximately 4.5 peak sun hours/day (typical for Sri Lanka) and around 20% charge-controller/conversion losses, the 5 W panel yields roughly 18 Wh/day of usable energy, while the 12 V/7 Ah battery provides approximately 42 Wh of usable capacity at a 50% depth-of-discharge limit. The continuous electronics load (ESP32 and sensors) is estimated at 0.75-1.0 W (18-24 Wh/day) based on typical component current draws rather than direct measurement, leaving limited surplus for the lighting load; a 1 W LED was therefore selected for automatic lighting, giving roughly 1.5-2 days of battery reserve during extended cloudy periods. This indicates the 5 W panel is only marginally sufficient for continuous operation, and a directly measured total system current draw is identified as necessary to refine this estimate.

3.0 RESULTS AND DISCUSSION

3.1 Gas sensor calibration results

The MQ135 and MQ2 sensors were calibrated prior to testing, giving baseline resistance values of R_0 = 2197 Ω (MQ135) and R_0 = 3546 Ω (MQ2), which were incorporated into the ESP32's processing calculations. Both sensors produced stable, repeatable responses under ambient conditions. As MQ-series sensors respond to multiple gases rather than one specific pollutant, their outputs are treated as general gas-response indicators suited to tracking trends rather than precise concentrations.

3.2 Power Monitoring Sensor Calibration Results

The battery-voltage sensing circuit was calibrated against a multimeter reference, giving a fine-tuning factor of 1.0065. The solar-voltage sensing circuit was calibrated using the same method, producing a factor of 5.6527. The ACS712 (20 A) current sensor was calibrated under both no-load and controlled-load conditions. A zero-current output voltage of approximately 2.1271 V was recorded, and the sensor response was adjusted in software to better align measured and reference current values.

3.3 DHT22 and LDR Calibration Results

The DHT22 required a temperature correction of 0.00 °C and a humidity correction of 1.9%. The LDR was calibrated by comparing ADC readings across lighting conditions, yielding a threshold of 1637 used to trigger the automatic lighting function. Table 3.1 summarizes all sensor calibration results.

Table 3.1 Summary of sensor calibration results

Sensor	Calibration Parameter	Result
MQ135	Baseline resistance R_0	2197 Ω
MQ2	Baseline resistance R_0	3546 Ω
ACS712	Zero-current voltage/error/calibration factor	2.1271 V
Voltage sensor (battery)	Divider ratio/calibration factor	1.0065
DHT22	Temperature/humidity offset	0.00 °C/1.9%
LDR	Day/night ADC threshold	1637

3.4 System operation and discussion

The 18 V, 5 W solar panel, 10 A charge controller, and 12 V, 7 Ah battery were evaluated for system power and low-sunlight operation. Solar voltage varied with sunlight availability, while the battery supplied the system when solar input decreased, with power and consumption derived from the measured voltage and current. Field validation under full sun (panel, charge controller, and battery fully connected) revealed a discrepancy between the solar-voltage sensor (approximately 6.0 V) and a multimeter reading at the panel terminals under the same conditions (20.4 V), with charging-current readings briefly exceeding the panel's rated maximum (approximately 0.28 A for this 5 W, 18 V panel). This indicates the SOLAR_FACTOR and ACS712 calibration constants require re-verification under field charging conditions; a software sanity check now flags power readings exceeding the panel's rated capacity rather than reporting them as valid. This is reported explicitly, as it directly affects how confidently the claimed autonomous solar operation can be quantified at this stage.

3.5 System Operation and Dashboard Performance

The LDR-based automatic lighting function was tested under different ambient-light conditions. When the LDR was covered to simulate dark conditions, the system detected the reduced ambient light level and automatically activated the relay-controlled outdoor bulb (Figure 3.1). The gas-hazard alert function was verified using hand-sanitizer vapour and incense smoke as combustible-gas/smoke sources (approximately 1.5 cm from the MQ2 sensor, 20 s and 30 s exposure respectively, three trials each). The MQ2 gas-response ratio fell from a clean-air baseline of approximately 3.12 to approximately 1.46 under smoke exposure, crossing the 1.5 threshold and correctly triggering the buzzer and red LED in every trial, with the green LED and buzzer-off state confirmed under normal conditions.

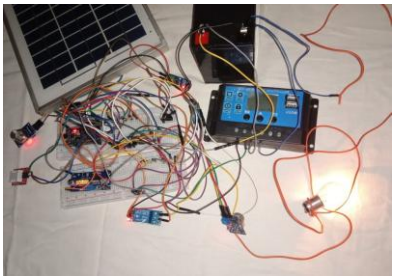


Figure 3.1 Automatic lighting operation under dark conditions with the LDR covered, showing activation of the outdoor bulb.

4.0 CONCLUSION

This research produced a low-cost, ESP32-based solar-powered outdoor air-quality monitoring prototype, combining MQ135, MQ2, and DHT22 sensors, voltage/current sensing, battery storage, and LDR-driven automatic lighting. Calibration gave an MQ135 baseline of $R_0 = 2197$ Ω, MQ2 baseline of $R_0 = 3546$ Ω, DHT22 offsets of 0.00 °C and −1.9%, an LDR threshold of 1637, voltage factors of 1.0065 (battery) and 5.6527 (solar), and an ACS712 zero-current voltage of 2.1271 V. The system reliably transmitted data via Wi-Fi/HTTP to InfluxDB, with Grafana providing real-time and historical visualization. Automatic lighting activated correctly under dark conditions, and the AI-based module generated short-term air-quality forecasts, correctly reflecting the general direction of real-time trends. These results demonstrate the practical feasibility of integrating gas-response, solar, and battery monitoring with IoT visualization, automatic lighting, and AI-assisted prediction into a single low-cost (approximately LKR 14,850) platform. A preliminary energy-budget estimate indicates the 5 W panel is only marginally sufficient for continuous operation, and the solar-side sensors require field recalibration; the prediction model has also not yet been evaluated against held-out data using standard metrics such as MAE or RMSE. Future work will prioritise sensor re-calibration, a formal prediction-accuracy evaluation, directly measured (rather than estimated) system power consumption, and multi-location deployment.

ACKNOWLEDGEMENTS

The authors would like to express their gratitude to the academic staff of the Faculty of Applied Sciences, Wayamba University of Sri Lanka, for their expert advice and guidance.

REFERENCES

1. Duan, X. et al., “Recent progress on phytoremediation of urban air pollution,” *Chemosphere*, 2023, p. 140821, doi: 10.1016/j.chemosphere.2023.140821. (Accessed 2026-07-31).
2. Karnati, H., “IoT-Based Air Quality Monitoring System with Machine Learning for Accurate and Real-time Data Analysis,” 2023. Online. https://arxiv.org/abs/2307.00580 (Accessed 2026-07-31).
3. Lakshmi Narayana, T. et al., “Advances in real time smart monitoring of environmental parameters using IoT and sensors,” *Heliyon*, vol. 10, no. 7, Art. no. e28195, 2024, doi: 10.1016/j.heliyon.2024.e28195. (Accessed 2026-07-31).

4. Nath, D. et al., "Internet of Things integrated with solar energy applications: a state-of-the-art review," *Environment, Development and Sustainability*, 2023, doi: 10.1007/s10668-023-03691-2. (Accessed 2026-07-31).
5. Dai, Y., Chen, M., Yang, Z., "Energy consumption optimization and self-powered environmental monitoring design for low-carbon smart buildings," *arXiv.org*, 2025. Online. https://arxiv.org/abs/2507.15169 (Accessed 2026-07-31).

Proc. Annual Symposium on Research & Industrial Training, 13 (2026) 119 - 126
Department of Electronics – Wayamba University of Sri Lanka

DESIGN AND IMPLEMENTATION OF A MULTI-SPECTRUM LI-FI COMMUNICATION SYSTEM WITH ADAPTIVE TRANSMISSION

H.M.M.U. Menike*, S.R.L. Gunawardhana

Department of Electronics, Wayamba University of Sri Lanka, Kuliyapitiya, Sri Lanka

madaraudeshika2020@gmail.com

ABSTRACT

Radio frequency (RF) wireless communication is increasingly limited by spectrum congestion, and RF communication may be restricted, undesirable, or less effective in certain electromagnetic-sensitive or propagation-challenged environments such as hospitals, aircraft cabins, and underwater installations. Light Fidelity (Li-Fi) offers an alternative that uses modulated light rather than radio waves to carry data, but most existing Li-Fi prototypes rely on a single visible-light source and a single free-space path, which restricts their use to a single lighted, line-of-sight space. This paper presents the design and implementation of a multi-spectrum, dual-path Li-Fi communication system built around an ESP32 microcontroller that transmits data using a 650 nm visible laser LED, a 940 nm infrared (IR) LED, or a 395–400 nm ultraviolet (UV) LED, and that can additionally route the visible laser signal through a fiber-optic cable instead of free space. Four manually selectable switches at the transmitter select between visible-free-space, IR-free-space, UV-free-space, and visible-fiber channels, while a matching set of receivers- a light-dependent resistor (LDR) for the visible channels and a BPW34 photodiode for both the IR and UV channels—recover the corresponding optical signals. Each character of the input message is encoded as an 8-bit ASCII value, encrypted with a lightweight symmetric XOR-based encryption method for confidentiality, after which a cyclic redundancy check (CRC) is appended for error detection; the resulting frame is transmitted using on-off keying (OOK). At the receiver, the CRC is verified, the payload is decrypted with the shared key, and the original message is recovered. During prototype calibration, decision thresholds of 3000, 1850, and 1500 were established for the visible-laser/LDR (both free-space and fiber), IR/BPW34, and UV/BPW34 channels respectively, together with OOK bit durations of 50 ms (visible free-space and fiber), 20 ms (IR) and 30 ms (UV). These give derived raw bit rates of approximately 20 bit/s, 50 bit/s and 33 bit/s. The fiber-coupled visible channel uses the LDR receiver and the same calibration as the free-space visible channel. Experimental results confirmed successful end-to-end encrypted transmission and CRC-verified, correctly decrypted recovery of test messages on all four channels under laboratory conditions. Comparative analysis showed that the IR channel achieved the highest data rate because the BPW34 photodiode responds significantly faster than the LDR, while the visible-laser and UV channels required longer bit periods to maintain reliable detection under ambient laboratory lighting. The system provides a low-cost and flexible platform for comparing different optical channels and transmission methods, with basic data confidentiality.

Keywords: Li-Fi, Multi-Spectrum, **O**ptical Wireless Communication

1.0 INTRODUCTION

Li-Fi is a wireless optical communication technology that transmits data through modulated light instead of radio-frequency (RF) waves. Because optical transmission does not occupy the RF spectrum, Li-Fi is suitable where RF interference is undesirable or restricted, including hospitals, aircraft, underwater systems, and high-security facilities [1]. Conventional systems mainly use visible-light LEDs and photodetectors and generally require illumination and a clear optical path [2], [3]. Infrared (IR) can operate in dark environments, while ultraviolet (UV) offers potential for non-line-of-sight links through atmospheric scattering [4], [5].

Previous work has demonstrated Li-Fi with LEDs, lasers, LDRs, and photodiodes, with performance depending on distance, alignment, detector response, ambient light, and modulation [6]. Single-spectrum prototypes such as those of Sarkar et al. [7] and Ramananda et al. [6] achieve short-range transfer with visible LEDs and OOK but do not allow controlled comparison across bands. IR has been proposed for illumination-constrained settings [4], and fiber-guided paths for point-to-point links between two locations [8]. Most systems examine only one spectrum and one path, so relative performance of visible, IR, and UV on a common platform, and free-space versus fiber in the same system, remains limited.

This study addresses these gaps with a reconfigurable multi-spectrum Li-Fi system based on ESP32 microcontrollers. The system provides selectable visible, IR, and UV free-space channels and a visible fiber-optic path on a shared encoding, lightweight encryption, OOK modulation, and decoding architecture. The visible channel uses a laser LED and LDR; IR uses an IR LED with a BPW34 photodiode, and UV uses a UV LED with a BPW34 photodiode. Holding the platform, frame format, encryption scheme, and OOK constant isolates the effects of spectrum and medium and enables controlled comparison absent from most single-channel prototypes.
In contrast to earlier single-channel designs, the present work places visible (650 nm laser), infrared (940 nm), and ultraviolet (395–400 nm) free-space links together with a visible fiber-optic path on a single ESP32-based platform that uses identical framing, XOR encryption, CRC error detection, and OOK modulation. Quantitative comparison of the four channels under the same laboratory conditions shows that the IR/BPW34 combination supports the highest raw bit rate (50 bit/s) because of the photodiode's faster response, while the LDR-based visible channels are limited to 20 bit/s and the UV channel to 33 bit/s. These measured rates, although modest, are consistent with the known response-time limitations of LDRs and the relatively low optical power of the UV LED, and they provide a clear experimental baseline that was missing from most prior single-spectrum prototype [2,3].

The main objectives are to design and implement selectable visible, IR, and UV free-space channels with a visible fiber-optic path, to develop a common ESP32 transmitter–receiver architecture for encoding, lightweight encryption, transmission, reception, decryption, and decoding, to evaluate channel performance using calibrated decision thresholds, bit duration, and derived raw data rate, to quantitatively compare the four channels are visible free-space, visible fiber-optic, IR free-space, and UV free-space, and to assess the feasibility of multi-spectrum, multi-medium Li-Fi with basic data confidentiality.

2.0 EXPERIMENTAL

2.1 System overview

The system consists of a transmitter unit and a receiver unit, each built around an ESP32 microcontroller, connected by one of four selectable optical channels, as summarized in Table 2.1. Three of these channels are visible (laser LED/LDR), IR (IR LED/BPW34 photodiode), and UV (UV LED/BPW34 photodiode), operate over free space, and are intended for short-range communication within a single indoor location. The fourth channel couples the visible laser LED into a plastic optical fiber (POF) and detects the received optical signal using an LDR at the receiving end; the fiber guides the light by total internal reflection, since the core has a higher refractive index than the surrounding cladding [5]. In this configuration, the transmitter and receiver can instead be placed at two separate indoor locations, with the same hardware forming a simple point-to-point link between them rather than a short-range link confined to one location.

Table 2.1 Transmission channels and their corresponding sources, media, and receiver sensors

Spectrum	Source	Transmission Medium / Range	Receiver Sensor
Visible	650 nm laser LED	Free space, single location	LDR
Infrared (IR)	940 nm IR LED	Free space, single location	BPW34 photodiode
Ultraviolet (UV)	395-400 nm UV LED	Free space, single location	BPW34 photodiode
Visible	650 nm Laser LED	Fiber optic cable, between two locations	LDR

2.2 Transmitter design

The operator enters a text message via serial link to the ESP32. The message is converted to binary, protected by shared-key XOR encryption, and a CRC checksum is appended. Exactly one of the four optical channels is selected by a switch. Data are sent using on-off keying (OOK), with the active LED turned ON for binary 1 and OFF for binary 0. Bit timing is set independently for each channel during calibration. Only one driver stage is active at a time, keeping the branches electrically isolated. Message entry uses a wired serial connection only, so the system remains RF-free. Two status LEDs are provided on the transmitter board. A green LED lights when the complete frame has been successfully modulated and sent through the selected optical channel. A red LED lights if any error is detected during encoding, encryption, or transmission preparation.

2.3 Receiver design

Matching switches select the correct sensor (LDR for visible free-space and fiber; BPW34 for IR and UV). Sensor outputs are conditioned and fed to a common ESP32 ADC. Each sample is compared with a calibrated threshold to recover bits. The CRC is checked; if valid, the payload is decrypted with the shared XOR key and the original message is displayed. If the CRC fails, an error is reported, and the message is discarded. Thresholds were set by measuring ON/OFF ADC levels for each channel and choosing a midpoint value that maximizes immunity to ambient light. The receiver board also includes two status LEDs. The green LED turns on when a frame is received, the CRC check passes, and the message is successfully decrypted and displayed. The red LED turns on if the CRC check fails or if the received data cannot be correctly recovered.

2.4 Hardware implementation

The transmitter is built around an ESP32 microcontroller. Four mechanical switches select one of the optical sources at a time: a 650 nm laser LED (visible free-space or fiber), 940 nm IR LED, or a 395–400 nm UV LED. NPN transistor driver stages are used to switch the IR and UV LEDs while limiting the current drawn from the ESP32 GPIO pins. Message entry is performed exclusively over a wired USB-serial interface; no RF interfaces are used. Figure 2.1 shows the transmitter circuit diagram.

The receiver uses a second ESP32 and a matching set of selection switches. An LDR detects the visible free-space and fiber channels, while a BPW34 photodiode recovers both the IR and the

ultraviolet signals. The conditioned analogue outputs are sampled by the ESP32 ADC, thresholded, and decoded; the recovered message is displayed. Figure 2.2 shows the receiver circuit diagram

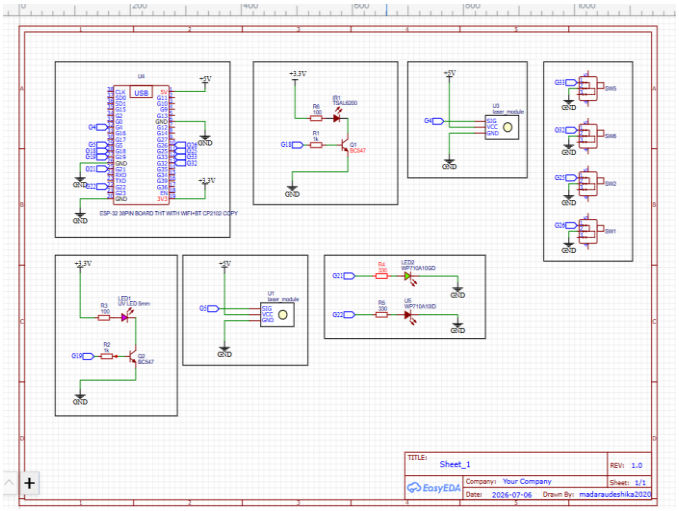


Figure 2.1 Transmitter Circuit Diagram

.

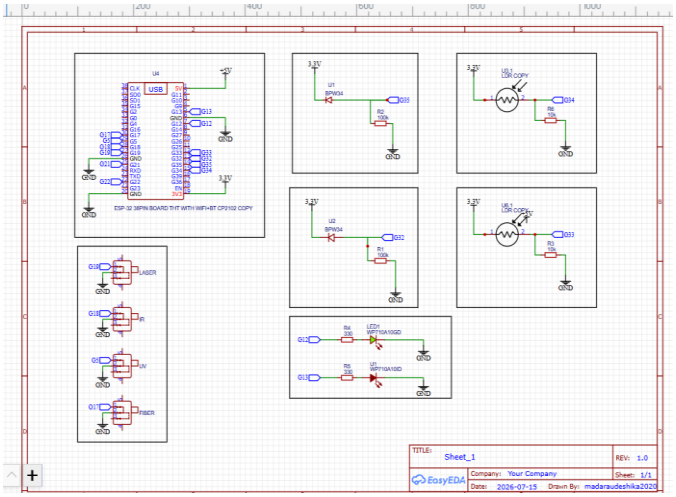


Figure 2.2 Receiver Circuit Diagram

3.0 RESULTS AND DISCUSSION

Figure 3.1 shows the fabricated transmitter PCB developed for the multi-spectrum Li-Fi system. The PCB integrates the ESP32 microcontroller, channel-selection switches, and optical-source driver circuits. The transmitter was designed to support the visible-light laser, infrared (IR), and ultraviolet (UV) optical sources. The ESP32 processed the input data and generated the corresponding digital bit sequence, while the selected driver circuit controlled the optical source according to the transmitted binary data.

Figure 3.2 presents the fabricated receiver PCB used to recover the transmitted optical data. The receiver incorporates the ESP32 microcontroller together with the optical sensing circuits required for the different transmission channels. An LDR was used for visible-light detection, while a BPW34 photodiode was used for both infrared and ultraviolet signal detection. The detected optical signals were converted into electrical signals and processed by the ESP32 through its analog-to-digital conversion and thresholding process.

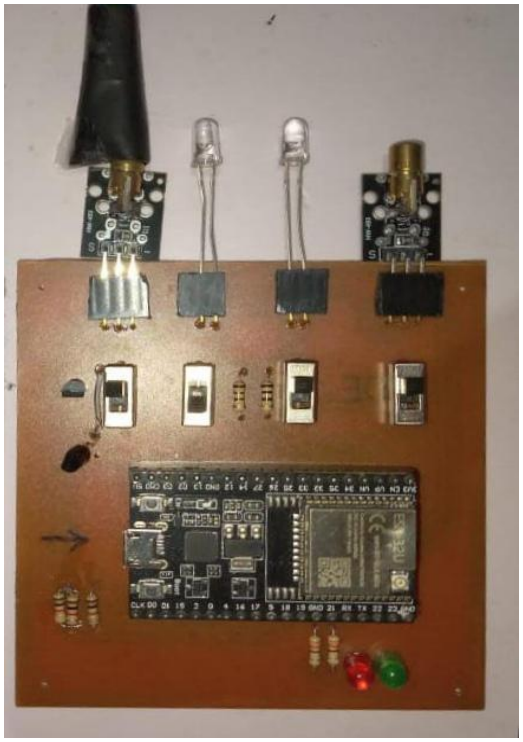


Figure 3.1 Fabricated transmitter PCB



Figure 3.2 Fabricated receiver PCB

Figure 3.3 shows the successful transmission and reception of test data using the developed Li-Fi system. During the experiment, a test message was entered at the transmitter, encrypted with the shared XOR key, protected by a CRC, and converted into a binary data stream. The selected optical source was modulated using on-off keying (OOK), where it switched between ON and OFF states according to the transmitted binary sequence. At the receiver, the optical sensor detected changes in light intensity. The successful recovery of the transmitted message on each selected channel confirms the functional operation of the complete transmitter-to-receiver chain, including encryption and decryption.

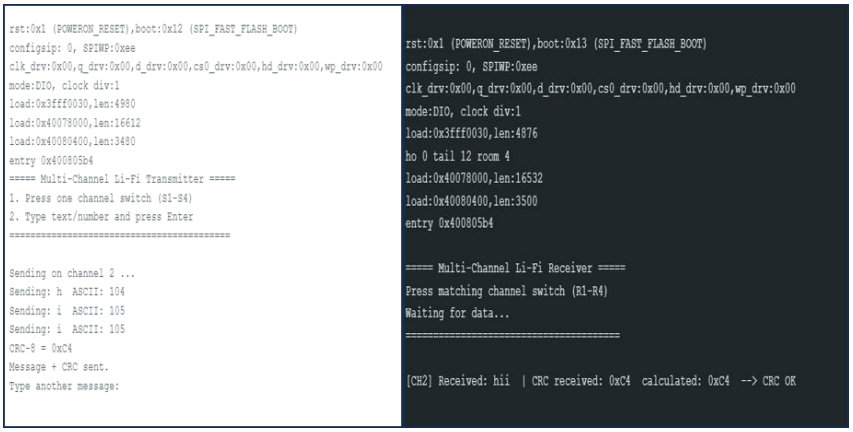


Figure 3.3 Successful Transmission and Reception of Test Data

All four channels successfully delivered CRC-verified and correctly decrypted messages under laboratory conditions. Measured raw bit rates were approximately 20 bit/s for both the visible free-space and fiber channels, 50 bit/s for the IR channel, and 33 bit/s for the UV channel. These differences arise from the photodetectors and available optical power. The IR channel achieved the highest rate because the BPW34 photodiode has a fast response and peak responsivity near 940 nm, allowing a short 20 ms bit duration. The LDR used for visible channels responds more slowly, requiring a 50 ms bit period and limiting the rate to about 20 bit/s. The UV channel needed a 30 ms bit period due to lower LED power and reduced photodiode sensitivity at shorter wavelengths.

The fabricated transmitter and receiver PCBs were successfully implemented and tested, demonstrating the practical operation of the proposed multi-spectrum Li-Fi system. The test results confirmed that encrypted data could be transmitted through the selected optical channel, detected by the corresponding receiver sensor, CRC-verified, decrypted, and correctly reconstructed at the receiver. These results verify the basic functionality of the developed hardware and the end-to-end optical communication link with confidentiality.

4.0 CONCLUSION

The multi-spectrum Li-Fi system successfully transmitted and received digital data over visible, IR, and UV free-space channels and a visible fiber-optic path. CRC-verified, correctly decrypted recovery confirmed the ESP32 transmitter/receiver, optical sources, photodetectors, OOK, lightweight XOR encryption/decryption, and error detection. Calibration gave thresholds of 3000, 1850, and 1500 ADC counts and raw rates of about 20, 50, and 33 bit/s for visible, IR, and UV channels; the fiber path matched the free-space visible rates. These results show that a low-cost, selectable multi-spectrum platform with basic confidentiality is feasible for short-range indoor use in RF-restricted settings.

Future work includes further fiber-length characterization, replacement of the LDR with a faster visible photodiode, automatic channel selection based on received-signal strength, stronger cryptography, higher-order modulation, and extension of the system to support transmission of images and PDF files with a download option at the receiver.

ACKNOWLEDGEMENT

The authors are grateful to the lecturers and staff at the Department of Electronics, Faculty of Applied Sciences, Wayamba University of Sri Lanka for their guidance, support, and access to laboratory facilities.

REFERENCES

1. Aldarkazaly, Z. T., Younus, M. F., Alwan, Z. S.,"Data Transmission Using Li-Fi Technique", *International Journal of Advanced Science and Technology,* 2020, vol. 29, p. 7367–7382
2. Sreesudha, P., Jasmine, S. K. S., Neha, Y., Pranathi, G., "Li-Fi Data Transfer System", *International Journal for Research in Applied Science & Engineering Technology,* 2024, vol. 12
3. Kumar, N. P., Visranthamma, N., Kumar, U. T., Balaji, P. P. S., "Li-Fi Technology for Wireless Data Transfer", *International Journal of Research in Engineering and Technology,* 2025, vol. 12, p. 1244–1250.
4. Gils, J. V., "Infrared Shift: A New Standard for Li-Fi", *CIBSE Journal*, 2025.
5. Guo, L., Guo, Y., Wang, J., Wei, T., "Ultraviolet Communication Technique and Its Application", *Journal of Semiconductors,* 2021, vol. 42